Department of Precision and Microsystems Engineering

Characterization of 2D material/DNA origami interactions for studies of origami conformational dynamics

Demetris Marangis

Report no : 2022.065
Coach : Dr. Sabina Caneva
Professor : Dr. Sabina Caneva
Specialization : Dynamics of Micro and Nano Systems
Type of report : Experimental
Date : 28 October 2022

Delft University of Technology

High Tech Engineering Thesis

Characterization of 2D material/DNA origami interactions for studies of origami conformational dynamics

Author:
Demetris Marangis

Supervisor:
Dr. S. Caneva

in partial fulfilment of the requirements for the degree of

Master of Science

in Mechanical Engineering

to be defended publicly on Friday October 28, 2022 at 01:00 PM.

:

Acknowledgements

First of all, I would like to thank my supervisor and mentor, Dr. Sabina Caneva, for providing me with the knowledge, help and opportunity to work in the exciting field of DNA nanotechnology. I want to thank Dr. Alejandro Martin Gonzalez and Dr. Ze Yu for being great mentors and helping me with the data analysis and use of AFM. Also, thank you to the Steeneken Lab, Cees Dekker Lab and Heuer-Jungemann's Lab for providing the resources required for this project. Finally, I want to thank the Caneva lab for the support and company they have kept me throughout my thesis journey, especially Dr. Dong Hoon Shin and PhD Candidate Xiliang Yang for their help in transferring 2D materials.

Abstract

The discovery of DNA origami nanotechnology has opened new opportunities in this field due to the versatility of the shapes and sizes that can be generated, the ease of modification and functionalization with molecular resolution, and its biocompatibility. Using Watson-Crick base pairing as the main driver in the self-assembly procedure, DNA origami's simple assembly process has paved the way for the design of static and dynamic nanostructures. The main methods of characterization are AFM and TEM. While AFM allows the characterization of static and dynamic nanostructures, TEM is only limited to static. However, the TEM's dynamic imaging ability might be enhanced due to a new technique known as Liquid Cell Electron Microscopy. Graphene, the primary material for the fabrication of Liquid Cells, enables reduced electron scattering, reduced radiation damage and allows enhanced contrast compared to conventional carbon supports. If successful, liquid cell microscopy could enable higher lateral resolution and reduced invasiveness related to AFM measurements while imaging the sample in physiological conditions.

However, graphene has been a hostile substrate for DNA origami nanostructures. Due to $\pi-\pi$ bonding of graphene, DNA bases react with the delocalized π electrons of graphene and are denatured, causing unwanted deformations in the nanostructures. Additionally, other 2D materials with $\pi-\pi$ bonds like MoS_2, which was also involved in liquid cell microscopy, have shown similar deformations with DNA origami structures. Various functionalizations have enhanced the biocompatibility of graphene and MoS_2 surfaces, reducing the degree of deformation of DNA origami nanostructures. A drawback of all these studies is the lack of similarity between the substrates and the methodologies used for the transfer of 2D materials. This impedes the comparison of the interaction of DNA origami with pristine and functionalized 2D materials.

This project aims to qualitatively assess the interaction of DNA origami with pristine and functionalized 2D materials. First, measurements on mica were taken as a baseline for comparison. It was found that the location where the measurement was taken affects the surface's cleanliness due to the morphology of the cleaved mica. A reduced amount of salt was found present in the centre of the mica compared to the side, which allowed an accurate characterization of DNA origami nanostructures. In addition, rinsing 2-3 times reduced the roughness, increased the adhesion of DNA origami nanostructures and diminished the concentration of salt on the mica substrate. Next, the deposition of DNA origami on graphite substrates has shown a shrinking of DNA origami triangles ($\approx$ 10 nm) due to the melting of dsDNA to ssDNA. A similar deformation was observed in hBN substrates that have a similar shape to graphene but have localized π electrons. Functionalization with poly-l-lysine decreases the degree of deformation of DNA origami nanoarchitectures. However, the values still do not match the ones experienced on mica. Conclusionally, pristine graphite and hBN supports cannot serve as an alternative substrate for imaging DNA origami nanostructures. The optimization of the functionalization protocol might enable the use of graphite as TEM grids.

Contents

1 Introduction **1**

2 Theoretical Background **3**
2.1 DNA origami nanotechnology . . . 3
2.1.1 DNA and DNA origami . . . 3
2.1.2 Dynamics of DNA origami . . . 6
2.1.3 Techniques for imaging conformational dynamics . . . 9
2.2 2D Materials . . . 11
2.2.1 Graphene Liquid Flow Cells . . . 11
2.2.2 Interactions of DNA origami and Graphene . . . 14
2.2.3 Ultrathin Materials used for preparation of the liquid cells . . . 18

3 Research Proposal **20**

4 Experimental Methods **21**
4.1 AFM Imaging . . . 21
4.1.1 AFMs used for this project and their properties . . . 22
4.1.2 Deposition of DNA origami on mica and AFM imaging . . . 24
4.1.3 Deposition of DNA origami on 2D materials and AFM imaging . . . 25
4.2 Transfer of 2D materials on mica . . . 25

5 Results **29**
5.1 Characterization of DNA origami on Mica substrate . . . 29
5.1.1 Effect of Scanning Region Location on adhesion of DNA origami on mica . . . 31
5.1.2 Rinsing Test . . . 33
5.1.3 Measurement of Triangle Sides on Cleaved Mica . . . 37
5.2 Deposition of buffer on pristine graphite . . . 39
5.3 Deposition of DNA origami on mica after transfer from empty PDMS stamp . . . 40
5.4 Characterization of DNA Origami on Graphite . . . 42
5.4.1 Different Incubation Times . . . 46
5.4.2 Characterization of DNA origami triangles on graphite . . . 48
5.5 Functionalization of graphite with poly-L-lysine . . . 51
5.5.1 Effect of incubation time on the roughness and topology of poly-L-lysine functionalized graphite substrates . . . 57
5.6 Characterization of DNA origami on pristine hBN substrates . . . 60

6 Conclusion and Future Work **65**
6.1 Conclusion . . . 65
6.2 Future Work . . . 66

A Appendix **73**

A.1 Preparation of Buffer 73
A.2 Preparation of mica 73
A.3 Complete Data of Rinsing Conditions Experiment 74
A.4 Composition of Rutherford Triangles (RTO) DNA origami 74
A.5 Imaging of DNA origami diluted with MilliQ water on mica and graphite substrates . 75

Chapter 1

Introduction

In 1982, Nadrian Seeman revolutionized the field of DNA nanotechnology by inventing a new type of DNA structure called DNA origami [1]. While DNA is known as the basis of the genetic information in all living organisms, Seeman created a nanostructure that can self-assemble via various hybridization reactions. These structures consist of a long scaffold strand and several staple strands that fit in defined positions on the scaffold depending on their sequence. By using hybridization reactions between complementary DNA strands, folding of the DNA origami structure can be achieved at the desired positions, giving rise to a variety of structures, from simple plates to complex machine-like components. The primary imaging technique for static and dynamic DNA origami nanostructures is Atomic Force Microscopy (AFM). Despite its success, AFM measurements are affected by the invasiveness of the method due to tip interaction, the lateral resolution limit and the inability of molecular spectroscopy methods.

Transmission Electron Microscopy, or TEM, is an alternative imaging method that has also shown significant success in imaging biological structures, including DNA origami, with high resolution. It has a higher lateral resolution than AFM measurements and allows spectroscopy measurements. In spite of these advantages, high-power electron beams used in TEM have caused damage to DNA origami nanostructures. The damage is minimized through the use of cryo-state TEM which successfully reduces the damage to biological samples. On the other hand, samples are no longer in their physiological conditions, thus affecting the characterization accuracy. Another limitation of cryo-state TEM is its inability to measure intermediate states of dynamic DNA origami. A new method of TEM, called Liquid cell Microscopy has evolved in the past years and might enhance TEM's dynamic imaging ability. A liquid cell can be defined as a bilayer of a conductive material that is separated by a 'pocket' where the biological sample can be inserted. The main material for its fabrication until now is graphene. Graphene's properties allow minimal radiation damage to the nanostructures and increase the transparency of the sample. Therefore, graphene's liquid cells are an attractive solution to the challenges of TEM imaging that will enable high-resolution measurements of static and dynamic DNA origami nanostructures under physiological and vacuum conditions.

On the other hand, studies involving the deposition of DNA origami on bulk/few-layer graphene substrates have shown significant deformations because of the $\pi - \pi$ interactions of graphene with DNA bases [2]. DNA origami is losing its folding structure and in a few cases, dsDNA strands melt into ssDNA strands. The main reason is the influence of graphene on the $\pi - \pi$ bonds of the adjacent bases on DNA strands. In addition, researchers have also noticed denaturation of DNA strands in another 2D material used for the fabrication of liquid cells, MoS_2, because of the presence of $\pi - \pi$ bonds. The role of functionalization has played a key role in providing a more 'friendly' environment for DNA origami on the aforementioned 2D materials. Functionalizing graphene with poly-l-lysine and pyrene among others has provided the substrate with a biocompatible environment for DNA origami and has reduced its denaturation.

A literature gap is found in the quantitative assessment of pristine and functionalized 2D materials using similar substrates, nanostructures and transfer methods. The main goal of this project is to fill this literature gap, by using the well-known Rutherford Triangles (RTO) to examine the interaction of DNA origami with 2D materials, mainly graphene, both in their pristine and functionalized state. Furthermore, the effects of roughness and cleanliness of the surface would be assessed to find the optimal environment for the stable deposition of DNA origami. The interaction of DNA origami with different 2D materials will be investigated using AFM measurements and compared to the current ideal substrate for AFM imaging, mica. The first chapter describes a detailed overview of the DNA origami design process; the static and dynamic nanostructures already manufactured by researchers. In addition, results from the deposition of DNA origami and its interaction with various 2D materials are described. Subsequently, the research questions answered in this report are outlined. The next 2 chapters convey the experimental protocols and the results of the experiments conducted, followed by data analysis and discussion. Finally, conclusions drawn from the experiments and future work are reported.

Chapter 2

Theoretical Background

2.1 DNA origami nanotechnology

2.1.1 DNA and DNA origami

DNA serves as the primary storage system of genetic information in living organisms. It is composed of molecular sub-units referred to as nucleotides, whose combinations form the genetic sequence of a cell. DNA strands consist of a sequence of 4 different bases: adenine (A), guanine (G), cytosine (C), and thymine (T). The bases are arranged by forming complementary base pairs, also referred to as Watson-Crick base pairing, giving rise to the famous double helix (dsDNA) structure [1] (Figure 2.1). 2 types of base pairs form, A-T and C-G. This simple yet powerful rule is the main reason why generating complex DNA-based nanostructures can be achieved in a highly predictable manner and with ample room for versatility regarding shape and size.

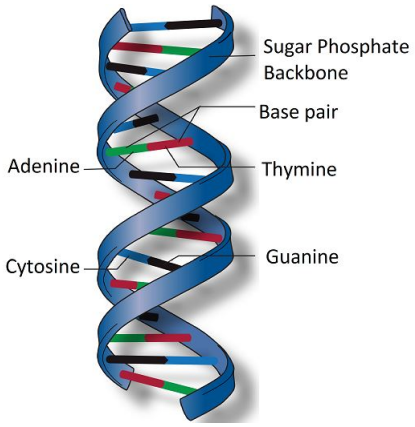

Figure 2.1: The DNA double helix: schematic showing the structure of double-stranded DNA [3]. The phosphate backbone gives DNA its highly negative charge

.

As can be seen in Figure 2.1, except for the bases that carry the genetic sequence, DNA consists of a sugar phosphate backbone. The phosphate backbone gives a highly negative charge to the DNA strand and plays a significant role in imaging.

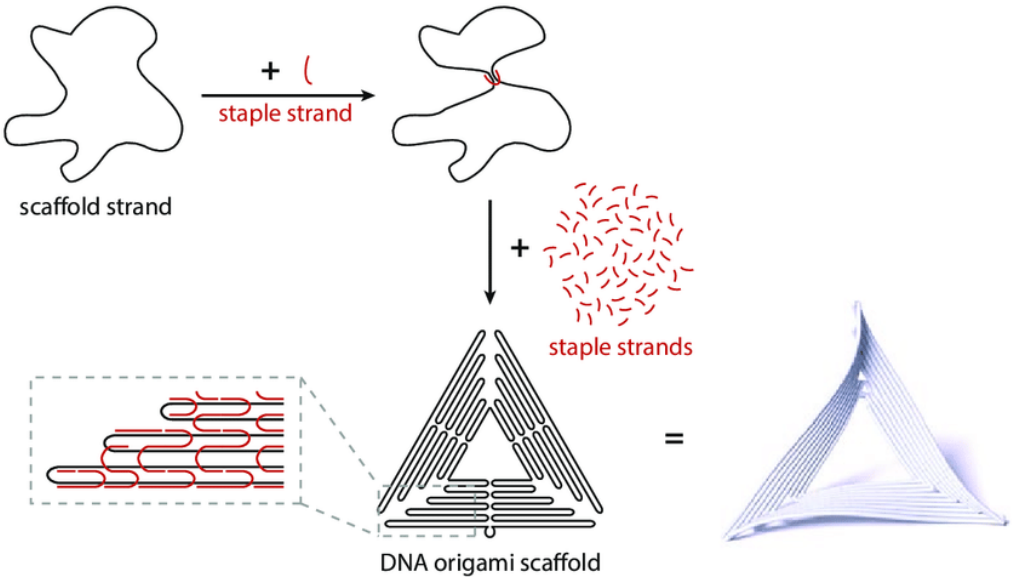

Figure 2.2: Schematic diagram of the assembly process. The staple strands consist of different sequences that bind to specific locations on the scaffold strand, forming complementary base pairs. The staple strands serve as guides for the structure to form the desired shape. Adapted from [4].

DNA origami, the main material utilized in this project, can be rationally engineered to assemble into virtually any desired shape. Structures start from a long scaffold strand that serves as the base of the structure and is acquired by extracting the base sequence of a virus, typically the M13mph18 bacteriophage [5]. At specific locations along its length, various short staple strands that are complementary to the scaffold strand are attached. These staple strands produce folding of the scaffold strand that guides the nanostructure to the desired final shape. This assembly process is schematically shown in Figure 2.2. During the self-assembly of the DNA origami, staple strands are added in excess (usually tenfold) to allow a much quicker hybridization and to reduce the possibility of adding an incorrectly bound staple [6]. Some examples of possible DNA origami structures assembled using this technique are shown in Figure 2.3.

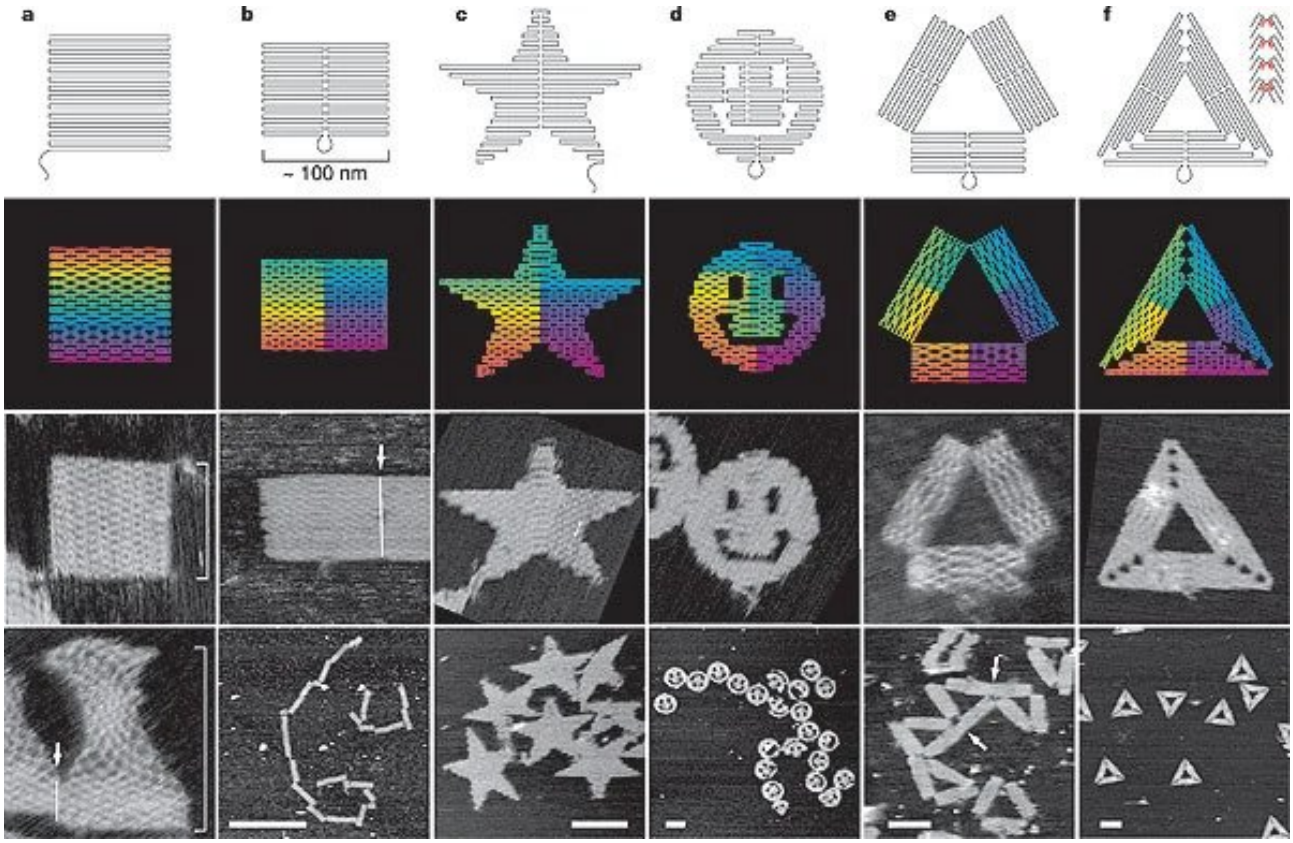

Figure 2.3: Examples of different DNA origami structures, depicting the wide variety of geometries that can be designed (top two rows) and produced (bottom rows AFM images). Adapted from [7].

Design rules should be followed for a stable assembly of the DNA origami molecule, outlined in detail in [1]. The shape of the DNA origami nanostructure is determined using the Watson-Crick base pairing. DNA origami design is made easier through the use of the specialized CAD software, called CADNano, which helps users allocate the location and the suitability of the staple strands that will enable a stable assembly. The output of this software gives the base sequences of both the staple and scaffold strands that can be synthesized either in-house or bought commercially from companies such as Tilibits Nanosystems. The interface of the software is seen in Figure 2.4. CADNano allows for the assembly of both a square and honeycomb lattice, which are the two types of lattices commonly used in literature. Once the scaffold strands and the staple strands are generated, the assembly occurs in a so-called synthesis buffer, followed by a thermal annealing process. Using a suitable buffer solution and excess staple strands helps in maximizing the desired product yield. The annealing and assembly process can occur over different timescales depending on the design of the DNA origami and typically range from 1 day up to 1 week [6].

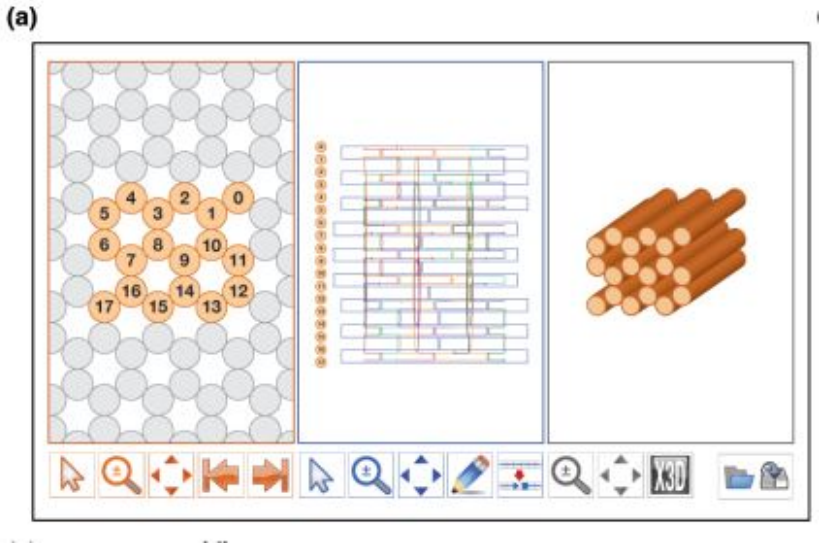

Figure 2.4: Interface of CADNano. Left: Cross-section of the lattice formed (in this case honeycomb). Middle: Structure and position of the scaffold and staple strands before folding. Right: 3D representation of the scaffold strands the users have selected. Adapted from [8].

2.1.2 Dynamics of DNA origami

The predictability of the DNA origami configuration has allowed researchers to create static and dynamic nanostructures. In the literature to date, the dynamics of DNA origami are based on a mechanism called 'strand displacement reaction'. Strand displacement occurs when two strands with partial or full compatibility hybridize with one another. Through a succession of reversible single nucleotide dissociation and hybridization stages, one domain displaces another of similar sequence (branch migration)[9]. These displacement reactions are often triggered by complementary single-stranded DNA molecules (ssDNA), known as toeholds. The size and base composition of the toehold will control the rate of the strand-displacement reactions. Figure 2.5 shows an example of this mechanism: Region 3 acts as a toehold that causes branch migration of region 2 and gives rise to the final products B and Y, where Y is the closed state of complex X.

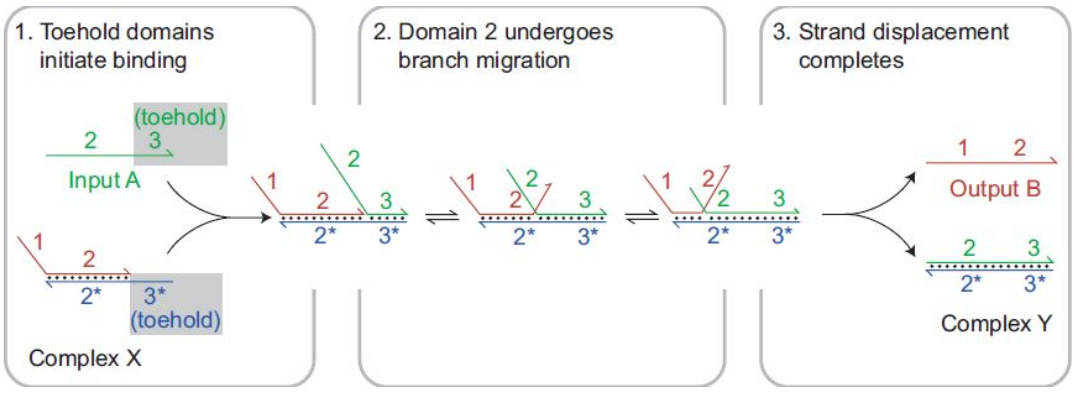

Figure 2.5: Schematic diagram of a strand displacement reaction. Toehold region 3 initiates the reaction, resulting in branch migration of region 2 that produces the two products B and Y. Adapted from [9].

Furthermore, strand displacement reactions are enzyme-free and can be stopped by hybridizing the single-stranded toeholds into double-stranded (ds) structures. They can also be geometrically con-

strained by forming a hairpin, which as its name suggests, is a DNA structure in the shape of a loop. For a reversible mechanism to exist, the base sequences of the DNA origami strand, the actuator strand (used for forward assembly), and the closing strand (used for reverse assembly) need to be carefully considered and designed. The reversible mechanism can be based on strand displacement reactions. An example of its implementation is described in detail in the article by Marini et al. [10]. To enable reversible assembly, the authors use a partly complementary single-stranded (ss) DNA for forward assembly, whereas to bring the configuration back to its initial condition, a single-stranded DNA referred to as 'competitor' is added, which is perfectly complementary to the actuator strand. The 'competitor' allows the detachment of the actuator strand from the DNA origami nanoactuator.

Compliant Mechanisms

Compliant mechanisms have increased flexibility relative to traditional mechanisms, by gaining mobility from the deformation of their robust members. Their high precision and predictability will be essential in applications such as nanopore gating, where control of the nanopore's state is essential for accurate measurements. Nanopores are nano-sized channels in biological membranes that allow the selective transport of molecules and ions inside a cell. The change of state during gating occurs from a small-sized pore (closed) to a larger-sized pore (open). DNA origami nanotechnology has already proven its ability to mimic more complex dynamical structures inspired by mechanical engineering, as schematically shown in Figure 2.6.

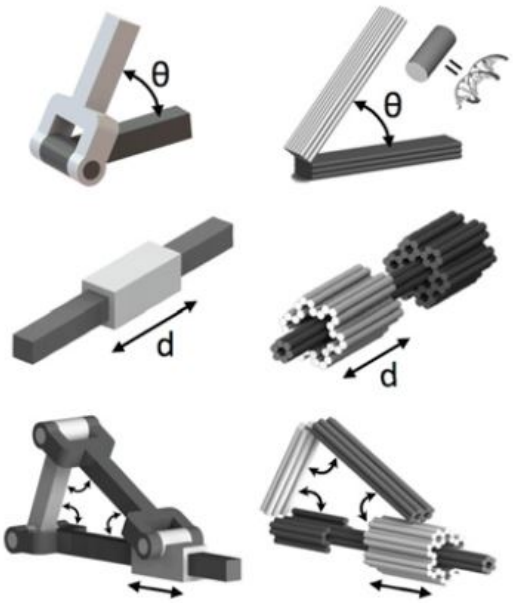

Figure 2.6: Schematic showing various types of machine components that can be designed using DNA origami nanotechnology, including joints for angular or linear motion and crank-sliders, which couple rotational to linear motion. Adapted from [11].

Joints and sliders are formed by replacing beams in the original mechanical structures with DNA origami tubes, as described in [11]. Flexible single-stranded DNA connections along a line, create a hinge axis, which gives rise to joints. The slider joint is formed by joining two stiff strands with complementary structures using robust ssDNA scaffold connections. An important observation is that fewer and longer ssDNA connections can be used to enhance the range of motion. The magnitude of the stiffness ranged from 0.42 pN/mm for small sliders with short connections, to 0.07 pN/mm for sliders with larger connections and small displacements. It should be noted that sliders with larger

connections had a nonlinear stiffness response, whereas for shorter connections stiffness was linear. Values of the torsional stiffness for the hinges were in the range of 25-70 pN-nm/rad. These values give an idea of the magnitude of the stiffness expected from the dynamic DNA origami designs.

An interesting mechanism was developed by Ke et al. [12] and involved a rhombus-shaped structure that behaved in a mirror-like behaviour. DNA origami changes its shape from an open (i.e. enclosing a large area) to a closed state (i.e. enclosing a small area) using a lock and key mechanism. The design of the actuator and the states the nanoactuator occupies are shown in Figures 2.7 and 2.8.

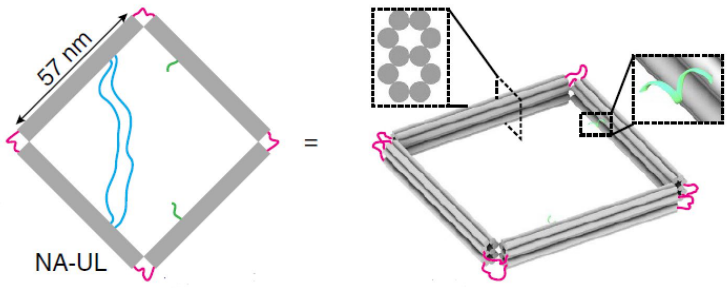

Figure 2.7: Design of the rhombus-shaped actuator. The blue and pink strands are single-stranded DNA, that act as links and hinges to minimize out-of-plane movement and enable the nanoactuator to adopt different planar configurations. The green strands are used for cargo molecule attachment. Adapted from [12].

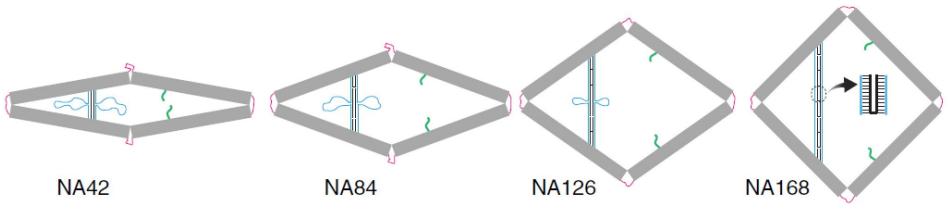

Figure 2.8: Locking strands of different nucleotide lengths are applied to the structure to control the configuration of the nanoactuator [12]

The rigid arms are designed to prevent deformation from bending, shearing, or torsional stress. The structure importantly includes two long single strands inside the rhombus that control the conformation of the DNA structure (blue lines). Connecting strands of different lengths were added, and their effect on the configuration the nanoactuator occupies is examined. As the length of the connecting strands increased, the side angles also increased in the steady state of the nanoactuator. Buffers, enzymes, and nucleic acids were utilized as triggers to change the state of the nanoactuator from closed to open. The process was monitored through the use of a fluorescence dye and involved the dissociation of the corner locks initially added (top and bottom pink strands). A drawback of this design is that it does not allow reversibility, therefore once it reaches its locked state, it cannot be unlocked.

Actuation Mechanisms

Besides the actuation using strand displacement, there are several alternative mechanisms for switching conformational states of DNA origami nanostructures. Here I briefly review the different types:

- **Photoactive molecules**: The operating principle is photosensitivity, which in the work by Tanaka et al. [13], enabled the actuation of a reversibly gating DNA capsule. Gating is carried

out by using a photosensitive azobenzene molecule, which breaks into small structures upon exposure to UV light. At an illumination wavelength of approximately 300-400 nm, azobenzenes change their structure from trans to cis. Cis and trans isomers refer to molecules that have different geometric configurations such that the cis configuration prevents the formation of double-stranded structures since it occupies a hairpin shape [14]. In the trans-state, the hairpin loop opens and the nanostructure adopts the open state.

- **pH change**: There are 2 methods to trigger actuation using pH
  1. in low pH, a quadruplex (quadruple strand DNA) conformation also known as i-motif is formed from an ssDNA with a high number of cytosines (C) bases [15].
  2. DNA triplex (triple strand DNA) can be formed only in acidic pH, therefore raising the pH to become alkaline can destabilize the structure [16]
- **Ionic concentration**: High salt compositions and low temperatures can result in a transfer of a double-stranded DNA from a right-handed configuration (B-DNA) to a left-handed configuration [17].
- **Electric fields**: Due to the negative charge of the phosphate backbone, electrical actuators have been used on a flexible DNA-origami arm where the direction of the electric field determines the location where the complementary base pairing occurs [18]. This relatively fast mechanism can take place in less than one second.
- **Magnetic fields**: By attaching a micron-sized magnetic nanoparticle, rotational motion was achieved in a DNA origami rotor when external magnetic fields were applied to the system [19].

2.1.3 Techniques for imaging conformational dynamics

The characterization and imaging of DNA origami have been performed using Atomic Force Microscope (AFM) methods. Here, parameters such as buffer composition and substrate functionalization affect the quality of the DNA origami structural stability. AFM measurements require an extremely flat surface to obtain high-resolution images. Mica was found to be the substrate of choice in the vast majority of previous work. Cleaving mica produces an ultra-flat and negatively charged surface that DNA origami, with the appropriate chemical functionalities, can bind to[20]. Measurements can be performed in both liquid and dry conditions. Performing measurements in liquid mode enable increased mobility of the DNA structures compared to measurements in air, therefore they are better suited to the study of dynamics of the conformational changes. Measurements in air, on the other hand, might be better for static DNA origami because of their decreased mobility which would allow the characterisation of the structural properties of DNA origami nanodevices. On the downside for air measurements, the lack of a buffer or water might affect the dimensions of the structure because the DNA nanodevices are not in physiological conditions, resulting in a loss in structural stability. High-speed AFM modes can also be used as a reliable tool to accurately image nanostructures at 1-second time frames, as demonstrated by Endo et al.[21] (Figure 2.9). In their study, they manage to capture successfully the intermediate states of a cube, unfolding to its planar 2D form.

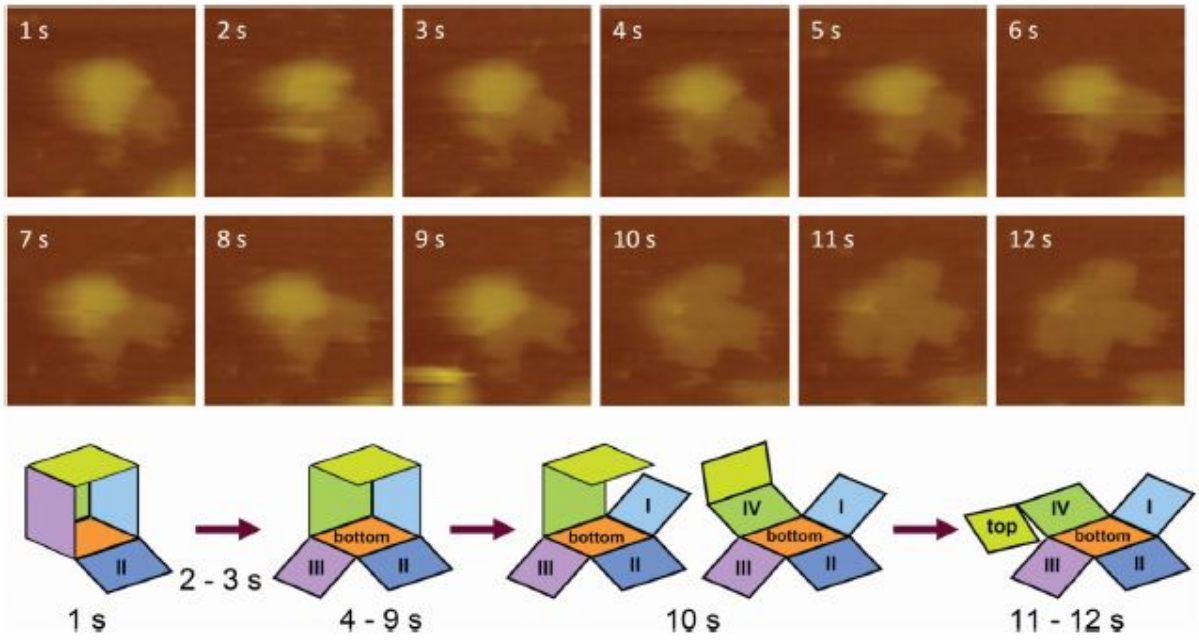

Figure 2.9: Time series during the conformational change of a DNA origami structure during the transition from a 3D cuboid surface to a flat surface. High-speed AFM images (top) and a schematic of the folding process (bottom) are shown. The data is adapted from [21].

Optimizing the buffer conditions is an important step for the imaging protocol. Two main strategies have been adopted for high-resolution imaging by the field and involve:

- Using a buffer solution with divalent cations that will enable attraction of the DNA origami to the mica surface;
- Chemically modifying the mica surface.

Both methods were successfully implemented in the imaging of DNA origami nanostructures because they enable the attraction of DNA origami to the mica. Furthermore, Xin et al. [22] state that a magnesium-free environment is crucial for the dynamic imaging of DNA origami nanoactuators. The main reason behind this is that in high magnesium concentrations the switching and actuation mechanisms of the DNA origami are affected by the influence of magnesium in the reactions and processes of DNA origami [22]. Therefore, as the first step in their protocol, they perform a buffer exchange from the TAE/Mg^{2+} (synthesis buffer) to an Mg-free phosphate-buffered saline (PBS) buffer by spin filtering. Spermidine modification of the mica enabled the stronger adsorption of DNA origami structures in PBS, superior even to magnesium. Additionally, poly-L-lysine also enabled a strong absorption of DNA origami structures in both pure water and PBS buffer. Figure 2.10 conveys the distribution of DNA origami structures on mica functionalized with spermidine. A compromise of the immobilization strength and the mobility of the DNA origami in the sample is required to ensure optimal imaging conditions for both dynamic and static structures.

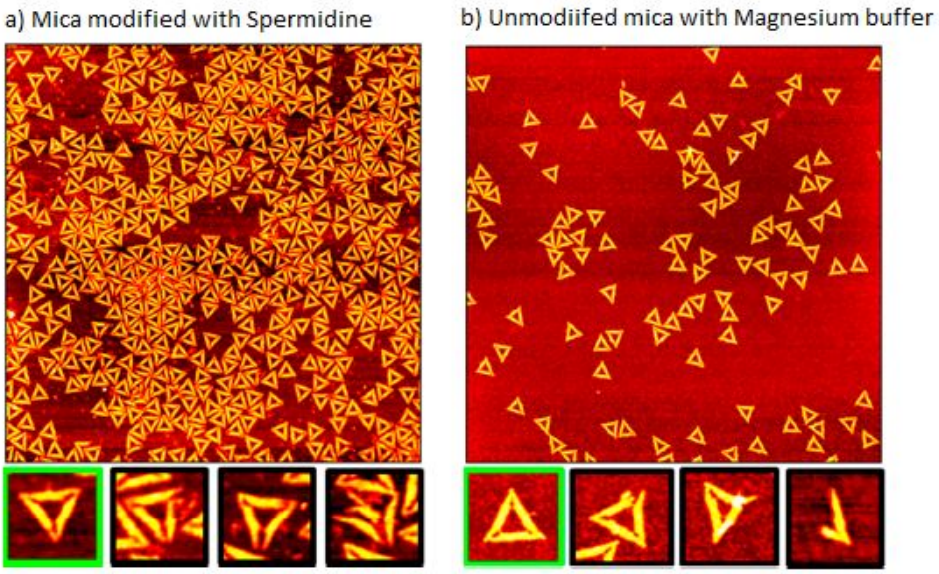

Figure 2.10: Deposition of DNA origami triangles on a) spermidine modification of the mica, where the DNA origami structures were placed in PBS buffer and b) magnesium buffer. Adapted from [22].

For static analysis of DNA origami structures, there is no need for a magnesium-free environment and this simplifies the process, since a TAE/Mg^{2+} buffer would enable enough adhesion force to bind the negative DNA origami structures with the freshly cleaved mica.

2.2 2D Materials

2.2.1 Graphene Liquid Flow Cells

AFM has proven a valuable tool for imaging biological samples in static and dynamic modes. However, AFM has its drawbacks. Due to its lateral resolution limitation, AFM measurements cannot provide accurate representations of the interior or hidden parts of the structure. The lateral resolution of AFM measurements is defined by the radius of the cantilever tip since it limits the detection of structures with shorter dimensions. Another disadvantage is the significant amount of noise caused by the tip interactions with the surface and the ease by which cantilever tips become attached to biomolecules. Another disadvantage of the AFM is the damage caused by the tip when it interacts with biological samples, even though the set point parameters are optimized to minimize interaction. Furthermore, AFM does not allow any chemical characterization to verify the identity of the biological sample imaged, sometimes creating questions about the nature of the imaged structures. Some of the problems posed by AFM can be solved by another form of microscopy, namely Transmission Electron Microscope (TEM). Currently, the imaging of biological samples like DNA origami and proteins under TEM is possible, however, several challenges limit its usage. Among them, the differential scattering of electrons as they pass through areas of the supporting substrate limits the imaging resolution[23] by creating background noise. Also, because of the poor contrast of biological samples, staining methods with heavy metals are required. The staining is often negative, causing artificial aggregations as the heavy metal binds with the phosphate and carboxyl groups, predominantly found in biological materials [24, 25]. A new method of TEM imaging has been a point of interest, showing great potential in improving the imaging capability of biological samples under TEM. It is called liquid flow cells, and the primary material used for their application was graphene. Graphene liquid flow cells (GLC) can be described as two monolayer graphene surfaces separated by a pocket (distance between the

sheets) of liquid placed (1st generation GLC in Figure 2.11). The current state-of-the-art and further generations of liquid cells are depicted in Figure 2.11. The difference between the 2 layers of graphene for 1st generation GLCs was about 100 nm.

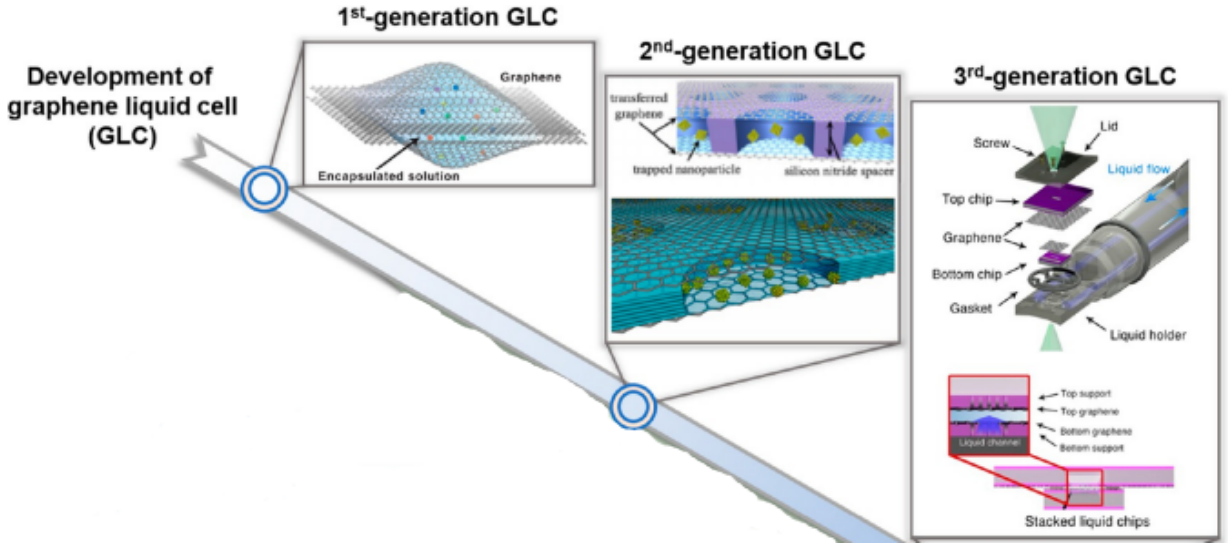

Figure 2.11: Schematic diagram of different types of graphene liquid cells. The design that is mainly used to date is the 1st generation GLC, seen in the upper left corner. Adapted from [26].

Since 2004, when graphene was exfoliated from graphite, graphene has emerged as an attractive material due to its outstanding range of physical properties. Graphene's structure offers a thin surface with enhanced resolution, and contrast (due to the transparency of graphene) under TEM imaging compared to conventional carbon supports [27]. Another advantage is the ability of the thin structure of few-layer graphene to minimize background electron scattering [28] because of the limited influence of the graphene layer on the electrons passing through the substrate. Furthermore, the few-layer graphene structures have a high thermal and electrical conductivity that are essential in the reduction of electron-beam damage on the imaging sample [29, 30]. Furthermore, researchers have found a substantial decrease in leakage and contamination experienced in graphene-encapsulated samples during sample preparation [31]. Given the aforementioned properties, graphene could be an excellent material for TEM substrates, solving the challenges of sample preparation, contrast and damage encountered in TEM studies of biological samples.

Graphene's intrinsic properties have led researchers to utilize graphene-based supports for TEM imaging to characterize biological specimens. Jeon et al.[32] used a graphene-coated grid to image unstained proteins, achieving improved contrast and resolution in densely populated proteins. Theoretical calculations have shown an increase in image contrast of up to 7.9 times higher for graphene supports (unstained samples) compared to traditional carbon films of thickness 3 nm (negatively-stained samples). However, experiments have shown a reduced imaging resolution of graphene supports compared to conventional negatively-stained images for biological samples of low density. Also, according to [33], avoiding the use of staining increases the probability of a sample collapse due to the lack of protection from heavy metals. This was not the case in the study of Jeon et al. [32], since proteins retain their stability during imaging. All in all, Jeon et al. have found convincing evidence that graphene has a substantial advantage in imaging proteins as the mass thickness increases compared to conventional TEM procedures.

Graphene can also enable the study of biological structures in their physiological conditions (liquid buffer solutions) and not in cryo-state, which is sometimes used for conventional TEM procedures. Cryo-TEM conditions require the use of expensive equipment and delicate procedures, and the rea-

son for its application is to minimize the damage encountered in the sample when subjected to high vacuum conditions. The use of graphene-based grids in physiological conditions because of the high thermal and electrical conductivity of graphene that reduces radiation damage. The study of ferritin enclosed in a graphene sandwich, conducted by Wang et al.[34] enabled increased protection in higher electron dosage rates compared to conventional methods. On the other hand, measurements of longer duration under high electron dosage rates also imposed damage on the samples on both carbon and graphene-coated grids. Another downside of graphene support, in this case, was its interaction with the protein that changes the local atomic configuration of the protein, thereby denaturing the protein. The functionalization of graphene can be used to minimize the damage caused to the atomic structure of the proteins. In a study by Shan, C. et al.[35], the addition of poly-l-lysine (PLL) coating provided graphene with a biocompatible environment, minimizing graphene's effect on the biomolecules' structural arrangement. The active amino groups present in PLL acted as linkers for the immobilization of biomolecules. At concentrations as low as 0.5 mg/mL, a stable functionalized graphene surface was fabricated and can be stored for several months without any structural changes.

The use of the graphene liquid flow cells was studied in [36], where dsDNA were adhered to Au nanocrystals (create high contrast) for improved resolution of the structural details of dsDNA. The experiments have found no influence of the liquid pockets on the dynamics of the Au-dsDNA conjugates that managed to retain their stability over prolonged periods. The dosage rate used for the experiments has managed to surpass the critical dosage for biological molecules ($60 - 100e^{-}/\mathring{A}^2 \cdot s$). The 3D motion of the Au nanocrystals bonded together via dsDNA linkers is portrayed in Figure 2.12. However, an electron beam power of 200 kV enabled imaging for about 2 minutes since heating from the electron beam evaporated the liquid between the graphene layers, causing them to collapse together. Furthermore, the coating of DNA origami nanostructures with monolayer graphene results in a substantial increase in the structural stability of DNA origami. According to [31], coating DNA origami with a monolayer of graphene eliminates the effect of mechanical wear or solution phase processing that occur during imaging. Their results have shown a 30 times increase in the damage threshold of graphene-coated DNA origami compared to DNA origami deposited on bare silicon. Also, exposure to deionized water was less significant on graphene coatings, since only after 24 hours, graphene starts to wrinkle and causes damage to the structural integrity of the DNA origami.

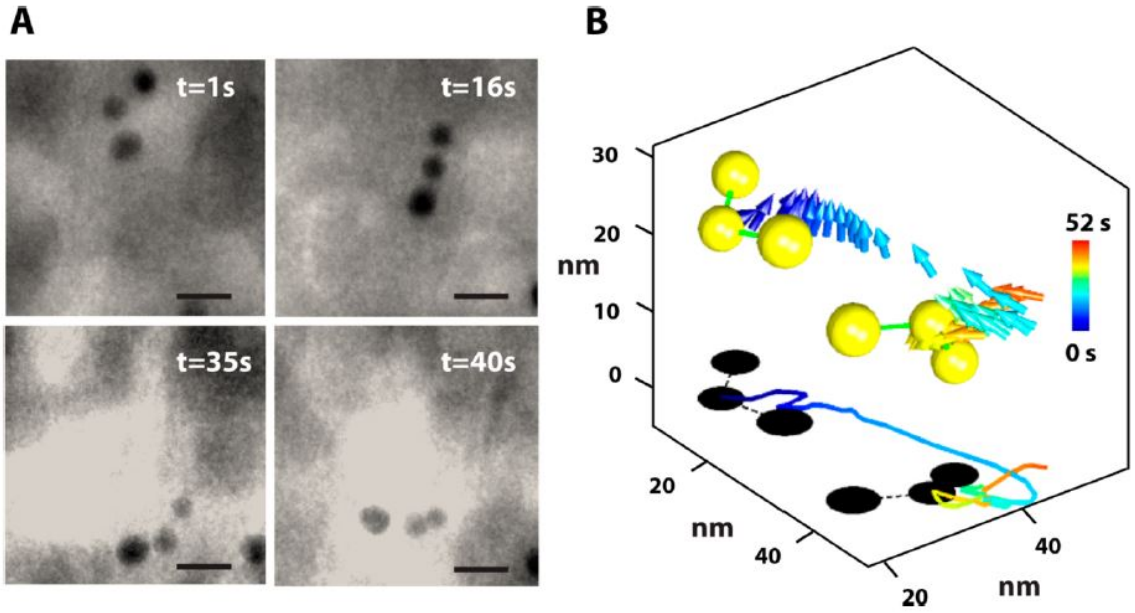

Figure 2.12: A) Images taken at different times during imaging of a trimer (3 Au nanoparticles connected by dsDNA linkers). B) The rotational (arrows) and the translational (dots represent the central nanocrystal) motions are reconstructed for the 3D motion of the trimer. The yellow spheres with the green lines represent the configuration of the trimer at times of 1 and 40 seconds. Adopted from [36].

2.2.2 Interactions of DNA origami and Graphene

One of the questions of this project is to examine whether graphene or other 2D materials can be utilized as a substrate for the characterization of dynamic DNA origami nanoactuators under TEM imaging. AFM could also be a valuable tool for evaluating the interaction of DNA origami with different substrates. Factors such as the roughness, flatness, and cleanliness of the surface could increase the deformation and/or decrease the adhesion of DNA origami.

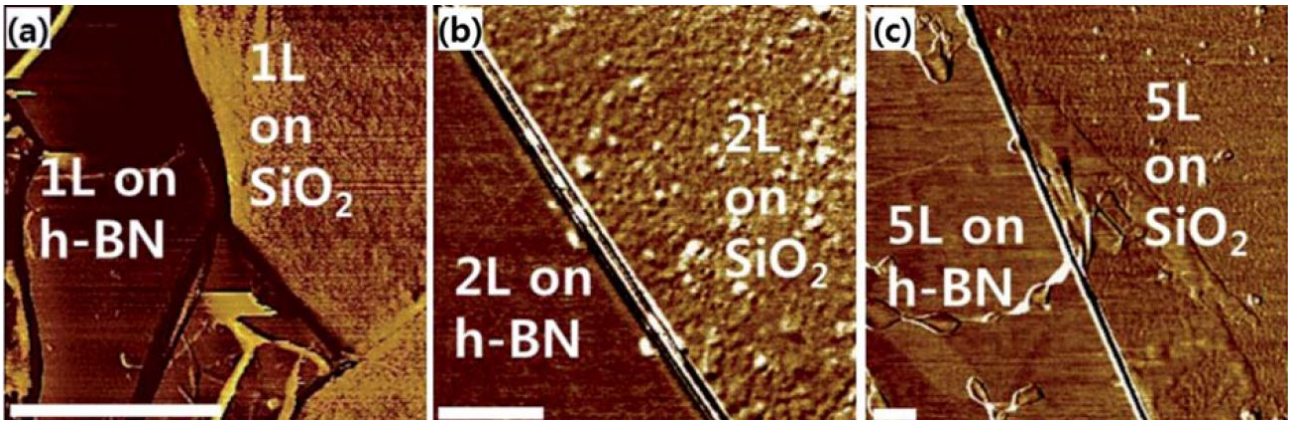

Figure 2.13: AFM images of the surface topology of a) monolayer, b) bilayer and c) 5-layer graphene on hBN and Silicon Dioxide (SiO_2). Scale bar = 500 nm Adapted from [37].

According to [38], the substrate should be as flat as possible, since corrugated surfaces decrease the van der Waals interaction energy by changing the shape of the graphene sheet such that it mimics the surface morphology. The effect of surface morphology on the adhesion force of graphene on various

substrates, including mica, was examined in [37]. The authors have found that on ultraflat surfaces, friction has no dependence on the number of graphene layers because of the flat surface morphology. On the other side, in silicon structures (rougher morphologies), the friction between graphene and silicon increased as the thickness of graphene decreased. The results imply that for thin graphene flakes, silicon would have a high friction environment, reducing the transfer yield because of the less smooth silicon surfaces (Figure 2.13). According to [39], mica shows a similar friction behaviour to atomically flat substrates like h-BN. Because of the atomically flat nature of cleaved mica and its high surface energy, there is a high probability of close contact of graphene with mica because of the reduced protrusions or defects in the graphene layer. In both [37] and [38], graphene was transferred using the mechanical cleavage method, which will be explained in the Methods Chapter. Furthermore, Lui et al.[40] have also suggested that the deposition of graphene on atomically flat substrates is crucial to decrease the number of defects in graphene flakes. The authors use a similar method to [37] for the deposition of graphene on mica, however, they perform the process in a glove box with water and oxygen concentrations below 1 p.p.m because of mica's strong interactions with water, carbon dioxide, and hydrocarbons.

The flatness of graphene supported on mica observed in various articles is crucial in allowing sufficient contact of DNA origami with the surface. The interaction of DNA origami on graphene and mica was evaluated in a study by Green, N. S et al.[41]. After transferring graphene into mica, the deposition of DNA origami was measured on both substrates (graphene, mica). Chemical Vapor Deposition (CVD) graphene was transferred on mica using the wet transfer PMMA coated graphene layer procedure, described in detail in [42]. To get rid of transfer residues, the sample was rinsed with acetone followed by annealing at 400°C. The results of AFM imaging on the graphene-mica boundary have shown a great affinity of DNA origami to graphene because of the $\pi - \pi$ stacking off the graphene layers with the aromatic purine and pyrimidine DNA bases[2]. In the experiments, there is evidence of DNA origami becoming ssDNA or being heavily distorted on Highly Oriented Pyrolytic Graphite (HOPG). AFM measurements depicted 2 different height profiles of the DNA origami structures, in which their height difference matches the corresponding difference of dsDNA and ssDNA (0.3 nm[43]). On the other hand, the DNA origami structures retained their structural stability on mica substrates.

Other papers have also observed unwanted distortions in the origami structures. Kabiri, Y. et al.[44] tried to image DNA origami nanostructures on a substrate containing graphene on amorphous carbon supports and compare it with liquid AFM imaging on mica. Measurements were also performed using advanced TEM techniques. On mica, there is a slight distortion in the aspect ratio of the DNA origami nanoarchitectures because of incomplete immobilization. The distortion, however, in AFM imaging was much less than the distortion occurring in the nanostructures deposited on graphene substrates. White blobs, crumpled configurations, and the DNA origami nanostructures' shapes are hardly identifiable as plates during imaging were some of the observations of the deposition on graphene. Changing Mg^{2+} concentration, cleaning graphene, and removing EDTA from the buffer failed to minimize the deformations of the DNA origami. The results suggest that graphene is the driver of the unwanted deformation of the nanostructures. In an effort to decrease the distortion of the DNA nanostructures, graphene was functionalized with poly-l-lysine to minimize the unfavourable interactions between HOPG and DNA. The measurements have shown a reduction in the deformation of the structures, and structural details like the internal cavities became visible. However, there was still a noticeable deformation in the origami nanoarchitectures compared with mica.

DNA origami without any chemical functionalization has been unable to contain its original structure upon deposition on graphene. An advantage of DNA origami is the ease and the implementation of chemical functionalization, and it can be used to enhance the immobilization properties of the nanostructures. Kaminska, I. et al.[45] have used pyrene molecules to immobilize the DNA origami on a graphene substrate. In theory, pyrene hybridizes the DNA origami and interacts with graphene via $\pi - \pi$ bonding. Therefore, DNA strands avoid getting into direct contact with graphene. After incubation of pyrene-modified fluorescent molecules at binding sites of DNA origami for 2 hours, a

DNA origami nanopositioner was used to transfer single dye molecules at controlled distances from graphene (Figure 2.14). However, no indication of the nanopositioner's shape attached to the graphene support was given, therefore no evidence supporting the efficacy of pyrene in reducing deformation can be found.

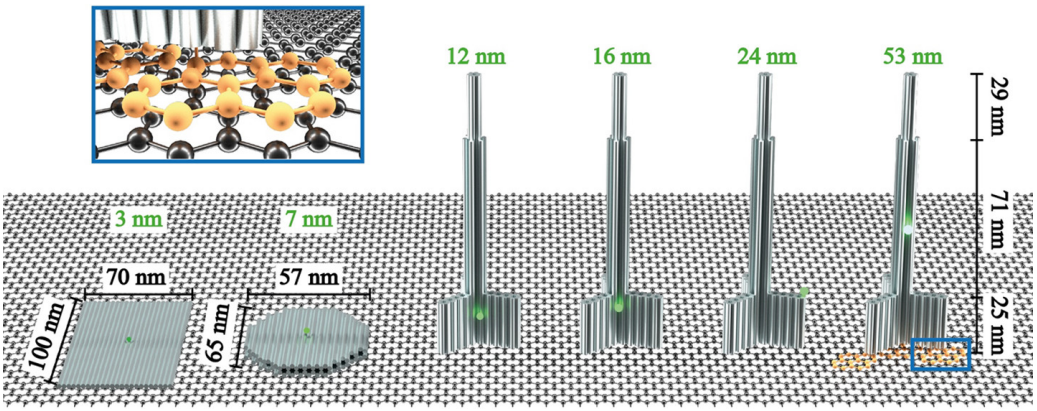

Figure 2.14: The nanopositioners shaped in a rectangular-, disc- and pillar-like structures and there were attached to the graphene via pyrene-modified DNA origami. The numbers in green mark the height at which the fluorophore is placed. The blue frame depict the pyrene-modified DNA strands (orange) and their interaction with graphene via $\pi - \pi$ bonding. Adapted from [45].

Contrary to the previous results, Brintlinger et al.[46] did not observe any significant deformations in triangular DNA origami structures imaged in high-angle annular dark-field imaging, a Scanning Transmission Electron Microscope technique. They have also used energy dispersive x-ray spectroscopy to characterize chemically unstained DNA triangles. The triangles were noticed without significant deformations, while the internal cavity remained visible. Buckhout-White, S. et al.[47] have also tried imaging unstained DNA origami under TEM. The DNA nanostructures were deposited in suspended graphene layers. The graphene was CVD grown and was transferred to silicon using wet transfer followed by thermal annealing at 300 °C. The surface was functionalized with poly-L-lysine and rinsed with deionized water to get rid of residual salts. Although the visibility of the structure is not very good, the distortion appears insignificant (Figure 2.15). The authors predict that optimization of the parameters of TEM imaging could lead to increased image resolution.

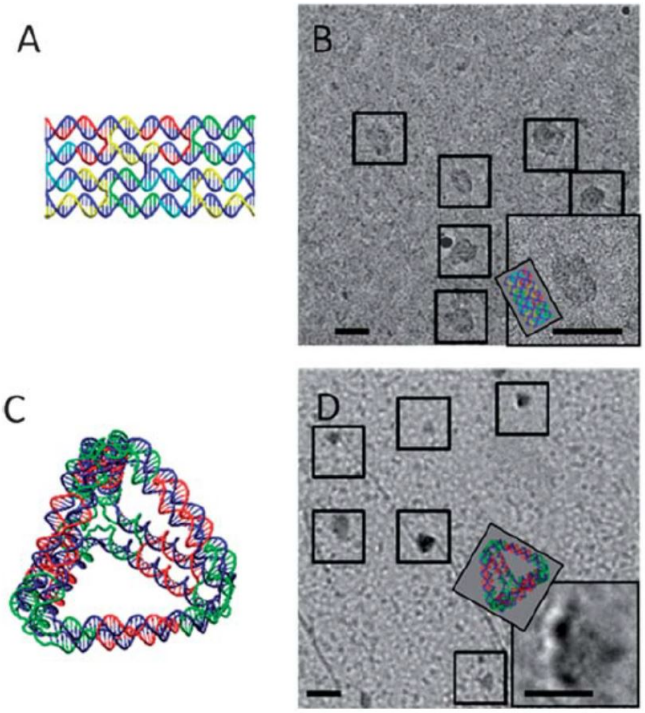

Figure 2.15: DNA strand structure and TEM images of rectangular-(A-B) and triangular-shaped (C-D) DNA origami. The substrate used in the study was graphene functionalized with PLL. The samples were unstained. Scale bars = 20 nm. Adapted from [47].

In a study by Husale, B. S. et al.[2]., the thickness of graphene affected the shape that ssDNA occupies during deposition. They have noticed that short ssDNA strands prefer to adhere to thicker and wrinkly graphene shapes. DNA strands prefer the wrinkly structures of the dangling carbon ends at the edges. However, at about 7 ± 1 layers, ssDNA strands saturate the surface. Figure 2.16 shows the extent of ssDNA surface coverage on graphene with varying graphene thickness.

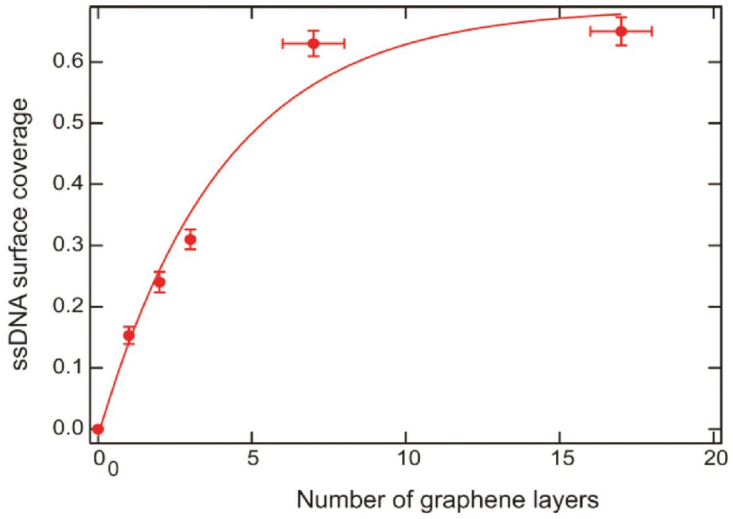

Figure 2.16: Graph showing the relation of ssDNA surface coverage in relation to number of graphene layers. Adapted from [2].

On a different approach, Akca et al. [48] tried to characterize the chemical interaction between DNA

and graphene and obtain a deeper understanding of the bonding involved. As other papers suggested, the $\pi - \pi$ stacking of graphene is the primary driver of DNA interaction. Consequently, ssDNA binds strongly to graphene compared to dsDNA since more bases are left exposed to graphene. Additionally, in dsDNA, the nucleobases are joined by hydrogen bonds to their complementary base pairs, therefore it requires more energy to break the dsDNA strands. Another factor examined by the paper is the hydrophobicity of the nucleobases. As observed in [49] and [50], the hydrophobicity of the bases falls in the order: G > A > T > C. Therefore, the G nucleobase binds more strongly to graphene than the other 3 nucleobases. Although adjusting the nucleotides is difficult to control, hydrophobicity might affect the interaction of graphene with DNA origami.

2.2.3 Ultrathin Materials used for preparation of the liquid cells

2D materials, except graphene, could provide an alternative option in fabricating liquid flow cells. Transition Metal Dichalcogenide Materials, also known as TMDC, are an intriguing type of material used in optoelectronics, sensors, energy conversion and storage devices [51, 52]. MoS_2 is the most commonly used and has relatively high stability compared to other TMDC materials[53]. MoS_2 has a stack arrangement where a positively charged Mo atomic layer is sandwiched between 2 negatively charged S layers. High-in-plane mobility, large current on/off ratio, and high photoresponsitivity [54] are some of MoS_2 intriguing properties. An interesting feature of MoS_2 is the change of its band structure from indirect (1.2 eV) in its bulk configuration to direct (1.8 eV) in its monolayer form. MoS_2 crystals, like graphene, can be obtained using CVD and mechanical cleavage techniques (look in [53] for more details).

Yang, J. et al.[55] was the first to use MoS_2 as a material for liquid cell electron microscopy. Their transfer process (Figure 2.17) has the advantage of reducing the influence of the polymer protection layer on both the physical properties of 2D materials [56–59], and also the undesirable organic residues that might interfere with the imaging [60, 61]. The transfer yield is similar to the polymer transfer method while minimizing the degree of mechanical damage to MoS_2 (verified by FEM analysis), leading to a high transfer yield and taking much less time (less than a second). As an application, they have used the liquid cell to study the solution-phase growth of Pt Nanocrystals on MoS_2, with their results being in line with previous experiments of the same growth reaction.

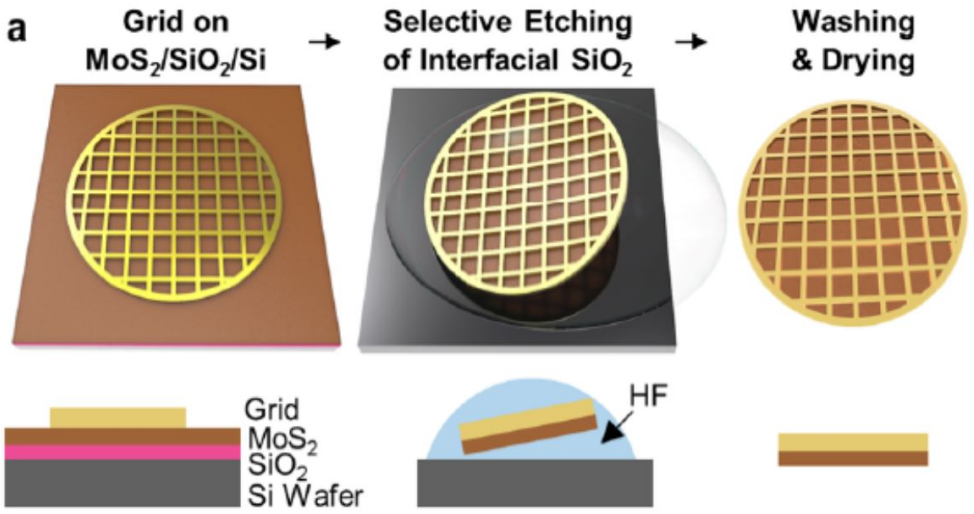

Figure 2.17: Transfer Method of MoS_2 into TEM grid. Adapted from [55].

In contrast with graphene, few papers exist that study the interaction of DNA origami and MoS_2. Zhu

et al.[62] utilized monolayer MoS_2 to construct a nanoprobe that could homogeneously detect biological molecules. The results of their experiments suggest that dsDNA has a weaker interaction with MoS_2 than ssDNA. Additionally, similarly to graphene, undesired deformations affect the structural integrity in this 2D material as well [63]. The authors report that the denaturation process occurs in 10 s, and the possible cause of this denaturation is the high polarity and hydrophilic nature of MoS_2. The nature of MoS_2 leads to the absorption of DNA through van der Waal Interactions (Figure 2.18). A functionalization that worked for graphene substrates, pyrene, also temporarily solved the denaturation problem. Despite the improved immobilization, after 24 hours, the DNA origami decomposed.

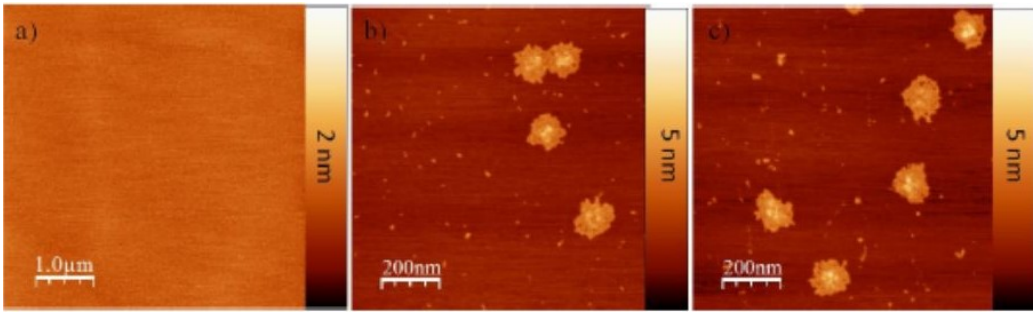

Figure 2.18: AFM images of pristine MoS_2 before, and after deposition of DNA origami. An incubation time of b) 10 s and c) 30 s was utilized. Adapted from [63].

The functionalization that worked perfectly for the DNA origami was 1-pyrenemethylamine. Even after 2 days, DNA origami nanostructures retain their structure, as they reduce the van der Waals interactions between MoS_2 and dsDNA.

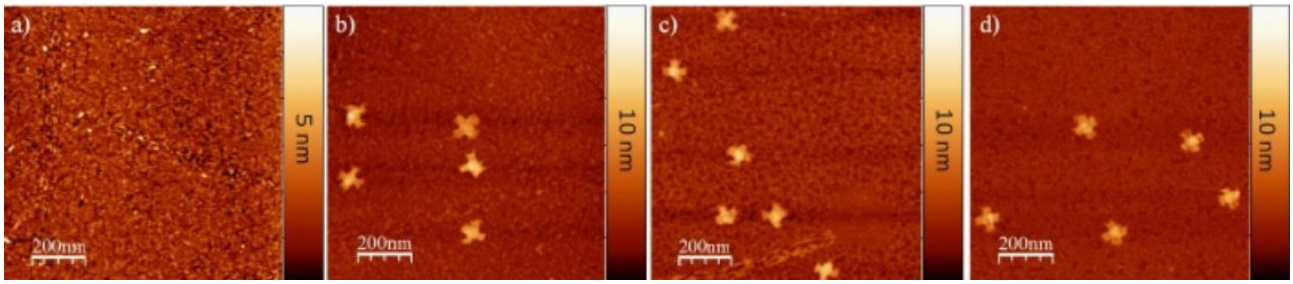

Figure 2.19: AFM images showing the structure of DNA origami on MoS_2 functionalized with 1-pyrenemethylamine. a) Before DNA origami was deposited. b-d) 0 seconds, 24 hours and 48 hours respectively after deposition of DNA origami. Adapted from [63].

Chapter 3

Research Proposal

The study of the dynamics of DNA origami's mechanisms has been a point of interest in the nanotechnology field because of their high predictability, and their potential application in drug delivery and nanopore gating. Currently, these measurements have been performed using high-speed AFM measurements that enabled researchers to successfully capture and analyze the dynamic characteristics (time and intermediate states of actuation) of DNA origami nanoactuators. However, TEM could offer increased lateral, and temporal resolution along with higher throughput. Also, TEM could increase the accuracy of imaging 3D structures due to its ability to image hidden structures. Various challenges have hindered the study of dynamic DNA origami structures in TEM, including sample preparation and reduced contrast. This might change due to the development of liquid cells that encapsulate these structures between a membrane of graphene. Using liquid cells, graphene's physical characteristics allow enhanced contrast and resolution of measurements relative to conventional carbon supports. The use of graphene could also significantly reduce the invasiveness of the imaging process because of its superior heat and electrical properties. Although promising, graphene denatures DNA origami shapes and causes unwanted deformations, affecting the dimensions of DNA origami-based structures. Similar deformations were also seen in another 2D material, MoS_2, which was used for fabricating liquid cells. Researchers have tried to functionalize both MoS_2 and graphene with different materials that helped in reducing the denaturation of DNA origami upon deposition on the 2D materials.

A literature gap can be found in the quantification of the structural integrity of DNA origami in substrates involving graphene and MoS_2. The unavailability of this quantification does not allow accurate comparison between different substrates and their corresponding functionalizations. A systematic study that uses similar substrates and DNA origami nanostructures could help in comparing the interactions of DNA origami with graphene and MoS_2. Also, parameters like the number of deformed structures, and the dimensions of each side of the origami structure could help in the appropriate selection of liquid cell material. The ultimate goal is a functionalization that would allow the mobility of DNA origami nanodevices (for dynamic studies) and no denaturation of the DNA structures. These characteristics would enable its use in liquid flow cells.

Having reviewed the advances in the current state-of-the-art, I will address the following research questions:

- Question 1: How is the structural integrity of DNA origami change upon deposition on pristine 2D materials?
- Question 2: How does the cleanliness and surface roughness affect the structural properties of DNA origami?
- Question 3: What effect do different functionalizations have on the structural properties of DNA origami?

Chapter 4

Experimental Methods

4.1 AFM Imaging

AFM imaging is the main characterization method used to image and analyze the interaction of DNA origami and different substrates. The principle of operation of AFM is dependent on the forces acting between a very sharp tip (4-50 nm in diameter) and the substrate. Different forces can cause the cantilever to deflect such as electrostatic and van der Waals forces [64]. The deflection is measured using the change in the laser reflection on top of the cantilever. A photodiode detects and measures the change in laser reflection. A computer connected to the AFM setup reconstructs the changes in reflection and outputs a representative topological image of the sample. A schematic of the principle of AFM imaging is illustrated in Figure 4.1.

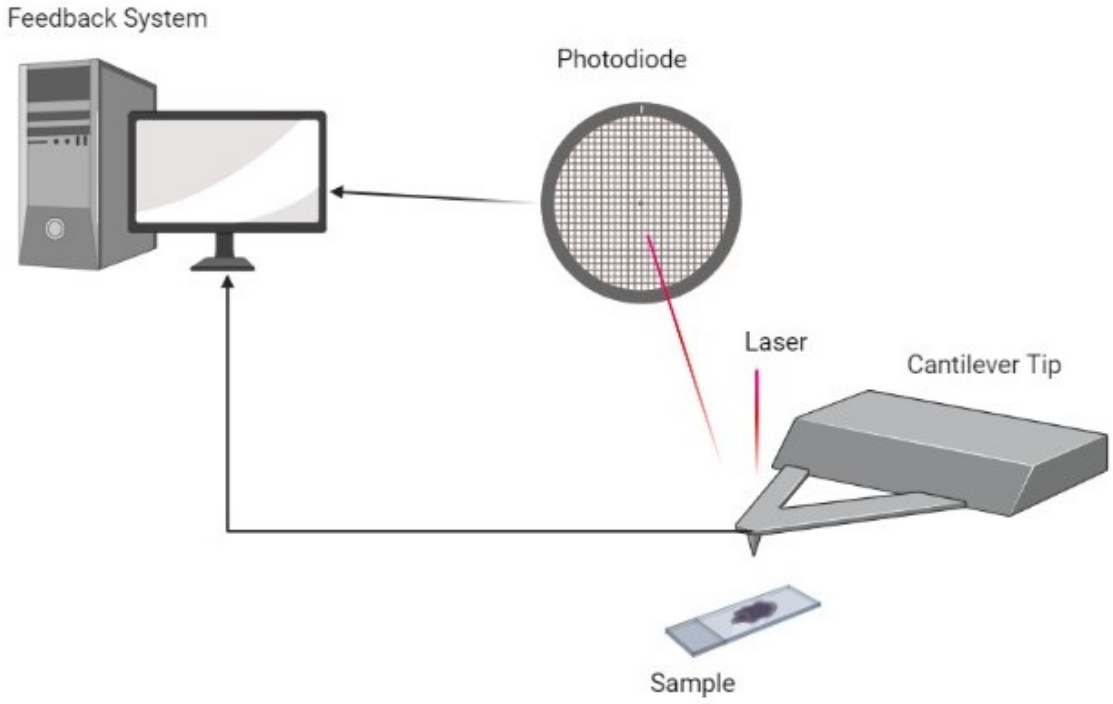

Figure 4.1: Schematic of an AFM system setup and its main components

For this project, the tapping mode was utilized. In this mode, the cantilever oscillates at a frequency close to its resonance frequency. As it approaches the surface, the oscillation amplitude alters due to the different interactions between the specimen and the tip. A feedback system keeps the amplitude of oscillations constant (known as the set point). The set point was always set to enable minimum interaction between the DNA origami and the tip. The image processing software Gwyddion allows the extraction of different parameters of the images such as the dimensions of the DNA origami triangles and minimizes any noise [65].

4.1.1 AFMs used for this project and their properties

In this project, various AFMs took measurements of DNA origami on mica and 2D materials. 3mE AFM is a nickname for the AFM found in the MNE lab of the Precision and Microsystems Engineering (PME) Department (Figure 4.3). BN AFM refers to the AFM found in the ML-1 lab of the Bionanoscience (BN) Department (Figure 4.2), whereas CD AFM is another AFM also found in the ML-1 lab of the Bionanoscience (BN) Department (Figure 4.4). However, CD AFM had a different controller than the other 2 AFMs. The properties of AFM are outlined in Table 4.1.

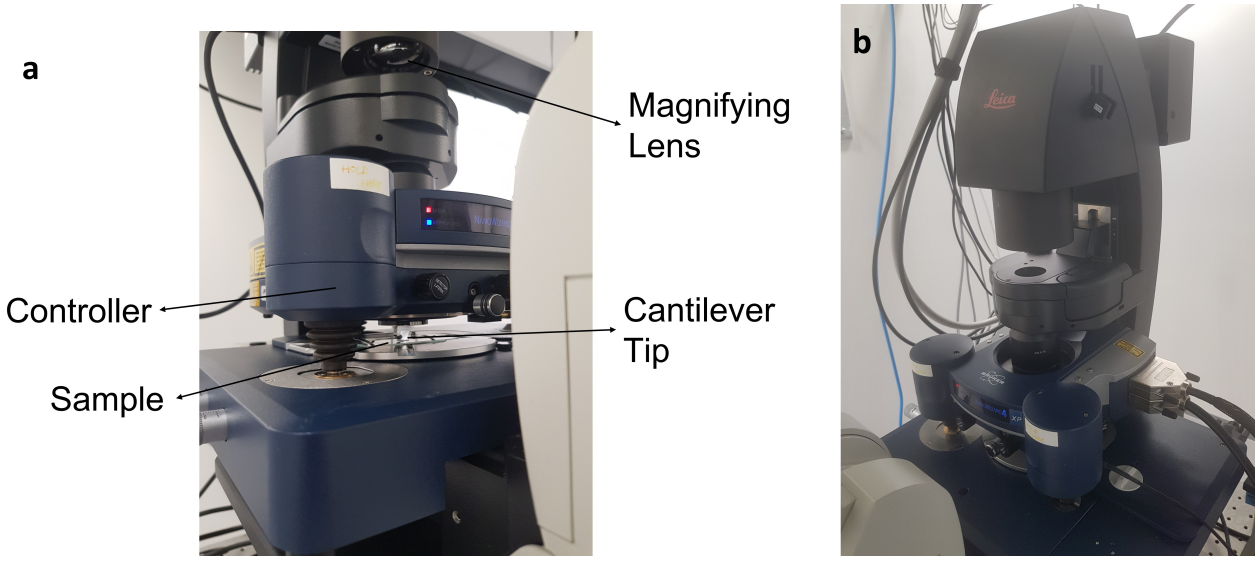

Figure 4.2: The AFM referred to as BN AFM, is found in the ML-1 lab of the Bionanoscience Department. a) Scaled-up image of the AFM controller stage b) Image of the AFM controller with the microscope on top

Figure 4.3: The AFM referred to as 3mE AFM, is found in the Micro and Nano Engineering (MNE) Lab of the PME department. It has the same controller as the BN AFM, however, both the camera and the illumination are on top of the sample. Taken from [66].

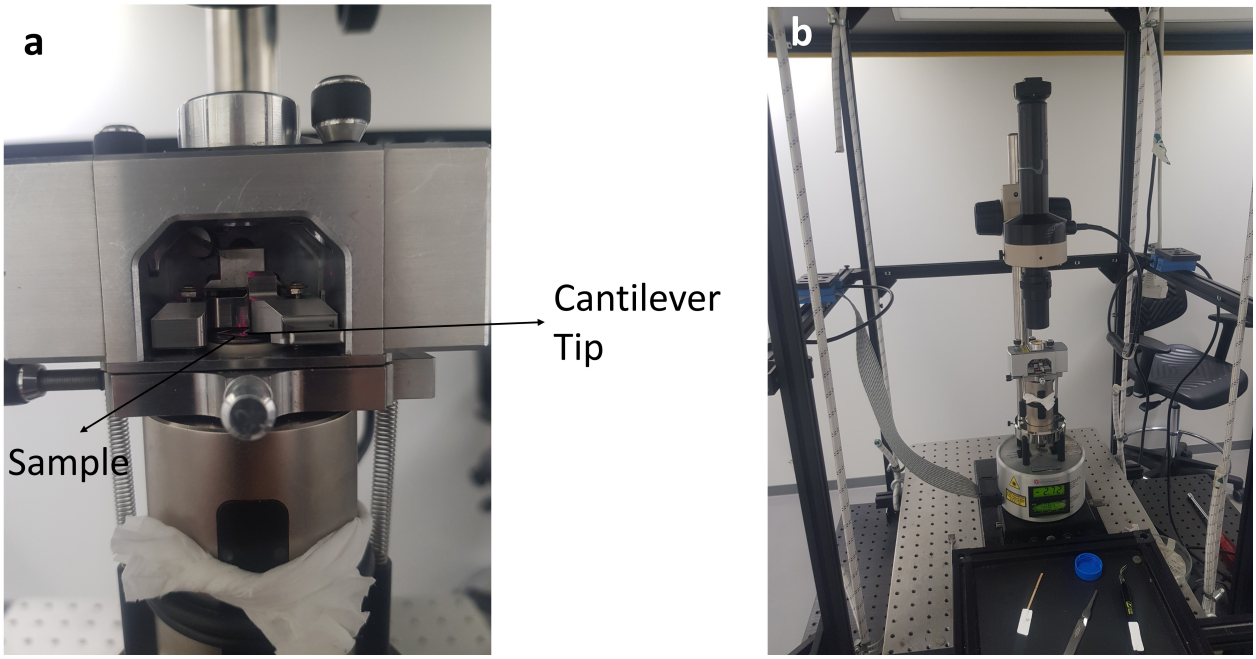

Figure 4.4: The AFM, refer to as CD AFM, is found in the ML-1 lab of the Bionanoscience Department a) Zoomed-in image of the AFM controller stage b) Image of the AFM controller with the camera and the magnifying lens on top.

AFM Nickname	BN AFM	3mE AFM	CD AFM
AFM Controller	NanoWizard 4 XP	NanoWizard 4 XP	MultiMode 8-HR
Scan Range	100 x 100 x 15 μm^3	100 x 100 x 15 μm^3	80 x 80 μm^2
Z Height Noise level	$<$ 0.03 nm RMS	$<$ 0.03 nm RMS	$<$ 0.03 nm RMS
Stage Shape	Glass Slide	Glass Slide	Circular Magnetic Base
Stage Control	Joystick or Software	Joystick or Software	Manual
Camera Position	Bottom	Top	Top

Table 4.1: Table comparing the different properties of the AFM utilized for this project.

Some other properties to be taken into account are that both the BN AFM and 3mE AFM have the option of fast scanning with speeds up to 150 lines/sec available. For the CD AFM, no scanning speed was found available, but the manual claims that speeds up to 6× quicker than conventional AFMs can be reached. The manual also says that CD AFM is designed for taking Peak Force Tapping Measurements. The properties for all the AFMs were taken from the official website of Bruker [67, 68]. Also, the cantilevers used were:

- SCANASYST-AIR HR - k = 0.4 N/m, tip radius = 2 nm
- FESP V2 - k = 2.8 N/m, tip radius = 8 nm

4.1.2 Deposition of DNA origami on mica and AFM imaging

The method utilized to image DNA origami on mica is outlined below. The buffer and the methodology were taken from [22]. The buffer and mica preparation are described in more detail in the Appendix (Section A.1).

(1) The assembly solution of DNA origami was about 136 nM. The concentration is very high, so dilution to an appropriate concentration (1-3 nM) was performed using TAE/Mg^{2+} buffer.

(2) Then, 10-30 μL of diluted DNA origami solution was deposited carefully on the cleaved mica. The volume utilized was dependent on the size of the mica. A higher size of mica would need more volume to cover homogeneously the surface.

(3) The sample was left to incubate for about 2 minutes.

(4) Mica was washed 2-3 times with 1 mL of MilliQ water.

(5) Mica was dried using a nitrogen gun, each time holding the gun sideways and going once from the top side to the downside or vice versa.

(6) The sample is now ready for imaging.

The process steps are shown in Figure 4.5.

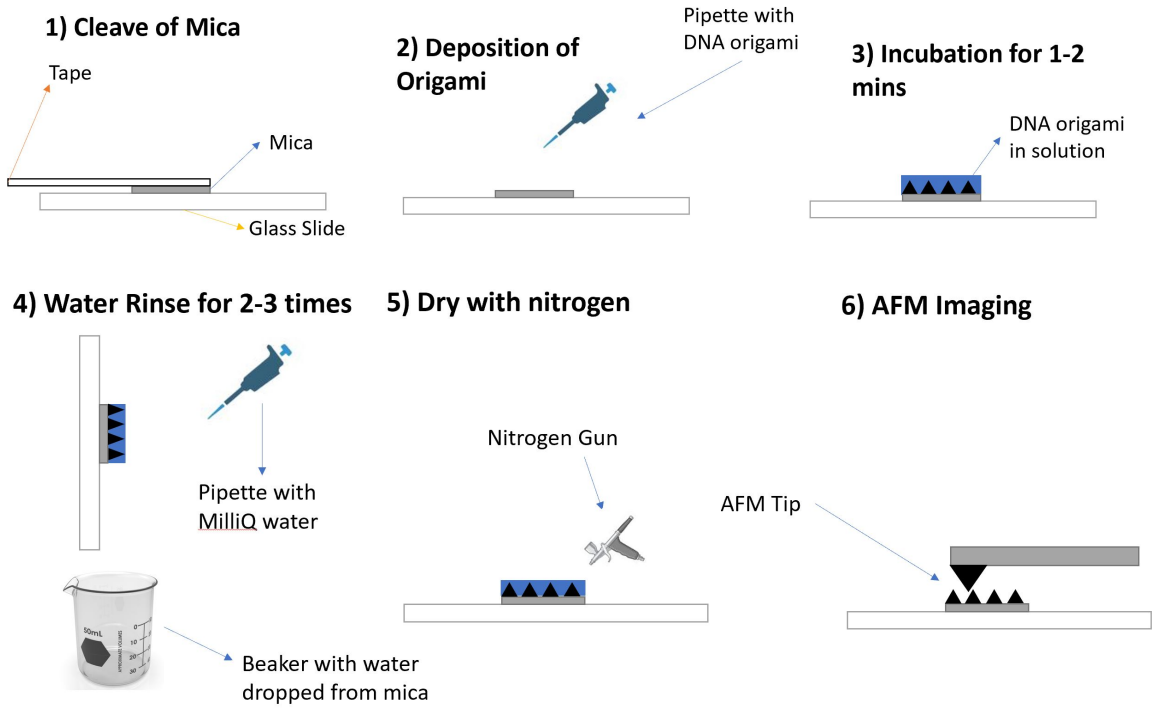

Figure 4.5: Steps taken for AFM measurement of DNA origami on mica substrate

4.1.3 Deposition of DNA origami on 2D materials and AFM imaging

(a) **No Functionalization**
After cleaving the mica and transferring the 2D materials to the mica, the preparation of the DNA origami sample was the same as in the case of bare mica. The only difference in the method was that the incubation time varied between 1 and 20 minutes.

(b) **Functionalization with Poly-L-lysine**
This functionalization was used for bulk graphene flakes on mica to allow for less distorted DNA origami on graphene.

(1) Dilute the poly-L-lysine solution (0.01 w/ v % original solution) 200 times using MilliQ water (Final Concentration = 0.00005 w/v %). The w/v % denotes the number of grams found in 1 mL of solution multiplied by 100 to find the percentage. In our case, the diluted solution was composed of 0.5 μg in 1 mL of the total solution.

(2) Drop 15-30 μL of the diluted poly-L-lysine (PLL) in the mica substrate. Incubation ranged from 1 minute to 1 hour. The incubation time and concentration were based on the papers of [22] and [47].

(3) Rinse the solution 3 times with 1 mL of MilliQ water.

(4) Dry the substrate with nitrogen.

(5) Follow steps 2-6 of the 4.1.2 Section.

4.2 Transfer of 2D materials on mica

For this project, bulk graphene and hBN flakes were deposited on mica surfaces. Mica was cleaved before transfer to allow for a clean surface each time. Mica and all the tapes are placed on clean

aluminium foil.

(a) **PDMS stamping of 2D materials**

(1) Get a supply of the desired 2D material on a tape and place another tape on top of it. Then, exfoliate it carefully.

(2) In the tape with the exfoliated 2D material, close and open it 3-4 times to ensure flakes were distributed evenly. Label this tape as 1.

(3) Transfer the contents of tape label 1 into another new tape (tape 2) and perform the same closing and opening procedure.

(4) Continue the procedure until you have 3-4 tapes. The number of tapes is dependent on the desired thickness and quality of flakes you want. Using more tapes, both the thickness and quantity of the 2D material decrease.

(5) Stick PDMS on a glass substrate.

(6) Use your final tape to transfer the 2D material into PDMS. Place the tape gently on PDMS, and use tweezers to ensure it sticks well. Then, remove it fast.

(7) Place the substrate on the stamping microscope stage and enable the vacuum option. The mica adheres to a glass slide since free-standing mica was found to stick to the PDMS stamp.

(8) Place the PDMS stamp close to the top of the substrate. They should not touch at this stage.

(9) Slowly bring the substrate closer to the PDMS while having the PDMS stamp on focus.

(10) Once they touch, continue the process until the whole PDMS stamp sticks to the mica.

(11) Slowly release the PDMS from the substrate, going very carefully when a flake is going to be detached from the substrate.

(12) Continue releasing the substrate until no adhesion between PDMS and the substrate is observed. Then, continue bringing the stage down to allow the removal of the PDMS stamp from the stage.

A visual illustration of the process and the setup is shown in the Figures 4.6 and 4.7.

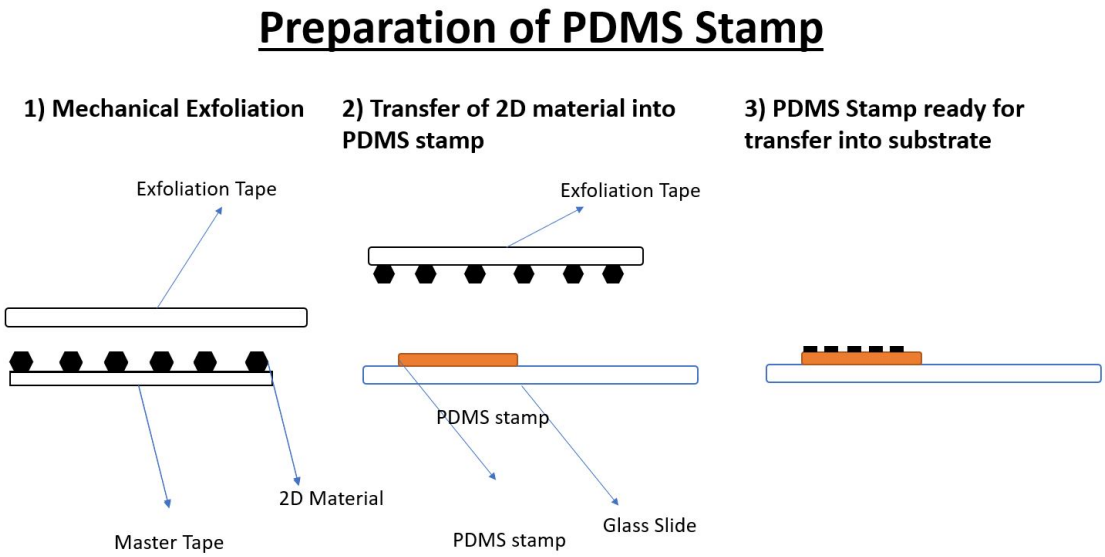

Figure 4.6: Preparation of the PDMS stamp required for transferring the 2D material

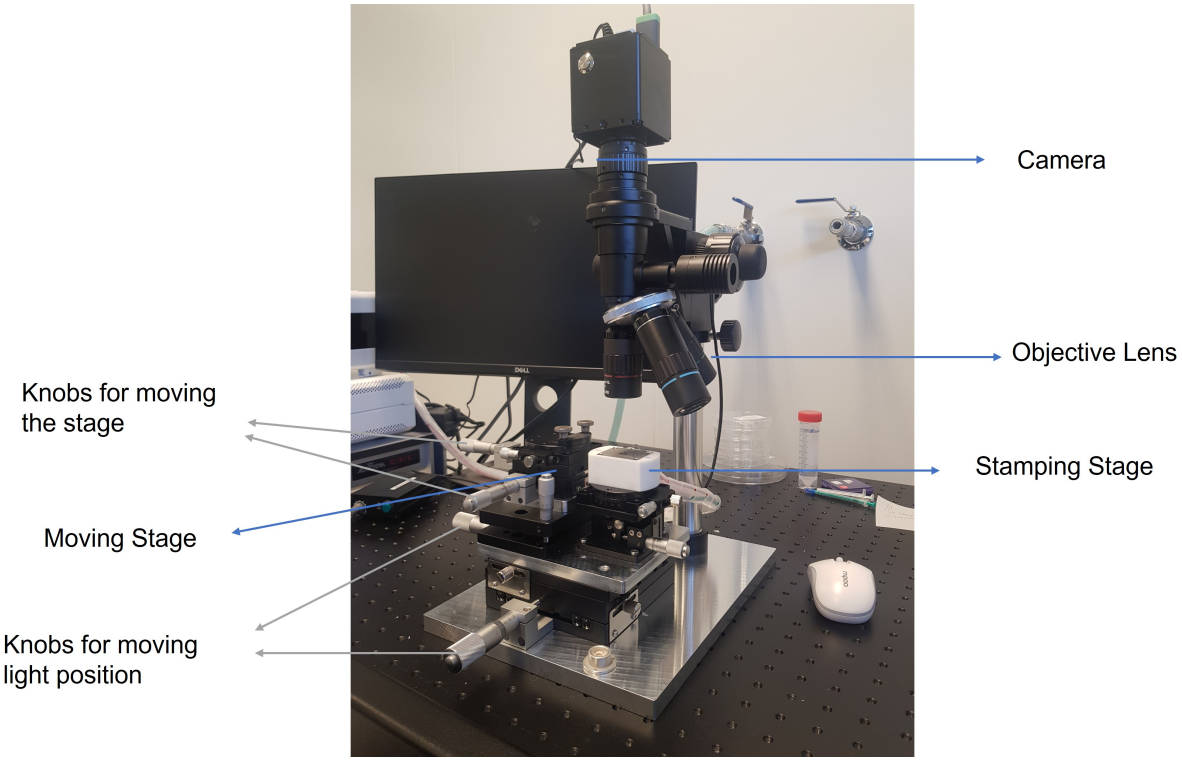

Figure 4.7: PDMS stamping setup

(b) **Direct Transfer of 2D Materials**

An alternative method used to transfer 2D materials is the direct transfer method.

(1) Follow the same procedure as the PDMS stamping procedure until step 5.

(2) Then, the last tape you extracted, without closing it and opening it again, find a spot where abundant 2D material is located and place it on top of the substrate.

(3) Slowly remove the tape, while holding the substrate in place using the tweezers. Try to minimize the interaction of the tweezers and the substrate to avoid contamination (place it near the edges).

Figure 4.8 depicts a schematic diagram of the process. Note that you should never use the same tape twice because of the contamination that might occur during the transfer of the 2D material into the substrate.

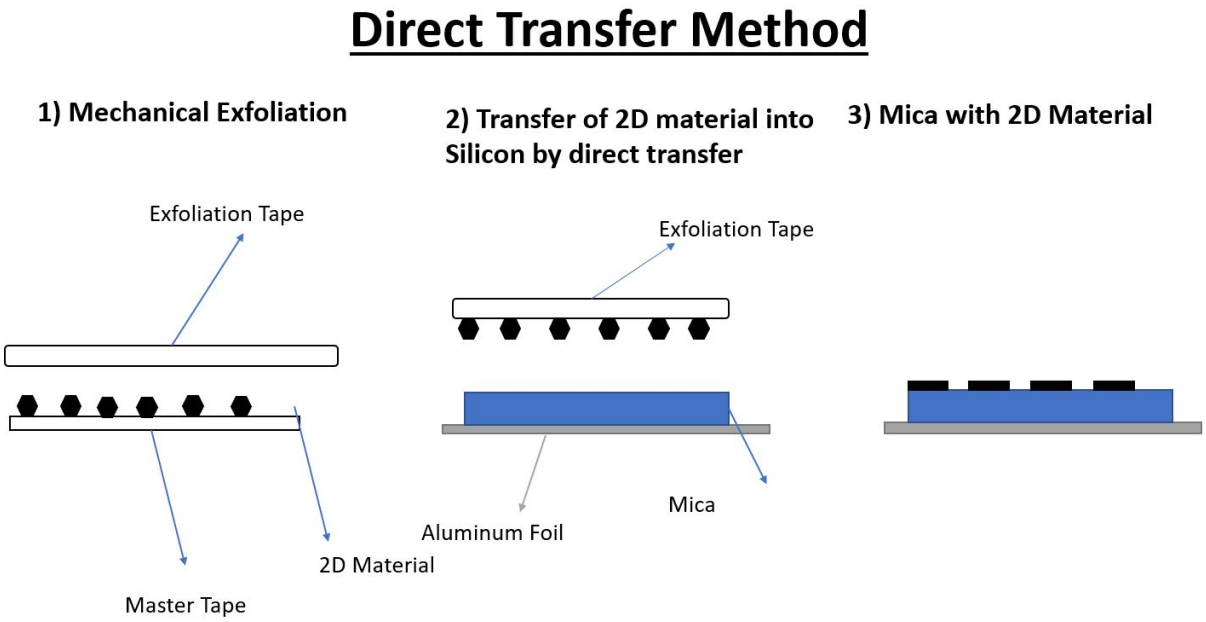

Figure 4.8: Schematic Diagram of the Direct Transfer Process

Chapter 5

Results

5.1 Characterization of DNA origami on Mica substrate

As a first step, the effectiveness of the TAE/Mg^{2+} buffer to provide DNA origami with the appropriate environment to absorb to mica was evaluated. The first measurements of the DNA origami were conducted in CD AFM with a SCANASYST-AIR HR cantilever. The images below (Figure 5.1) validate that the TAE/Mg^{2+} buffer (see Appendix A.1 for details) provides the DNA origami with an adequate positive charge to adhere to the freshly cleaved mica substrate. An incubation time of 2 minutes allowed enough time for the nanostructures to diffuse and absorb into the substrate.

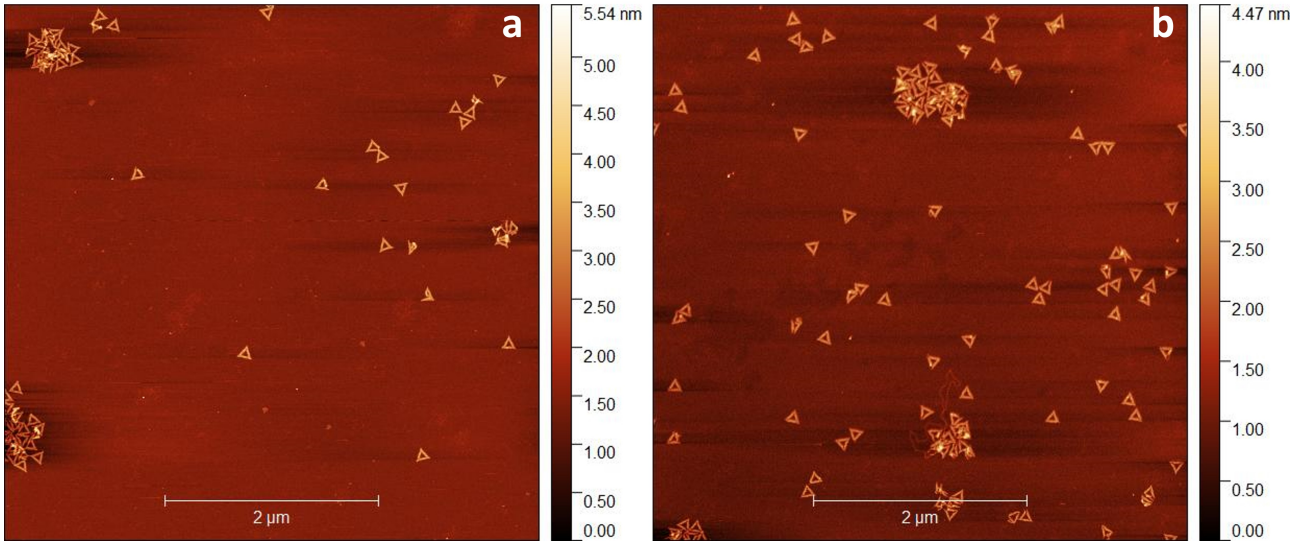

Figure 5.1: AFM images of DNA origami with concentrations of a) 1 nM and b) 3 nM on a cleaved mica surface

As expected, a concentration of 3 nM led to a significantly greater number of origami triangles than a 1 nM concentration to adhere to a 25 μm^2 area. A higher concentration led to an almost double amount of triangles in the 3 nM sample (84) compared to the 1 nM sample (45). The lack of a liquid environment and the tip interaction led to some deformed DNA origami. About 20 deformed triangles were noticed for both samples. Another reason for this potential deformation is that they did not stick strong enough to the surface, therefore drying and rinsing the sample might cause deformation to the less adhered parts. However, the last explanation is less likely since rinsing and drying removes the unabsorbed structures. An important thing to notice is the aggregates (collection of many DNA

origami nanostructures in a small region) that the DNA origami form on the surface. Aggregates are caused due to DNA's preference for adhering to other biomolecules. For each measurement, the parameters of imaging and preparation were kept constant. The scan rate was 1 line/s, 512 lines per image, and 3 rinses with MilliQ water were used. The number of lines is relatively high, and the time taken to image each line is low. The parameters minimize the interaction of the tip with DNA origami and accurately measure the structural details of the nanostructures.

After verifying that the buffer worked, a zoomed-in-image was taken so that structural details of the origami triangles could be measured (Figure 5.2).

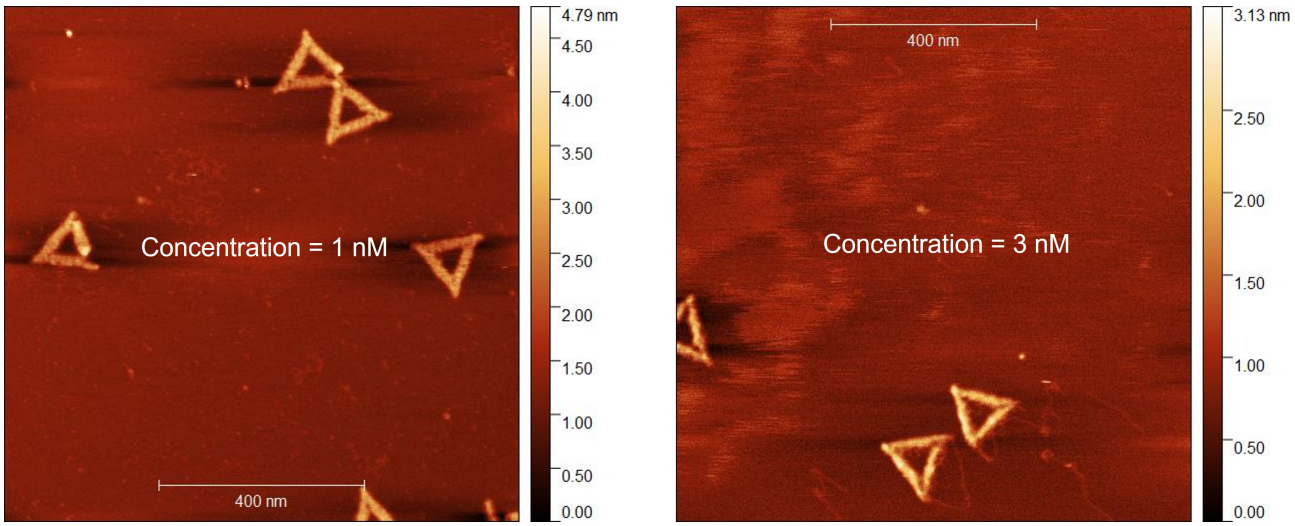

Figure 5.2: Zoomed-in images of the origami triangles. The regions used were taken from the same sample as in Figure 5.1

The dimensions of the sides were extracted using Gwyddion. The average length of each side was found to be 124.7 $\pm$ 4.7 nm. This value is very close to the expected size of the triangle (127.3 nm). For measuring the triangle sides, the lines were drawn from the exterior part of the triangle, as depicted in Figure 5.3. In addition, the range of heights for the triangular nanoarchitectures was between 1.3 and 2.5 nm.

Since the range of values for the triangle sides found varies significantly, measurements of many triangles were included in the average of the nanostructures' dimensions on different substrates. Also, the height indicates an intricate contact between the tip with the sample, with values close to 2 nm, which is representative of a 2D DNA origami nanostructure.

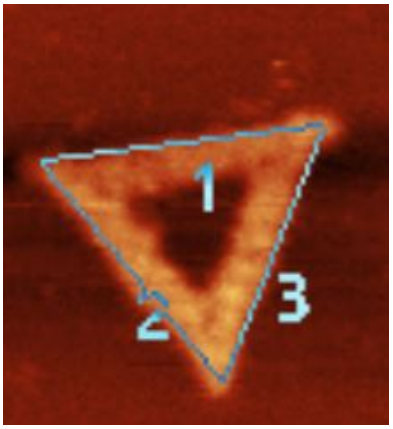

Figure 5.3: Figure showing how the lines were placed to accurately measure the side length of DNA origami triangles

5.1.1 Effect of Scanning Region Location on adhesion of DNA origami on mica

Mica is an ideal substrate for DNA origami due to its atomic flatness. However, damage to the surface is caused during sample preparation and handling. Taking a look in Figure 5.4, at the edges of the mica, there are several cracks and elevated mica regions (out-of-focus parts in the images). Cracks still exist at the centre, but no out-of-focus features are found.

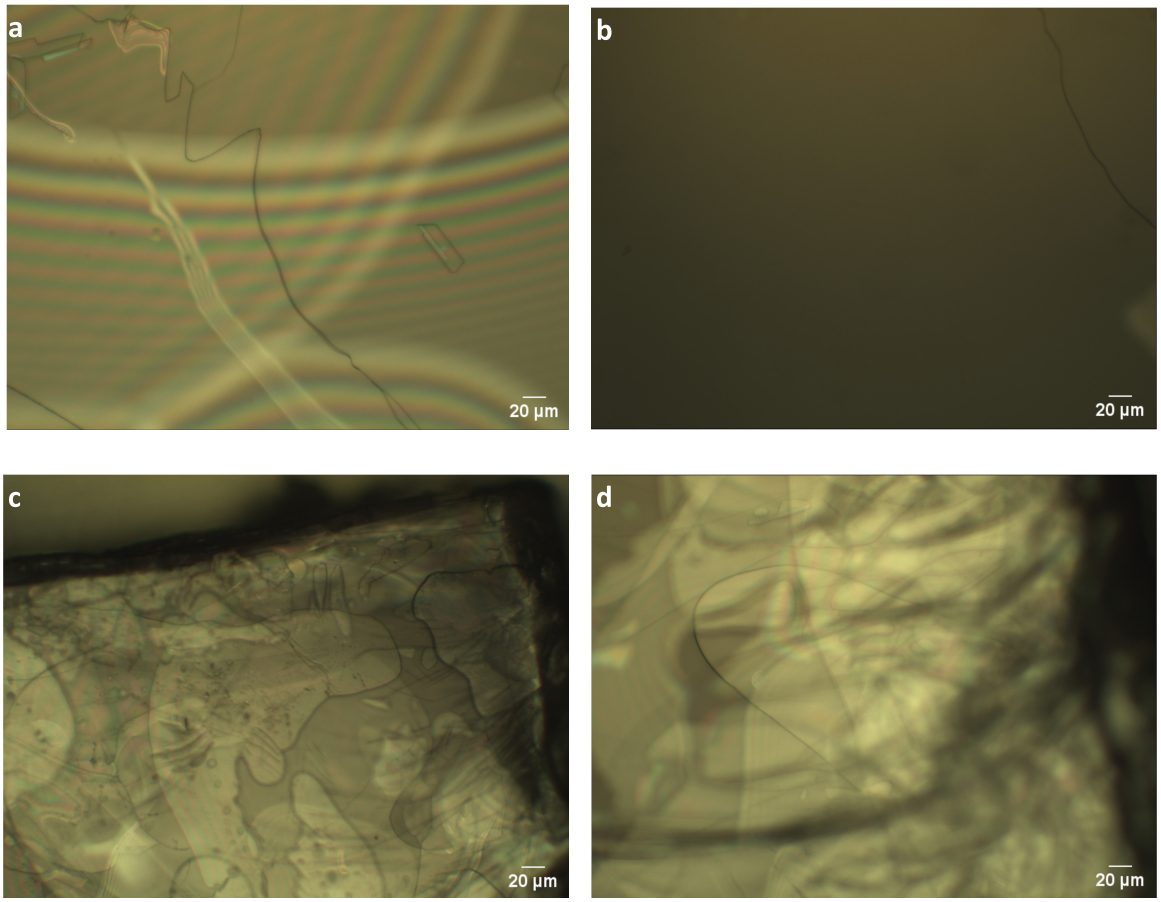

Figure 5.4: Optical Images of mica on the centre (a-b) and sides (c-d) show the differences in its morphology because of preparation. Magnification = 10 ×

To investigate the effect of the mica surface on the adhesion of DNA origami, several images were taken at different positions on the mica surface. The sample was rinsed 3 times, followed by drying with a nitrogen gun. The concentration and volume of DNA origami triangles used were equal to 1.25 nM and 15 μL respectively. This time, the BN AFM was utilized with the FESP-V2 cantilever. The most significant results are conveyed in Figure 5.5.

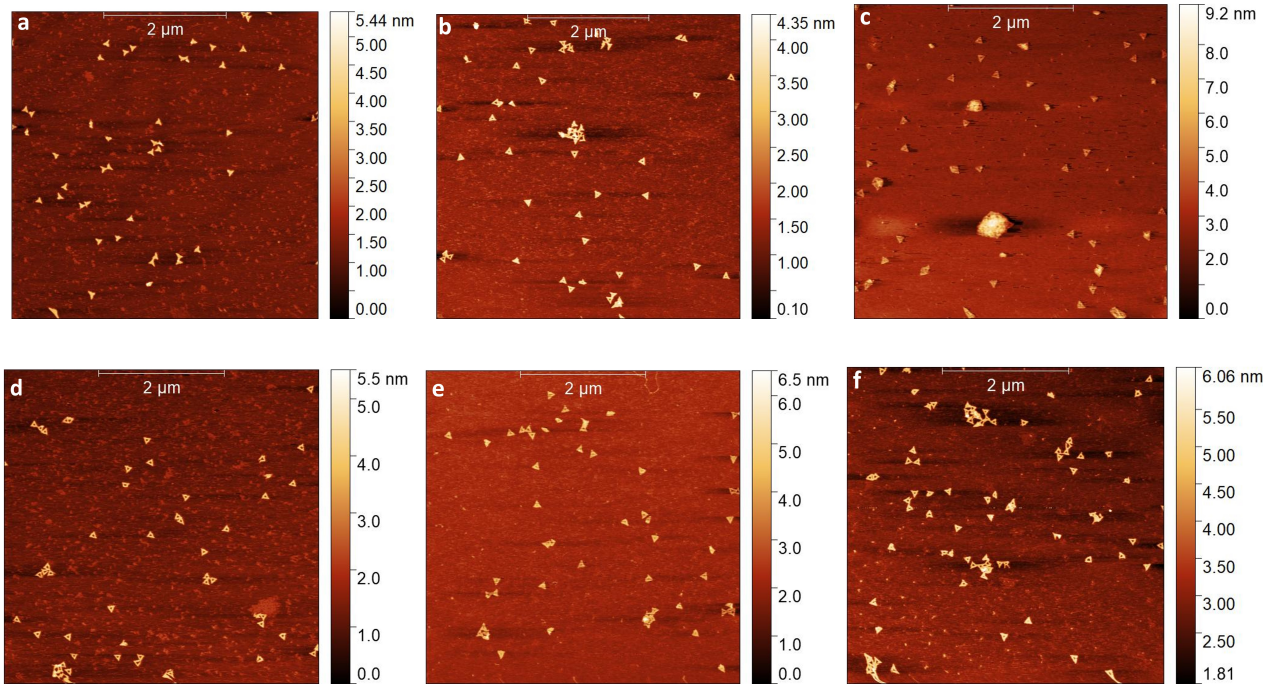

Figure 5.5: AFM measurements show the different distributions of DNA origami in various locations on mica. The top images represent measurements closer to the edges of mica, whereas the bottom ones are closer to the centre.

Even on the same substrate, different patterns of behaviour are observed in the centre of the mica (Figures 5.5d-5.5f) compared to the edges (Figures 5.5a-5.5c). The distribution of DNA origami is not as uniform since, at the sides, the surface is not as smooth and is slightly tilted. Additionally, increased buffer residue was found on the edges compared to the centre. As clearly viewed in Figure 5.5a, the cavities of the DNA origami are not visible in most of the nanostructures. A possible explanation is a high setpoint that did not allow the tip to enter the cavity between the triangle sides. The given explanation is unlikely since the same setpoint was used for all the images and most of the nanostructures have the cavity visible. The other possible reason for this observation is that the magnesium ions (positively charged) react with the phosphate backbone of the DNA strands (negatively charged), causing the cavity to disappear. Furthermore, a few nanostructures appear slightly deformed because of the unequal positive environment. As they are deposited, a lack of positive ions at specific locations causes repulsion of the DNA strands that leads to unfolding. However, one thing that can be verified from the measurement at the sides is how atomically flat cleaved mica is since mica's mean roughness was determined to be 182 pm.

These measurements convey the significance that imaging should be taken close to the centre of the mica. This will avoid the buffer residue that remains on the substrate, despite rinsing and drying.

5.1.2 Rinsing Test

The effect of rinsing on the substrate's characteristics was also examined. Parameters like the roughness, salt concentration, and the number of attached DNA origami would be used to evaluate each rinsing method. Rinsing volume varied from 0 to 3000 μL, using increments of 1000 μL. When no rinsing was applied, the incubation time was increased to 20 minutes since this was the time needed for the liquid to evaporate. This was the time when most of the liquid evaporated, as observed by optical microscope measurements that were taken in 5-minute intervals of a 10 μL droplet of a buffer solution on mica. For all the experiments, a volume of 10 μL of 2 nM DNA origami was deposited on the surface. To limit the change of parameters, the same mica surface was used for all measurements, which was cleaved each time a new measurement was performed.

No Rinsing

As a first test, the sample was left at room temperature conditions for approximately 20-30 minutes. To get an accurate outlook of mica, the images were taken at different locations, avoiding regions close to the edges of the substrate. Since the sample was not rinsed, the degree of salt and the number of aggregates are substantially higher when compared to the previous experiment (Figure 5.5). Also, another aspect to notice is that most DNA origami nanostructures do not have their cavities visible, possibly due to salt entering the triangle's cavity and not allowing the cantilever tip to reach the mica substrate.

Because of the increased aggregates and salt on the surface, no rinsing does not allow an accurate representation of DNA origami triangles on mica. This experiment verifies the importance of rinsing to remove unattached nanostructures and buffer residues.

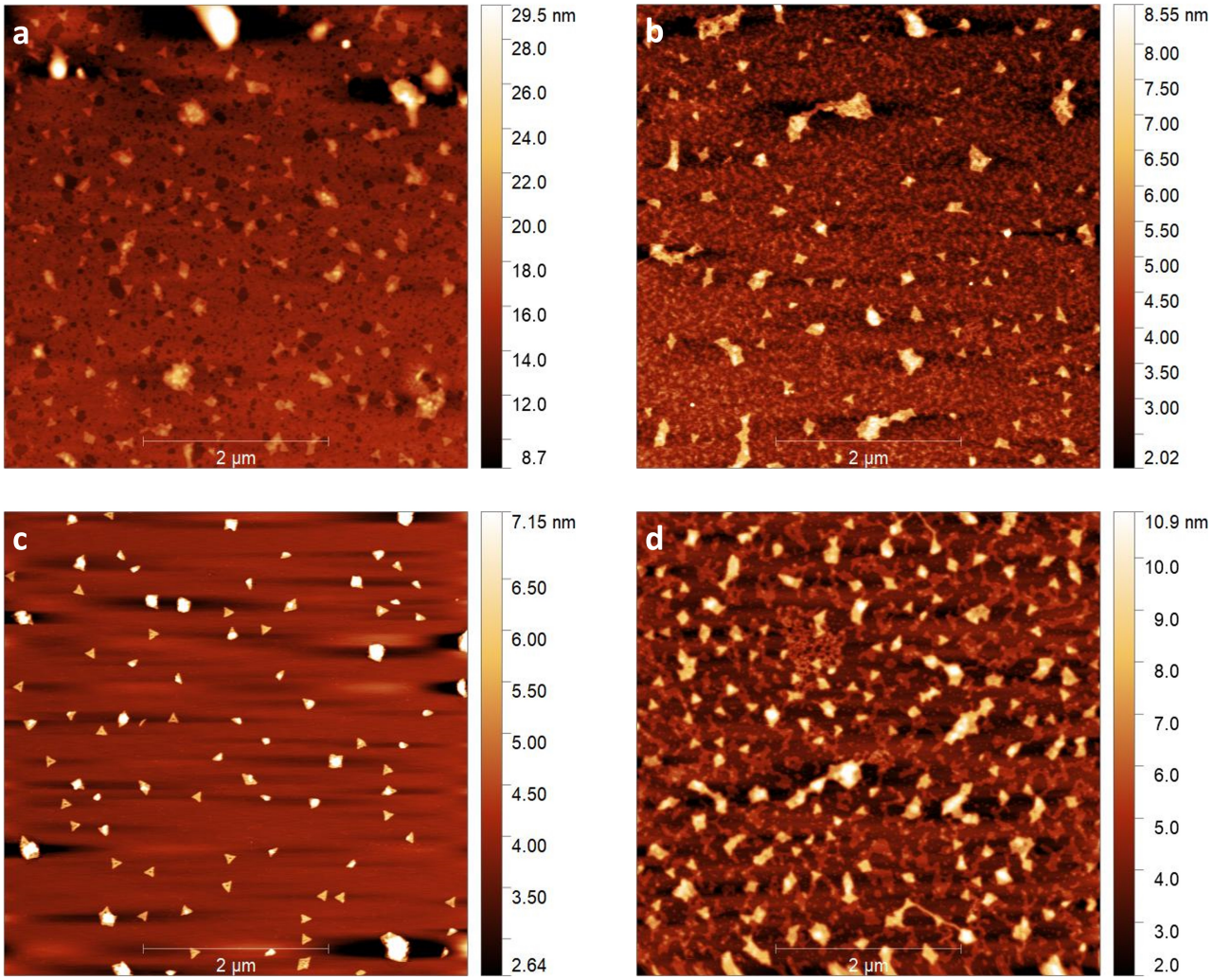

Figure 5.6: Images that show the distribution of DNA origami in different locations on mica. The DNA origami/buffer solution was left to evaporate on the surface.

1 Rinse

In the following experiment, mica was rinsed once with 1000 μL of water. Rinsing once managed to get rid of the salt, and the triangles are less deformed with fewer aggregates being formed in the images. Additionally, the cavities of the triangles can be measured again, as can be seen in Figures 5.7a and 5.7c. However, at some locations, aggregates form and buffer residue still remain in the surface (Figures 5.7b and 5.7d). The accumulation of salt that prevents the visibility of origami triangles is most clearly observed in Figure 5.7d.

The results suggest that an inadequate water volume was used to rinse away buffer and unattached DNA origami nanostructures. An increased volume of water would have allowed a decreased probability of aggregates and buffer residues on mica.

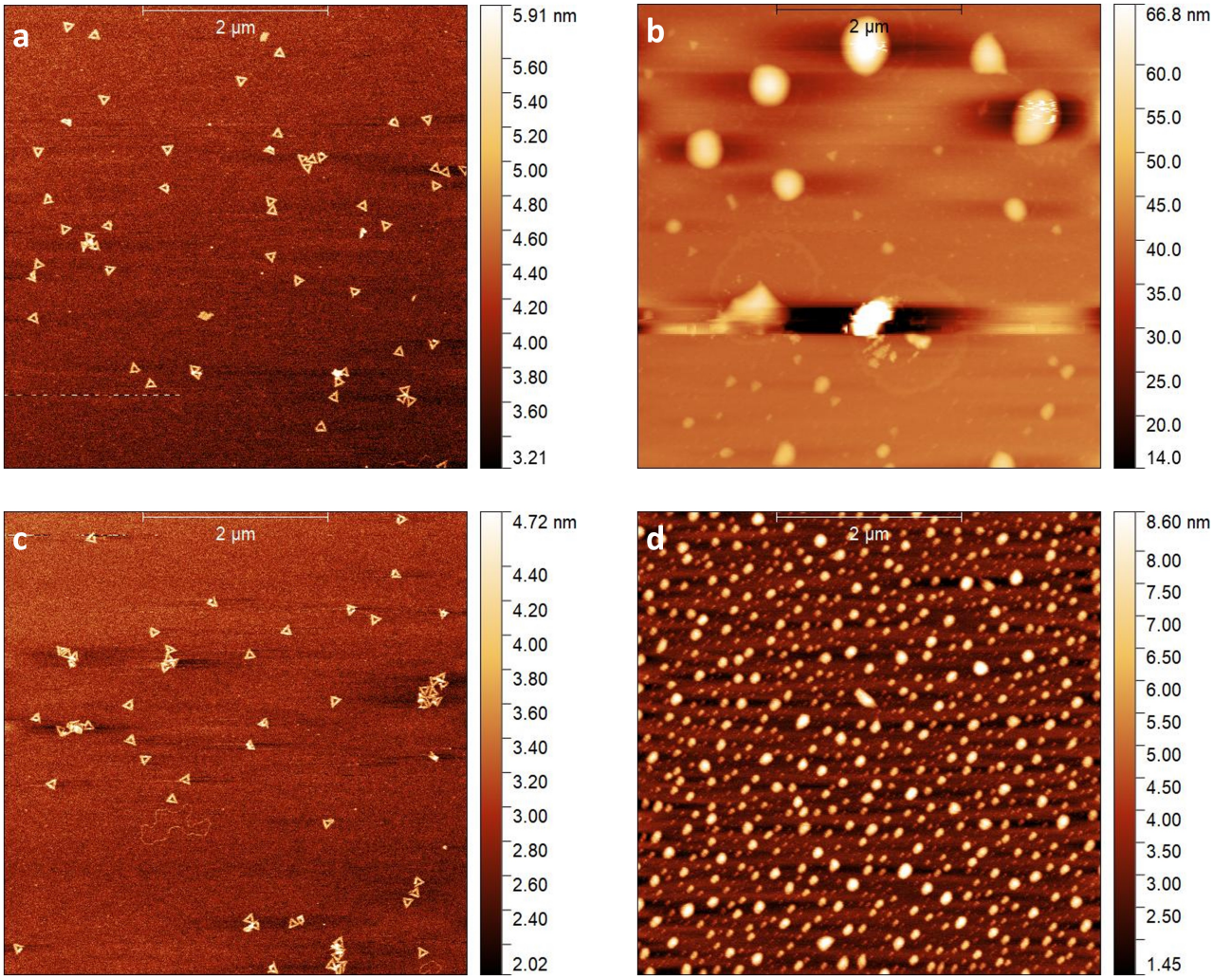

Figure 5.7: AFM measurements that portray the distribution of DNA origami nanostructures in mica. Rinsing once using a solution of 1 mL of MilliQ water was followed by drying the surface with a nitrogen gun.

2 Rinses

Finally, rinsing twice with 1000 mL of MilliQ water was conducted. The buffer residue left on the surface and the number of aggregates reduce significantly. As fewer aggregates form, the number of origami triangles has increased compared to the lower rinsing cases. The cavities of the triangles are visible in most of the triangles. On the other side, similar to the other situations, there is still salt accumulation and deformed DNA origami structures. In some cases, the lack of adequate positive charge causes DNA origami nanostructures to unfold, an effect most clearly seen in Figure 5.8d. In the same Figure, we can see some formation of ssDNA structures, noticeable at the bottom of the image.

This result portrays that even if adequate rinsing is conducted, salt residues might remain in specific regions, whereas nanostructures can unfold due to inadequate positive charge in the deposited region.

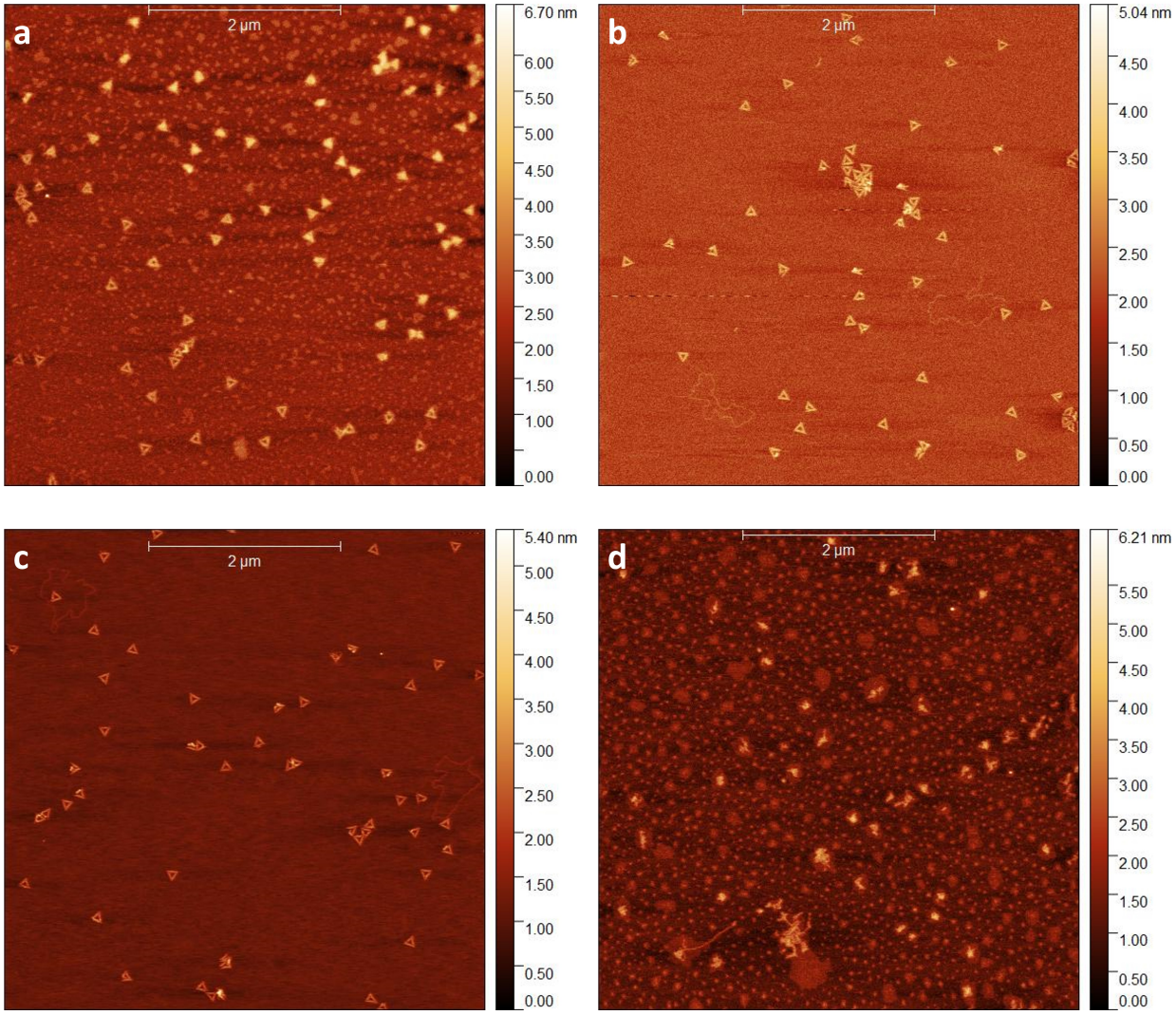

Figure 5.8: AFM measurements convey the distribution of DNA origami in various mica regions. This time, the mica was rinsed twice with MilliQ water.

Comparing all the results gathered from 0-3 Rinses, rinsing $2-3$ times removes unattached DNA origami nanostructures and the majority of the buffer residue on the mica. This methodology provides a clean surface that would allow accurate imaging and characterization of DNA origami nanostructures. The results of the rinsing test are summarized in the table below (Table 5.1). A more detailed table of all the results attained can be found in the Appendix (Table A.1). The concentration and volume of DNA origami solution used for all cases were equal to 2 nM and 10 μL respectively.

Rinses	**Number of Triangles**	**Cavities**	**Number of deformed Triangles**	**Aggregates**
0	52.2	04.2	25.4	09.8
1	21.2	16.0	04.2	08.6
2	56.3	45.0	07.3	02.5
3	65.0	56.2	11.4	03.0

Table 5.1: Table that evaluates the effect of rinsing on DNA origami adsorption

Also, the relationship between the number of rinses and the roughness was examined. The Root Mean Square (RMS) roughness measurements were taken from 6 images for each rinsing condition. For each

image, the average of 3 random regions distributed in different mica areas of 0.5 x 0.5 μm, where no DNA origami nanostructures were attached, was determined. Figure 5.9 demonstrates the relationship of surface roughness to the number of rinses.

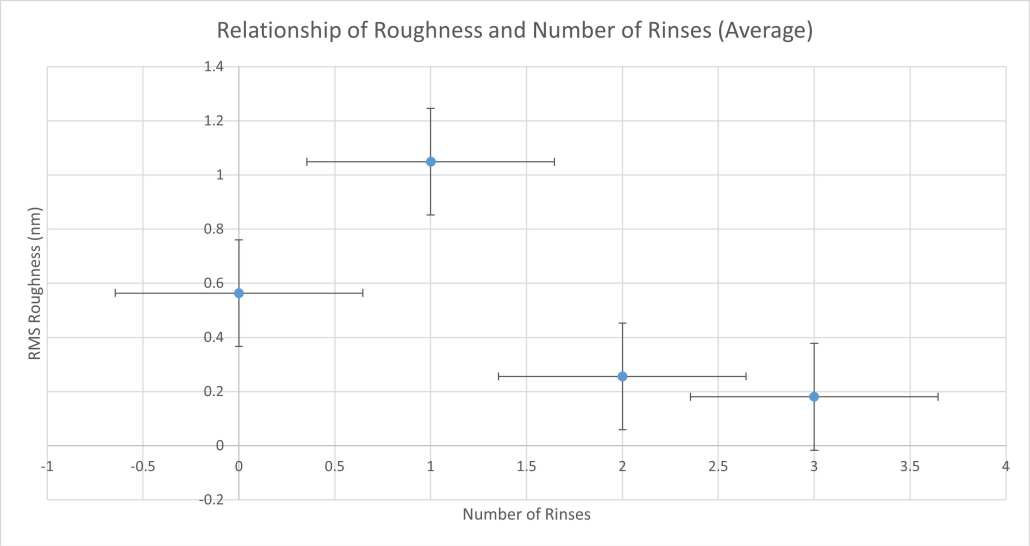

Figure 5.9: Graph showing the relation between the number of rinses and surface roughness

High roughness values were found when no rinsing or rinsing once was conducted. The values are high due to the high salt content attached to the surface that goes away as the rinsing volume increases. Unexpectedly, no rinsing seems to have a much smaller roughness value compared to the rinsing once experiment, which in theory, should drop because of the decrease in the unattached triangles and the salt concentration attached to the surface. On the other hand, origami triangles are more structurally stable when rinsed once compared to the no rinsing case. Furthermore, there is a smoother surface in samples which were rinsed $2-3$ times, reaching a value of about 0.2 nm.

These experiments validate the protocols followed in literature, that $2-3$ times of rinsing allows a greater degree of origami attachment and lower salt content on mica.

5.1.3 Measurement of Triangle Sides on Cleaved Mica

The length of the triangle sides was extracted from an average of 6 triangles for each rinsing case (except the no rinsing case, where only 2 were found). A zoomed-in image of each rinsing case is shown in Figure 5.10 (rinsing 3 times was shown in the previous section in Figure 5.2). In Figure 5.10c, some loops of ssDNA are visible on the right side of the image, which were probably dsDNA strands that unfolded during deposition. There is a possibility of origami unfolding when deposited in regions with insufficient magnesium ions. The lack of adequate positive charge creates a repulsive electrostatic force between the adjoining helices, that unfolds the DNA origami structure [69]. The results are summarized in the table below (Table 5.2).

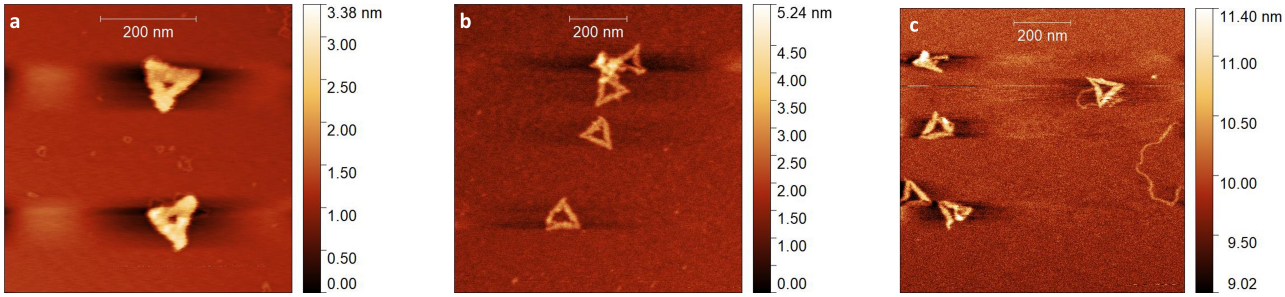

Figure 5.10: This Figure shows measurements of origami triangles after a) no rinsing, b) rinsing once and c) twice with 1000 mL.

The average length of the triangle's sides is significantly smaller than the value found for the 3-rinsing experiment. However, this is mainly accounted for by the different AFMs used for the topological measurements. The dimensions of the triangle sides greatly vary between the no rinsing and rinsing cases. There is a difference of 12 nm between the no rinsing case and the rinsing once experiment. The high variation in triangle lengths might be due to the increased magnesium ions on the substrate. As magnesium ions are attracted to the DNA strands inside the cavity, the nanostructure's dimensions reduce. On the other hand, there is a much lower difference between the triangles found when the sample was rinsed once and rinsed twice (about 3 nm). Another noticeable effect of changing the rinsing volume for each case is the increased thickness as the rinsing volume decreases. An increase of 10 nm in the thickness of the triangle side when no rinsing was performed compared to cases where rinsing by 1000 $/muL$ was applied. The thickness of the triangle sides further decreases to 29 nm when the rinsing volume increases to 2000 μL. Another thing to note is the high standard deviation found in the dimensions and the thickness of the triangles.

This experiment conveys the effect of magnesium ions on the triangular sides. As the buffer is not washed away, the remaining magnesium ions attach to the DNA strands, bringing them closer together, thus reducing the dimensions of the triangle. In addition, the thickness of the triangles' sides could indicate the number of positive ions that attach to the DNA origami nanostructures. As the positive ions attach to the nanoarchitectures, the side's thickness increase significantly. In this case, there is a difference of 13 nm between the optimal rinsing protocol and the no rinsing case.

Rinses	**Average Length (nm)**	**Thickness of Side (nm)**
0	105.6 ± 8.2	42.4 ± 3.5
1	117.6 ± 8.1	32.7 ± 5.8
2	114.2 ± 8.2	29.3 ± 9.3

Table 5.2: Table comparing various parameters of the origami triangle in effect of different rinsing conditions

Images of triangles in which cavities were not visible were captured for the case of rinsing twice and no rinsing was collected. In the case of rinsing twice, the dimensions of the triangle are not affected significantly (Average Side = 113.0 ± 2.1 nm), therefore the fact that the tip does not reach the bottom of the mica is more of the inability of the tip to interact with the surface at that particular location rather than magnesium interacting with the DNA origami. On the other hand, in the case of no rinsing, a lot more salt is present on the surface, and triangle sides shrink by about 20 nm (Average Side = 98.2 ± 2.7 nm). As mentioned previously, the reason for the deformation might be the interaction of magnesium ions with DNA strands. The height profiles for all the rinsing cases were all between the values of 1.5 and 2.2 nm.

Taking everything into account, images of triangles with cavities should only be considered when comparing dimensions with results from other substrates since magnesium might shrink the length of the triangle sides.

5.2 Deposition of buffer on pristine graphite

Before depositing DNA origami to graphite supports, control experiments were conducted to understand further the interaction between DNA/buffer solution and the 2 surfaces (mica, graphite). First, TAE/Mg^{2+} buffer was transferred onto both graphite and mica substrates. In this experiment, some optical images of graphite flakes on mica were captured (Figure 5.11).

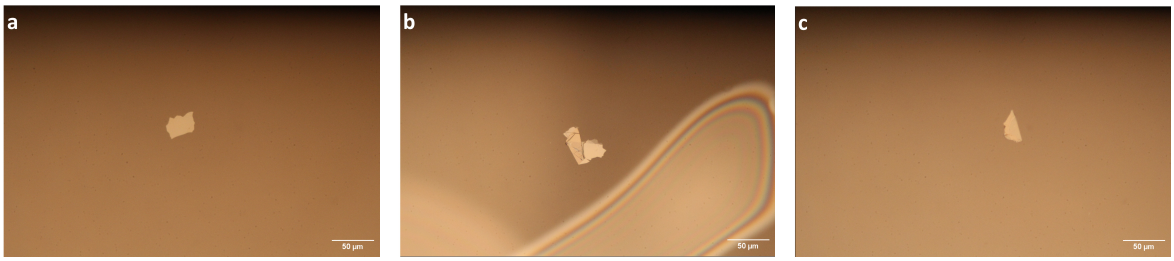

Figure 5.11: Optical Images of graphite flakes on mica. Magnification = 60×

Uniform colour is present on 2 out of the 3 graphite flakes, implying a similarity in the number of layers. In the other case (Figure 5.11b), two different colours appear, with the left part having a darker yellow colour than the one on the right. A darker yellow colour conveys a higher thickness i.e. higher number of graphene layers. Furthermore, some cracks appear on the thicker part of the flake, probably because transferring thicker graphite parts increases the surface tension during transfer to mica. Also, the flake might have inherited these cracks from before during the transfer of graphite parts found in the scotch tape to the PDMS stamp (Section 4.2). Figure 5.12 conveys the height profiles of the graphite flakes utilized for this experiment. In addition to the height profiles, also the additional graphite part on right side of Figure 5.13a was extracted (Figure 5.12b).

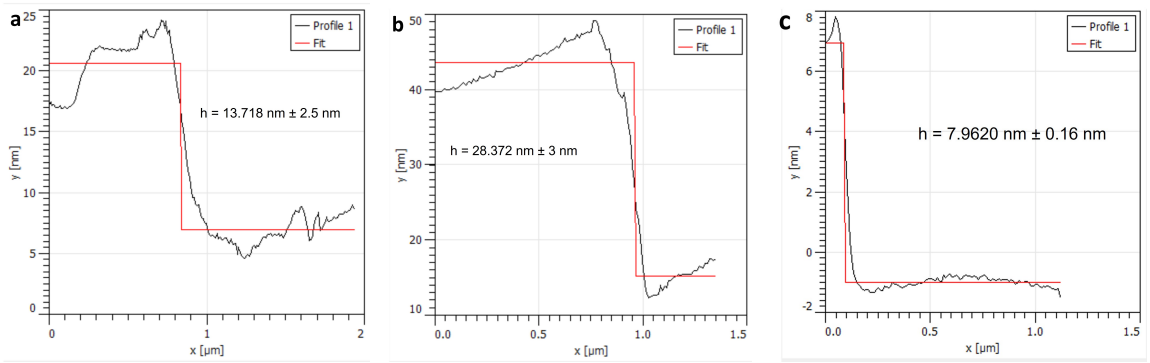

Figure 5.12: Height profiles of the flakes found in Figure 5.13a (a) and 5.13b (b). Figure c) is the height profile of the graphite part on the center right side of Figure 5.13a.

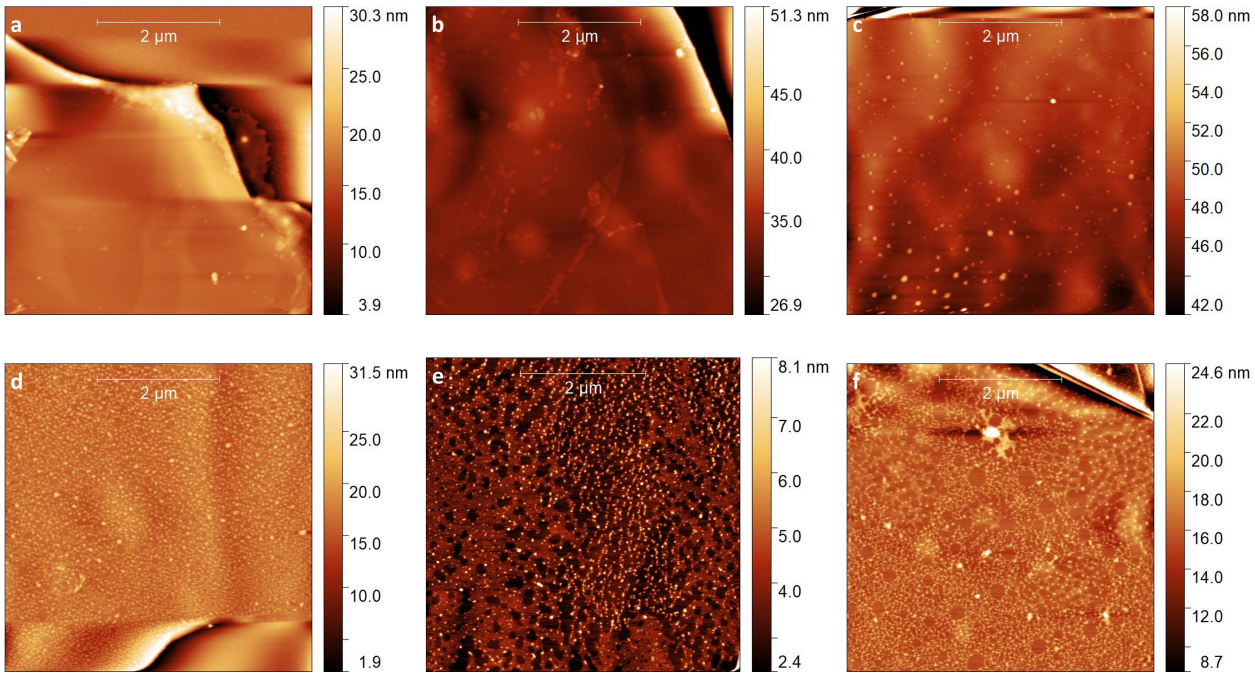

Figure 5.13: AFM measurements of pristine graphene before (top) and after (bottom) deposition of TAE/Mg^{2+} buffer

Images before and after the deposition were taken (Figure 5.13). Graphite was relatively flat with the RMS roughness measurements (1.39-1.65 nm). Furthermore, before deposition, some elevated structures mark the presence of a difference in the number of layers in the graphite region measured (like the right side of Figure 5.13a) and in some cases, the residue left from the PDMS transfer (bottom part of Figure 5.13c). However, the surface of graphite changes significantly after the deposition of the buffer on the surface. In all images, many dotted structures remained on the surface. The most likely origin of the dotted structures is the buffer residue that remained on the surface due to the hydrophobic nature of graphite upon interaction with the atmosphere [70]. The dots do not form networks due to the lack of negatively charged particles to connect them.

5.3 Deposition of DNA origami on mica after transfer from empty PDMS stamp

A question that comes into mind is whether the properties of mica change after the transfer methods are applied. Cleaved mica might lose its negative charge after interaction with air, as mica was left outside the desiccator during the graphene transfer (maximum time would be around 15 minutes). As previously mentioned in the 2D Materials Section (see Section 2.2.2), mica strongly reacts with water, carbon dioxide, and hydrocarbons [37]. Furthermore, PDMS residue might have glued to mica, resulting in a reduction in the attraction between DNA origami and mica. To test it, a freshly cleaved mica substrate underwent a PDMS transfer procedure. However, this time the PDMS stamp was empty without any graphite flakes. This experiment will help us understand if the properties of mica are changed significantly to reduce the adhesion of DNA origami to the substrate after the PDMS transfer method. Measurements before and after the deposition of DNA origami were taken (Figure 5.14).

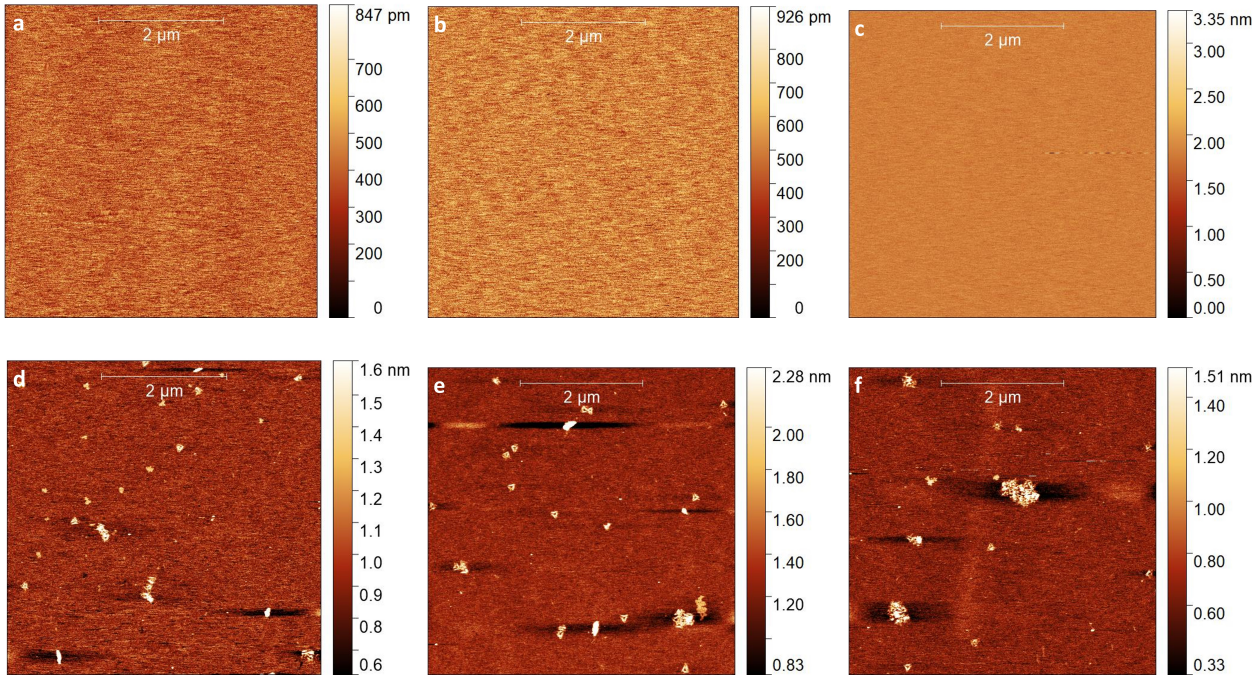

Figure 5.14: AFM images of mica surfaces before (top images) and after (bottom images) deposition of origami. The PDMS transfer method was used on mica, however the stamp was empty.

The roughness of the mica substrate does not seem to be affected during PDMS transfer. The corresponding RMS roughness values of the surfaces were all lower than 100 pm ($82.1 - 86.5pm$). Also, no dirt is visible on the surface, implying that no PDMS residue adheres to mica. These observations indicate that the PDMS stamp has no effect on mica's ultrathin surface. However, AFM measurements have found (Figures 5.14d-5.14f) that the origami nanoarchitectures decrease in quantity, appear in aggregates, and their sides detach from one another. The difference in behaviour is attributed to the potential loss of the negative charge of the mica surface. The exposure of cleaved mica to the atmosphere and the PDMS stamp for a prolonged time results in a loss of negative charge in specific locations. As previously noticed in previous experiments, the nanostructures unfolded because of the weaker interaction of negatively charged mica and positively charged magnesium ions. Figure 5.15 shows some examples of DNA origami triangles on PDMS-stamped mica. The magnitude of the triangle sides was similar to the bare mica case (116.6 ± 12.0 nm), despite the slight increase in the range of values.

Although the ultrathin nature of mica is not affected by the PDMS stamping method, there is a limited adhesion of origami on mica, probably caused by the loss of the negative charge of mica due to exposure to air and the PDMS stamp. On the other hand, triangles retain their original dimensions, having an average very close to the freshly cleaved mica case.

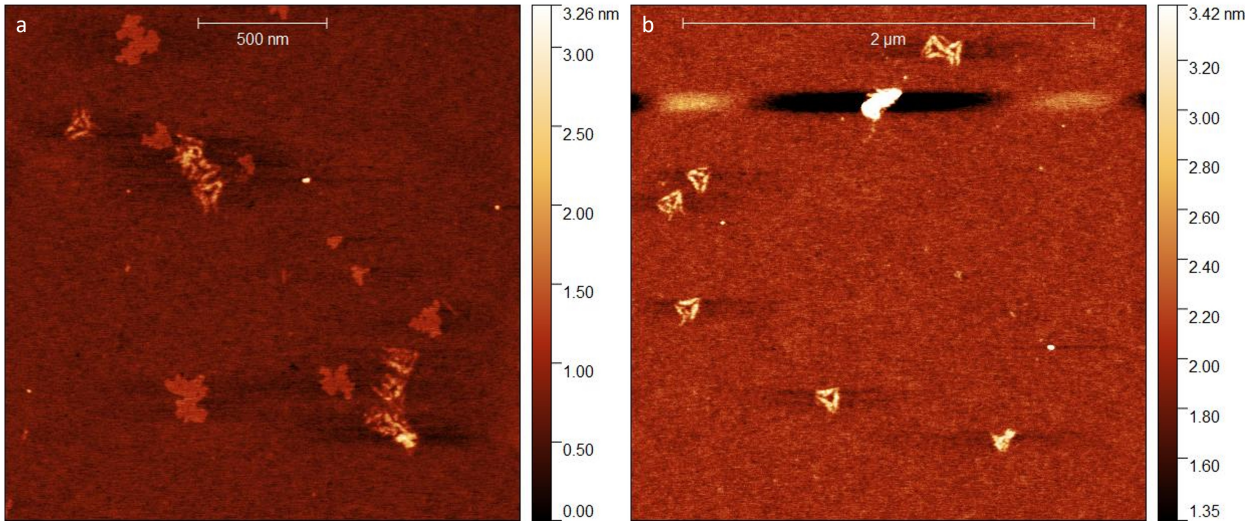

Figure 5.15: A closer look into the shape of DNA origami triangles on mica surfaces that were spontaneously in contact with an empty PDMS stamp

5.4 Characterization of DNA Origami on Graphite

After imaging DNA origami triangles on mica, measurements on bulk graphene substrates were performed. Bulk graphene was transferred into mica substrates using the direct transfer method and the PDMS stamping method (outlined in Section 4.2). The first experiment included DNA origami with a concentration of 2 nM and an incubation time of 5 minutes. The increase in the incubation time was because of the rougher surface of graphite in relation to mica which could potentially lead to a higher time for the nanostructures to diffuse and adsorb. Taking a look at the 3D topography of both substrates (Figure 5.17), there is a clear distinction of the much greater roughness on graphite samples when compared to mica.

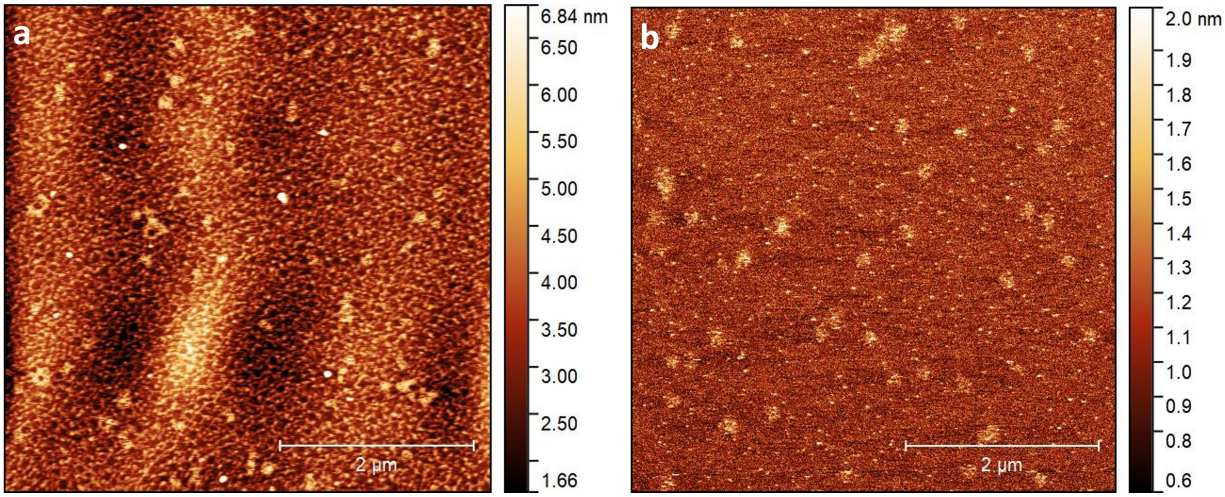

Figure 5.16: AFM measurements of a) graphene and b) mica after deposition of 2 nM DNA origami

A significant amount of buffer is present on both substrates (mica and graphite). Little structures join together that could possible be aggregates of DNA origami nanostructures that go on top of each other. On the bulk graphene substrate, there are also some networks visible. The formation of

networks could be explained by the reaction of denatured DNA strands and magnesium ions. These networks have a height of about $2-3$ nm, slightly higher than the height profiles previously seen. The graphite flakes in this experiment were transferred using the direct transfer method. On mica, also the nanostructures are not visible, with the substrate containing buffer residue. On both substrates, no triangular structures are visible.

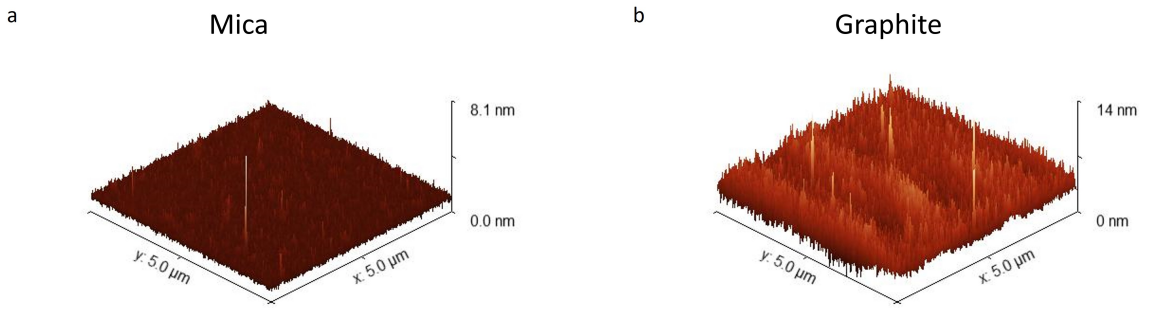

Figure 5.17: 3D Topography of a) mica and b) graphite after deposition of 2 nM DNA origami triangles

As concluded in [70], graphite becomes hydrophobic after a few minutes of exposure to air [70], whereas cleaved mica is hydrophilic. Due to the hydrophobic nature of graphite, the solution stays longer on the surface, resulting in the buffer sticking to both substrates. The quantity of DNA origami triangles (about 34 for both substrates) is reduced compared to previous cases, consistent with previous results [71], that noticed the ability of water exposure to reduce the density of DNA origami nanostructures. On graphite, DNA origami nanostructures lose their original structure, while a network forms in the background due to DNA and Mg^{2+} reacting together. As a reminder, on graphite substrates, DNA adheres covalently via $\pi - \pi$ bonds.

To validate the results, this experiment was repeated with similar conditions and transfer methods. The major results are outlined in Figure 5.18.

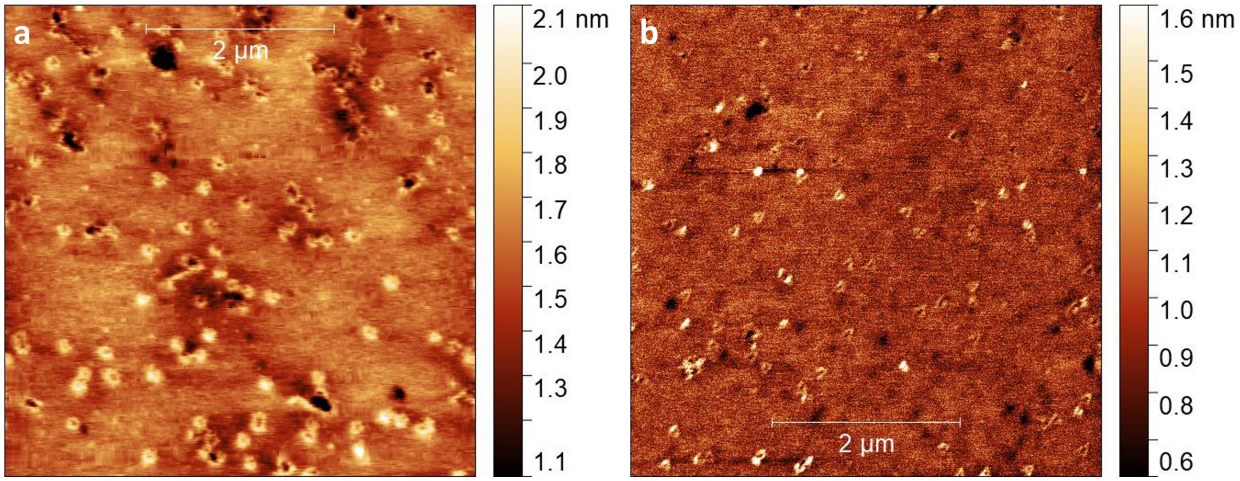

Figure 5.18: AFM images of DNA origami on direct transferred graphite (a) and mica (b)

Similar results are seen in this sample as well, with potential DNA origami structures found on mica (Figure 5.18b). However, the roughness of the surface and buffer residues on both substrates do not enable a detailed characterization of DNA origami. An attempt to get a closer image of the origami

triangles is presented in Figure 5.19.

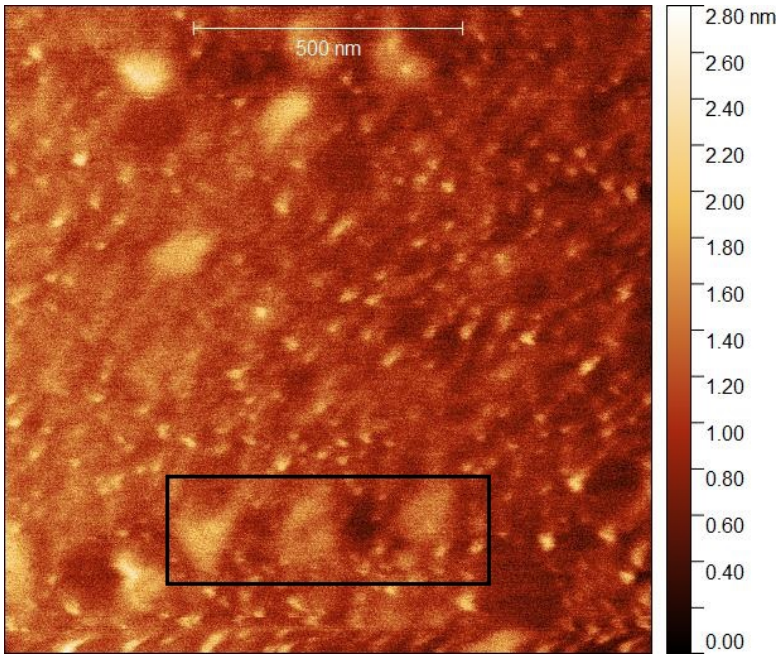

Figure 5.19: Attempt to image in more detail the DNA origami nanostructures on graphite substrates

At the bottom of the image (selected by a square), you can see 3 triangles that appear slightly distorted. Although the structures appear triangular, the background does not allow an accurate characterization of the triangles.

For the DNA origami nanostructures' characterization to be more accurate, a drying and rinsing method that would allow the complete removal of the buffer is required. The measurements were captured close to the edge, as most graphite flakes were deposited closer to the sides because of the direct transfer method. According to the results of previous experiments (Figure 5.5), close to the edge, a substantial increase in salt content compared to the centre was observed. For the following experiments, the PDMS stamping method deposited graphite flakes close to the centre of the mica. A small PDMS stamp transferred a large concentration of graphite flakes to the centre of the mica.

After using the PDMS stamping method to transfer bulk graphene flakes on mica, the same conditions were used (5-minute incubation, concentration of DNA origami = 2 nM). The 3mE AFM and the SCANASYST-AIR HR cantilever were utilized for this experiment. The cantilever changed because of the unavailability of the same tip at the location of this new AFM. On the other hand, the AFM controller remained the same (JPK Nanowizard XP 4), only now the camera was on top of the sample instead of below.

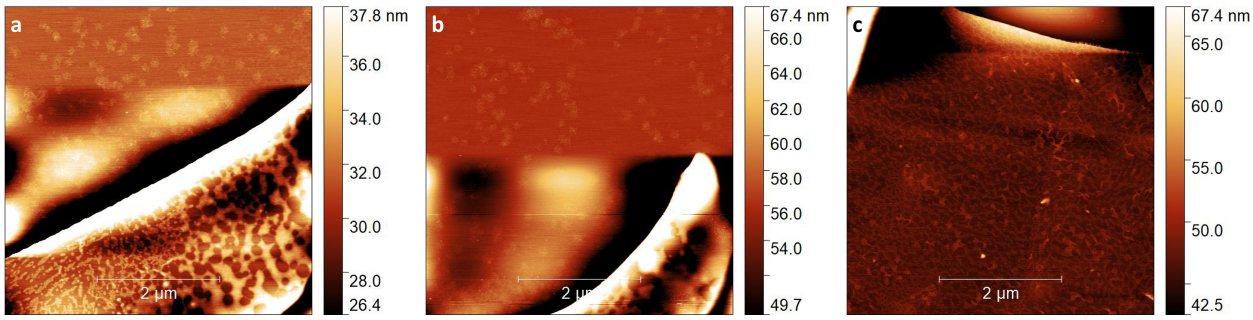

Figure 5.20: AFM images of DNA origami on the graphene/mica boundary

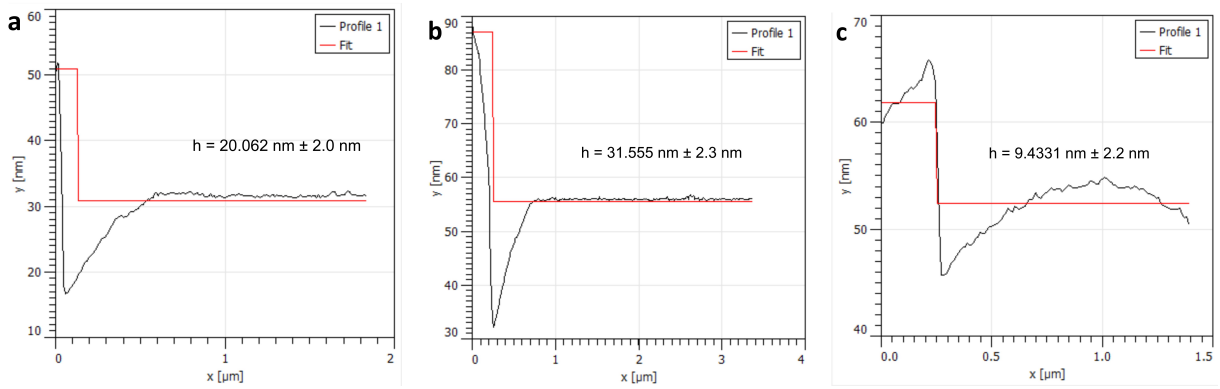

Figure 5.21: Height profiles of the flakes seen in Figure 5.20

Measurements close to the boundary of the mica-graphite were taken. This would enable a better comparison of the differences in the interaction of the 2 substrates. DNA origami structures accumulate close to the mica-graphite boundary because of the high magnesium concentration present in the mica-graphite boundary. A higher salt accumulation was induced because of the covalent bonding of graphite-DNA interaction that results in excess magnesium ions flowing freely on the surface. Another potential cause is the hydrophobic nature of graphite that forms blobs of the solution close to the boundaries. On the graphite substrate, there is a formation of DNA/Mg^{2+} networks that make it difficult to assess the effects of graphite on the nanostructure's dimensions. The height profiles of the graphite flakes were extracted and are shown in Figure 5.21. Smaller region measurements were conducted to characterize the structural properties of DNA origami nanoactuators. In Figure 5.20b, triangular structures with a higher height profile than the rest of the surface. The details of the origami nanostructures found on graphite surfaces will be outlined later (Section 5.4.2). An important thing to notice is that the heights of the triangular structures found on graphite are not uniform. The height difference is in the range of 1.0-1.5 nm. An increase of about 0.5-2.0 nm compared to the height profiles of the Rutherford triangles on mica substrates.

Because of the increased hydrophobicity of the surface, the drying procedure was revised, and higher power in the nitrogen gun was used.

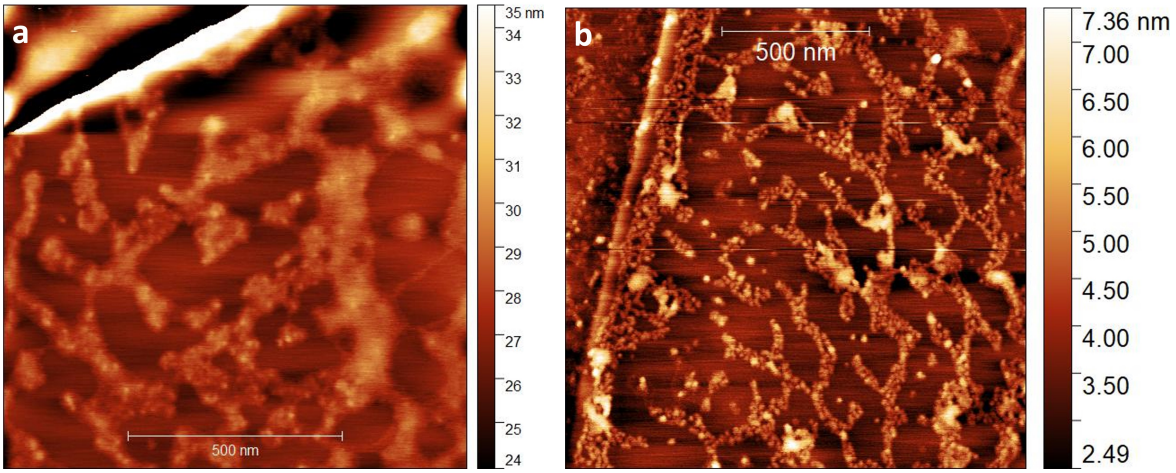

Figure 5.22: Zoomed images of DNA origami nanostructures on graphite substrates

5.4.1 Different Incubation Times

The origami accumulation close to the graphite-mica boundary also posed the question of how quickly the nanostructures would move towards the boundary. Therefore, experiments with increased incubation time (about 20 minutes) and decreased incubation time (1 min) were carried out.

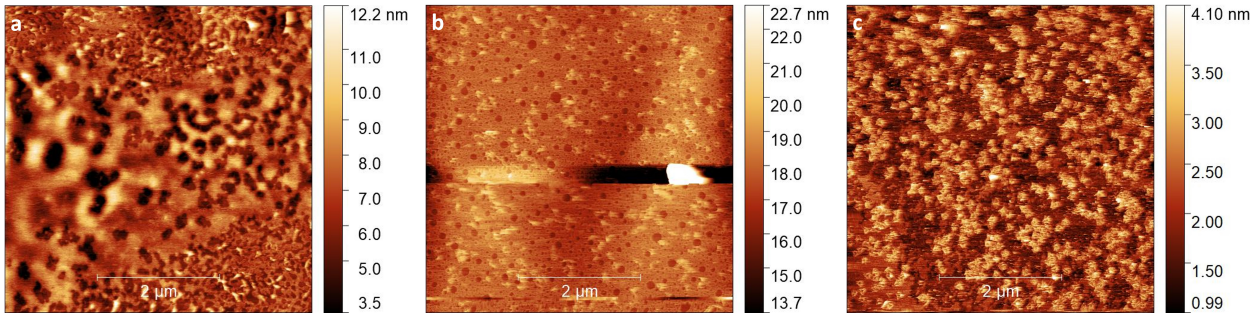

Figure 5.23: AFM measurements of graphite (a-b) and mica surfaces (c-d) after deposition of DNA origami and incubation of around 20 minutes

For 20 minutes incubation, there was an increased height profile for the networks (Figure 5.23a) because of the aggregates formed as the solution evaporated on the surface. In addition, the Rutherford triangles gather around the graphite-mica boundary more than the accumulation seen for the 5 min case (Figure 5.20). In Figure 5.23c, the DNA origami of the Rutherford triangles form aggregates, and there is difficulty in distinguishing individual DNA origami nanostructures. In Figure 5.23a, a cloud of buffer covers the substrate and does not allow the tip to reach the nanostructures. As the incubation time increased from 5 to 20 minutes, the number of networks and aggregates raised. On mica, the DNA origami nanostructures accumulate close to the graphite boundary, where most of the salt is dried due to graphite's hydrophobic nature.

Due to the abundant biomolecules present, the tip had 2 or more resonance frequencies (similar frequency value) on the frequency sweep measurement (calibration), and the laser intensity dropped after a few measurements, implying that a biomolecule might be attached. An important observation is the increased deformation of the triangles on mica. A possible explanation for this behaviour is the difference in the magnesium distribution in the mica/graphite interface compared to bare mica.

The hydrophilic nature of mica helps to achieve a better charge uniformity, whereas, on graphite (hydrophobic), the liquid might concentrate on specific areas. Also, the nanostructures might lose some of their structural properties due to the reduced negative nature of mica, as noticed in Figure 5.14.

The results suggest that a lower incubation time should be used to reduce the number of networks and aggregates created. Using a lower incubation time could reduce the possibility of aggregates and the gathering of origami nanostructures close to the mica/graphite boundary. Measurements before depositing DNA origami were captured (Figure 5.24). The measurements give an idea of the roughness and the amount of polymer residue left from the transfer.

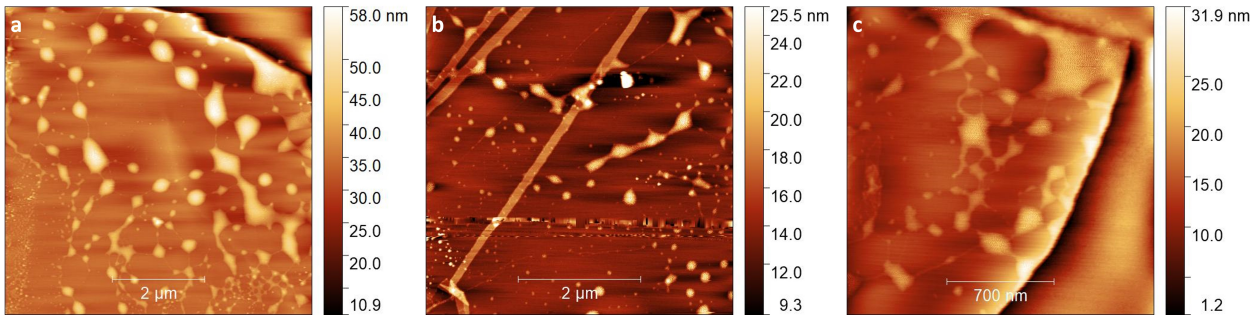

Figure 5.24: AFM measurements of graphite deposited on Mica before DNA origami was deposited

Polymer residue was more than expected because of the prolonged exposure of graphite to atmospheric conditions (2 hours). Graphite interacted with the environment and resulted in contamination and a high roughness value (average RMS roughness: 2.85 nm). After DNA origami deposition, the surface had an increased hydrophobic character than the graphite stored in the desiccator. In all cases, except this one, the samples were stored in the desiccator and were taken out only when measurements were performed. In addition, height measurements for Figures 5.24a and 5.24c were extracted and are shown on Figure 5.25.

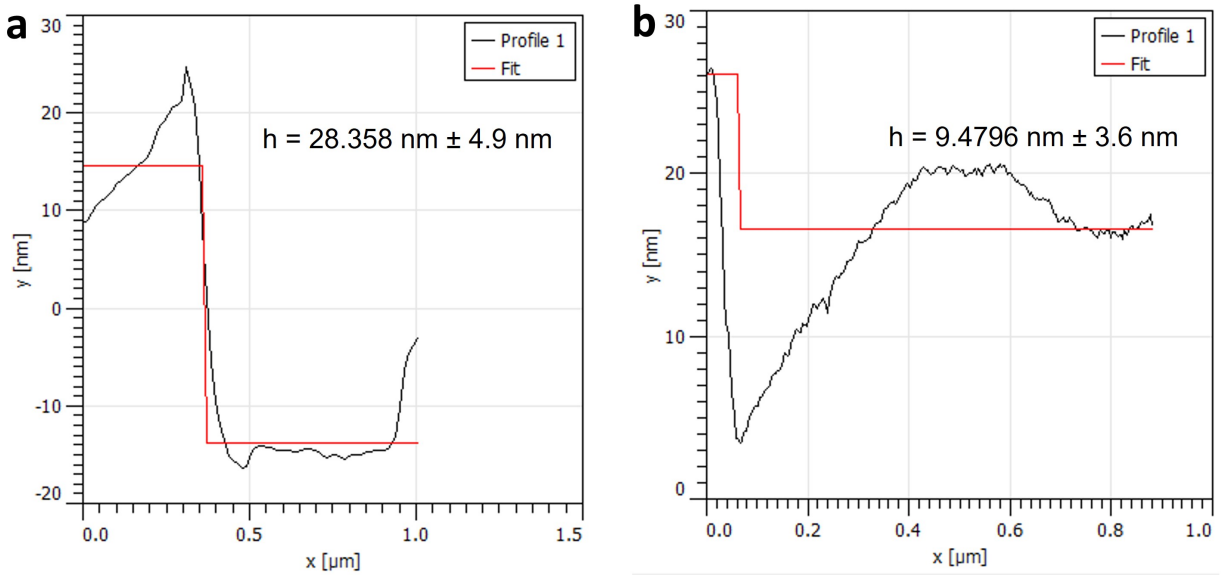

Figure 5.25: Height profiles of the graphene flakes imaged on Figures 5.24a and 5.24c.

After depositing DNA origami nanostructures, no networks were formed, on the other hand, dots of buffer residue remained on the surface. The DNA origami nanostructures are more visible than in the previous cases. On mica, the DNA origami nanostructures are more spread out and retain their shape, close to the results of freshly cleaved mica.

Reducing the incubation time to 1 minute decreased the interaction time of graphite and DNA origami structures, and as a result, fewer networks formed, allowing the characterization of DNA origami nanostructures. Therefore, the 1-minute incubation enables the optimal conditions for the characterization of individual DNA origami nanostructures because of the reduced formation of networks and aggregates.

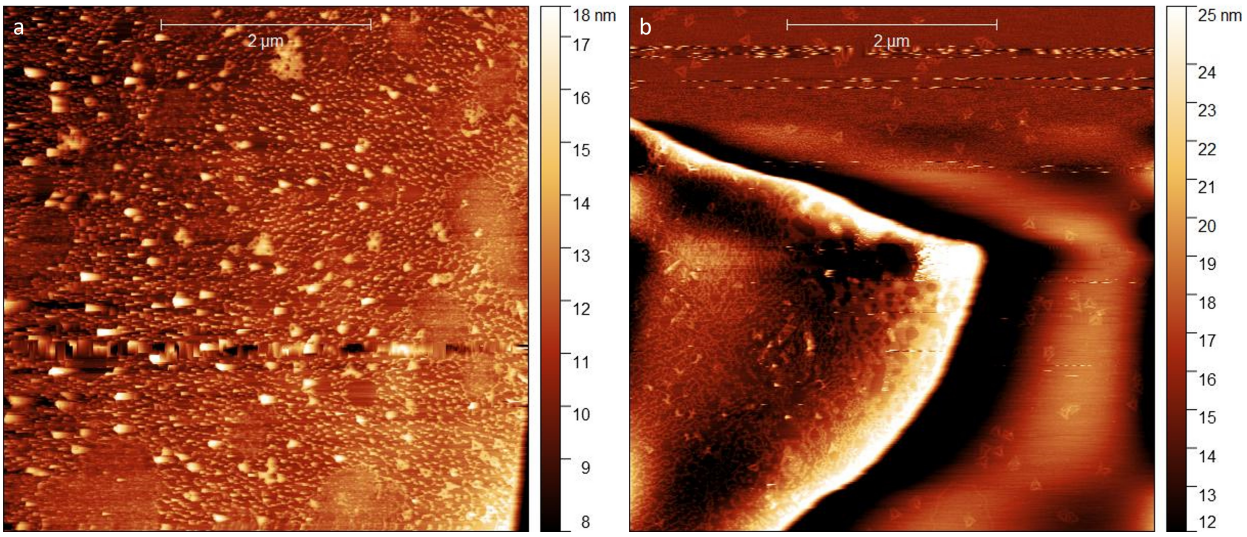

Figure 5.26: AFM measurements taken of a) graphene and b) mica/graphene boundary after deposition of 2 nM DNA origami

5.4.2 Characterization of DNA origami triangles on graphite

Although DNA origami/Mg^{2+} networks covered most of the bulk graphene substrates, a few images of DNA origami triangles were captured using AFM measurements of small graphite regions. In most cases, the incubation time of DNA origami on graphite substrate was 1 minute since increasing the incubation time resulted in a higher number of aggregates and DNA/Mg^{2+} networks.

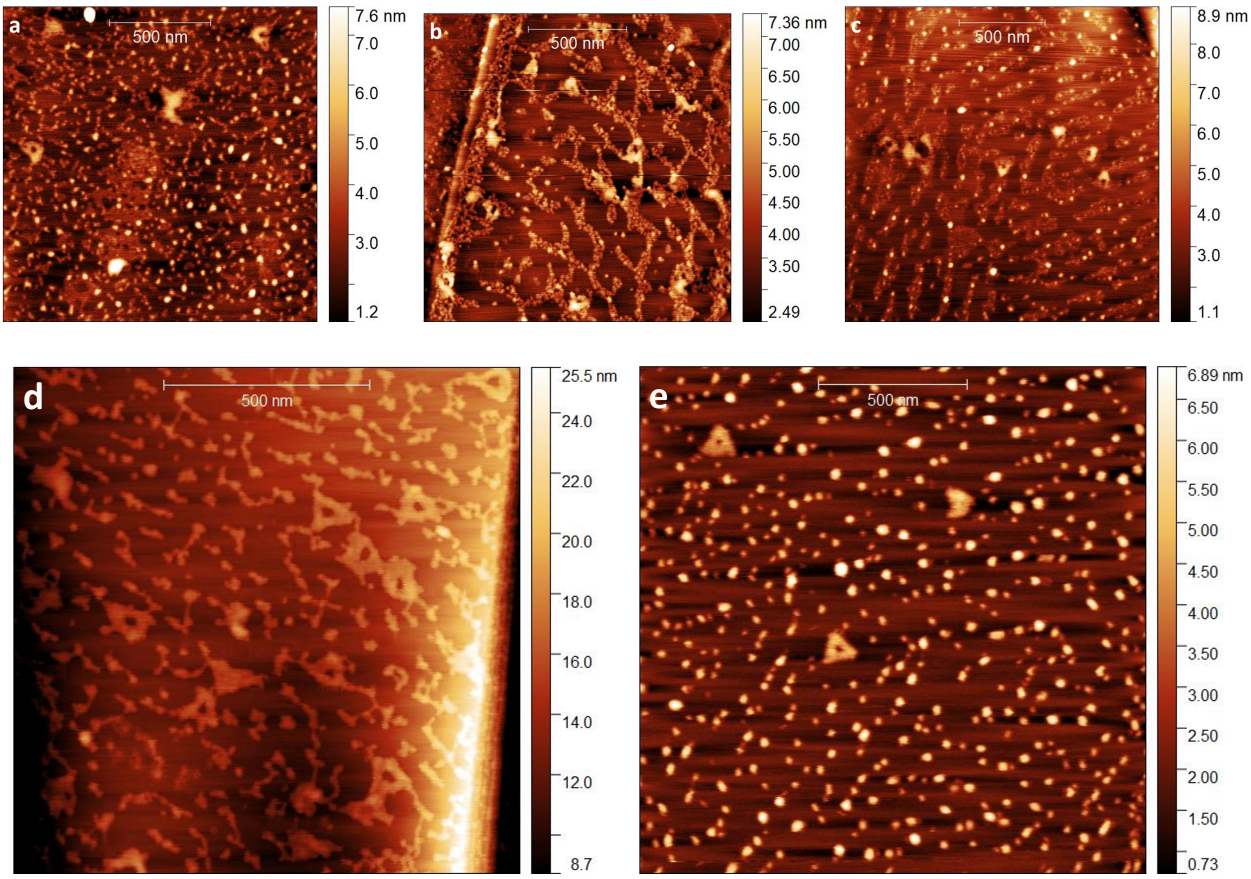

Figure 5.27: AFM Snapshots of DNA origami triangles on bulk graphene structures. For all the experiments, the incubation time was 1 minute except in Figure b) where the incubation time was equal to 5 minutes.

As mentioned earlier, the triangles have non-uniform height profiles AND slightly higher heights than the triangles found on mica. Possible causes of this behaviour are the attachment of denatured ssDNA strands on the nanostructures and the increased surface roughness of graphite to mica. Height profiles, on the other hand, cannot verify the nature of the DNA origami since they are easily affected by the tip contact with the sample and its usage time. Figures a-d were measured using the 3mE AFM with the cantilever SCANASYST-AIR, whereas for the rest, the JPK AFM with a FESP-V2 cantilever was utilized. Table 5.3 summarizes the length of each triangle's side (from the lowest to highest) and the average of all sides on different substrates. For an accurate comparison, the measurements from each AFM were separated.

AFM	**Incubation**	**Substrate**	**Dimension 1 (nm)**	**Dimension 2 (nm)**	**Dimension 3 (nm)**	**Average (nm)**
3mE	1 minute	Graphite	89.9	101.3	107.2	99.5 ± 13.1
BN	1 minute	Graphite	96.4	107.2	111.9	105.2 ± 11.4
BN	2 minutes	Mica	108.5	116.1	123.0	115.9 ± 8.3

Table 5.3: Table assessing the change in the triangle side lengths as the incubation time and the substrate are varied

There is a noticeable difference in the average and range of length sizes between the DNA origami triangles on graphite and on mica. On graphite, the triangles contract into an average size of about

99.5 ± 13.1 nm on the 3mE AFM, and 105.2 ± 11.4 nm on the BN AFM, in contrast with mica where the average length was 115.9 ± 8.3. A possible cause of the difference is the assumed melting of the dsDNA into ssDNA, resulting in a reduction of the base length of the triangle sides. For the 5-minute incubation, only 3 triangles were found, therefore they were excluded from the comparison. The reason for the low number of Rutherford triangles is the increased number of DNA/Mg^{2+} networks and aggregates developed on graphite that covered or melted individual nanostructures, as incubation time increased. Figure 5.28 conveys the distribution of triangle sides measured on both substrates.

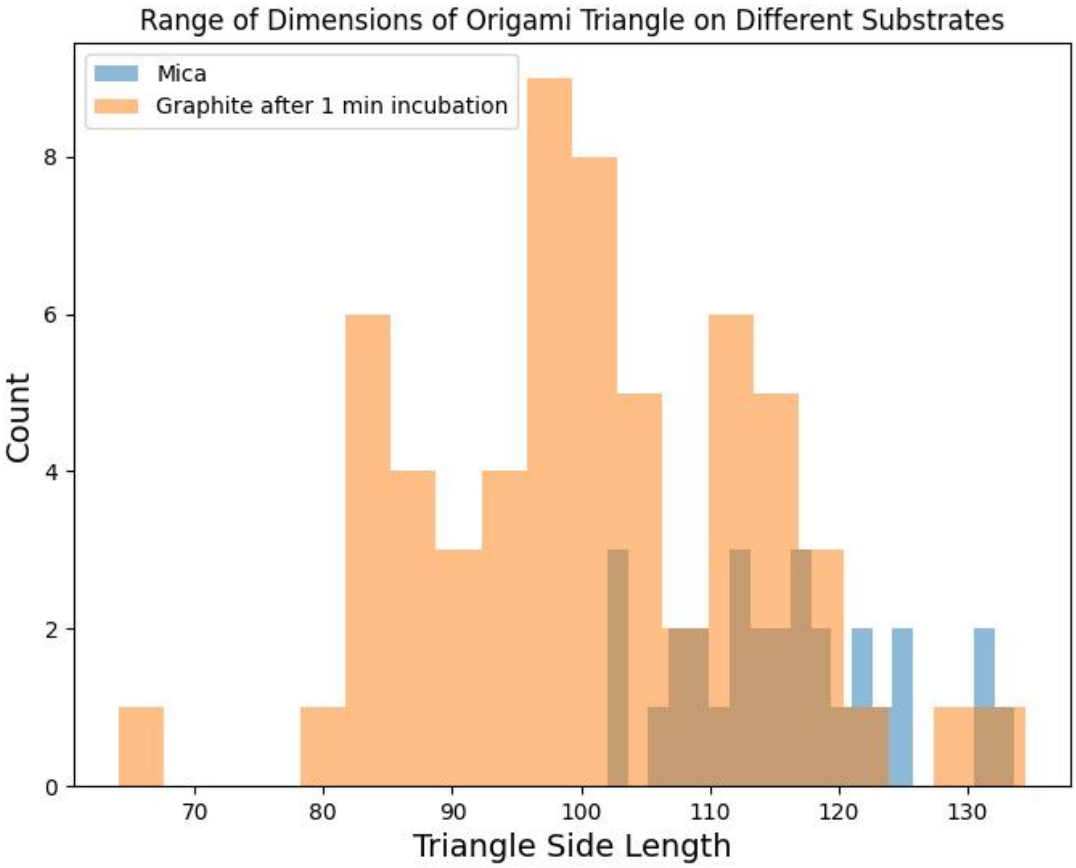

Figure 5.28: Histogram showing the magnitude of the triangle sides on both mica and graphite. On graphite, the incubation time was 1 minute, whereas for mica the incubation time was 2 minutes.

The histogram depicts a substantially greater range of values for the DNA origami nanostructures on graphite related to mica. The side lengths covered by DNA origami nanostructures on graphite were between 67-132 nm, whereas, for mica, it was 100-132 nm. As discussed earlier, the dehydration and absence of physiological conditions of DNA origami nanostructures gave a higher range than the values previously found in literature [72]. On the other hand, the effect of the $\pi - \pi$ bonding of graphite to DNA bases shortens the triangle sides due to the melting of dsDNA to ssDNA, broadening the range of side lengths found. Sometimes, on the other side, triangle sides retain their original dimensions. A potential reason is the decreased contact some DNA origami triangles have with graphite, which reduces the influence of $\pi - \pi$ bonding. Additionally, it might be that a single triangle side might react with graphite, while the other sides do not noticeably interact with graphite.

The change in the cantilever does not significantly affect the dimensions of the Rutherford triangles since both cantilevers measured a similar range of length values. The difference in the average found

for the 2 AFMs can be accounted for by the different number of triangles used for the calculation (3mE:14, BN: 5).

5.5 Functionalization of graphite with poly-L-lysine

Deposition of DNA origami nanostructures on bulk graphene showed an increasing number of aggregates and a reduced number of single DNA origami triangles visible on the surface compared to mica. In addition, the dimensions of the DNA origami triangles reduce significantly. The main reason is the denaturation of DNA origami due to $\pi - \pi$ interaction with graphene layers that might have led to the melting of dsDNA to ssDNA. Furthermore, because of the hydrophobic properties of graphite and the increased distribution of DNA origami, more magnesium ions attach to the surface and form networks of DNA/$Mg2+$. As discussed in the 2D Materials Section, different functionalizations provide graphite with a biocompatible environment. A frequently used functionalization was poly-L-lysine. Poly-L-lysine has abundant amino groups that interact with graphene due to the covalent amide group [73] (Figure 5.29 for its structure and how it binds to DNA origami). An Amide group has the structural formula $R - C = O - NH_2$ where R represents a molecule made of pure hydrocarbons or only hydrogen parts. After binding to graphene, plenty of NH_3^+ molecules can immobilize biomolecules like DNA origami.

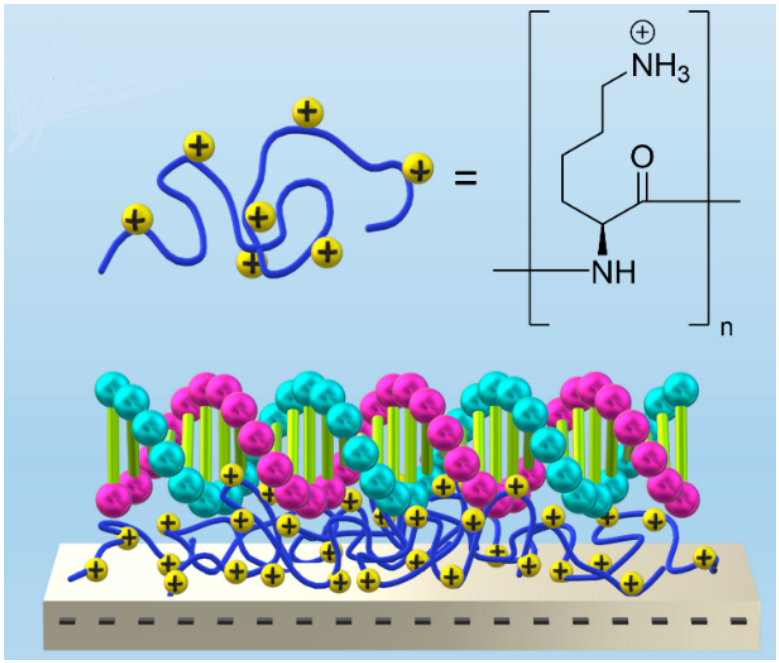

Figure 5.29: The structure of the monomer that gives rise to poly-L-lysine and the interaction between mica, poly-L-lysine and DNA origami. Taken from [22].

Researchers have used different concentrations and incubation times for poly-L-lysine for functionalizing bulk graphene or mica surfaces. Given the results of different articles, the protocols followed in [22] and [45] acted as tests to observe the effect of incubation time and concentration on mica/graphite surfaces after poly-L-lysine functionalization. In the first paper [22], the incubation time was 1 hour and the concentration used was relatively high (0.1 w/v %). The incubation time used was based on a study done by Jang, C. et al.[74], which found that maximum surface coverage of mica with poly-L-lysine occurs at around 1 hour. Unfortunately, the concentration in the lab was 10 times more diluted (0.01 w/v %) than the concentration utilized in the study. However, the experiment can demonstrate the surface coverage of poly-L-lysine on mica/graphite substrates. Figure 5.30 portrays the results for this protocol.

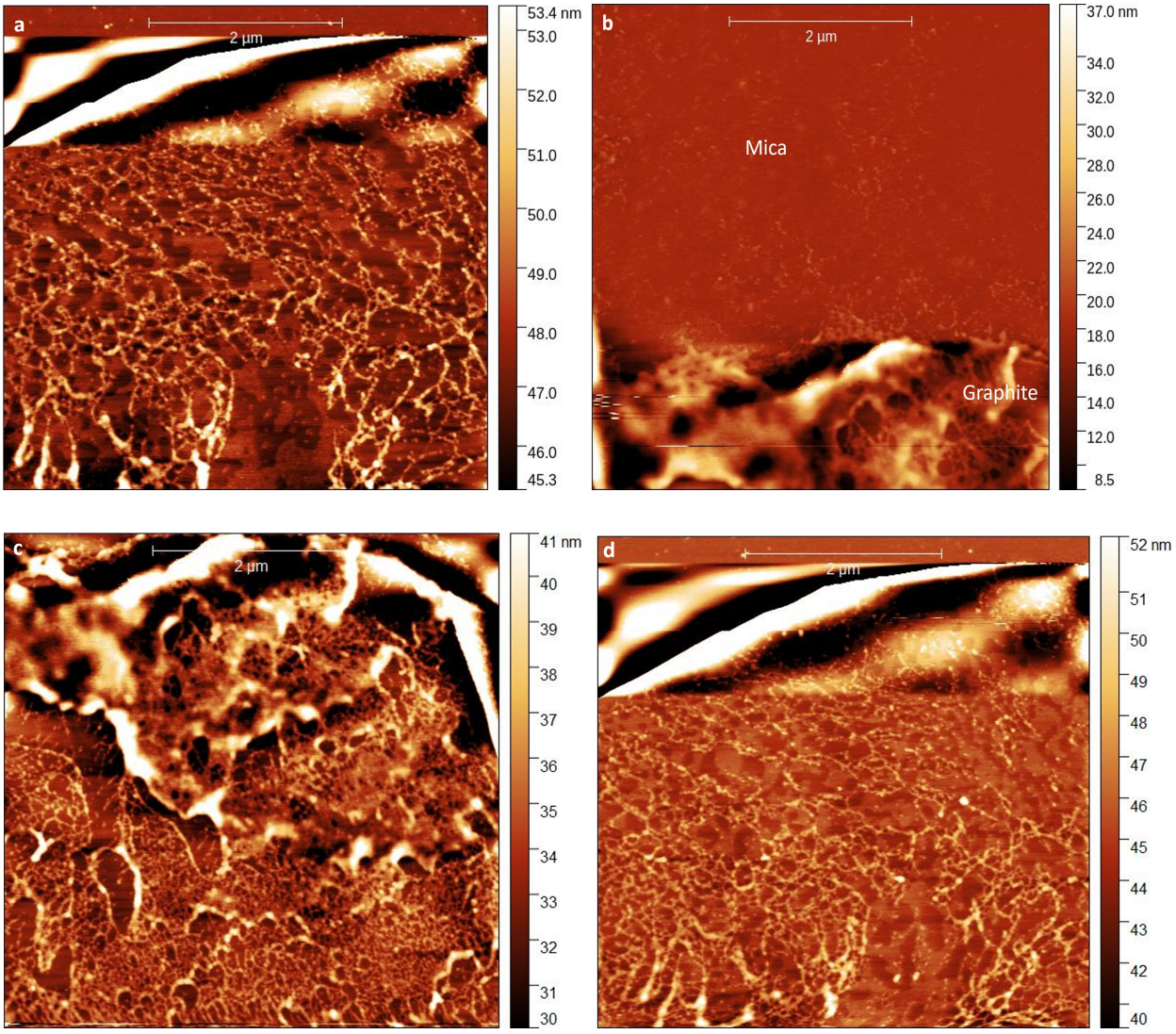

Figure 5.30: AFM measurements of a graphite substrate functionalized with poly-L-lysine followed by 1 hour incubation and drying, before (a-b) and after (c-d) DNA origami deposition

Similar networks as the one created by the Mg^{2+}/DNA on bare graphite surfaces are constructed. The similarity in behaviour can be accounted for by the $\pi - \pi$ bonding between graphene and DNA origami/poly-L-lysine biomolecules. The networks of poly-L-lysine and graphite are in the range of $1.3 - 5.0$ nm, as extracted from the height profiles at different scan locations. The accumulation of a high volume of poly-L-lysine might imply that the concentration of poly-L-lysine used is very high. The accumulation of poly-l-lysine has made it difficult for DNA origami to be found in the measurements after the deposition (Figures 5.30c and 5.30c). An important observation was the high hydrophobic character of the surface because of the presence of a poly-L-lysine coating on the graphite substrate. The volume used for poly-L-lysine was 30 μL, whereas for the DNA origami, a volume of 10 μL and a concentration of 2 nM was utilized.

Following the results of this experiment, another protocol utilized by Kaminska et al.[45] was followed. In this case, a much lower concentration (0.00005 w/v %) and a shorter incubation time were utilized (1 minute). This experiment aims to see the effect of the shorter incubation time and the diluted poly-L-lysine solution on reducing aggregates and networks formed on graphite substrates.

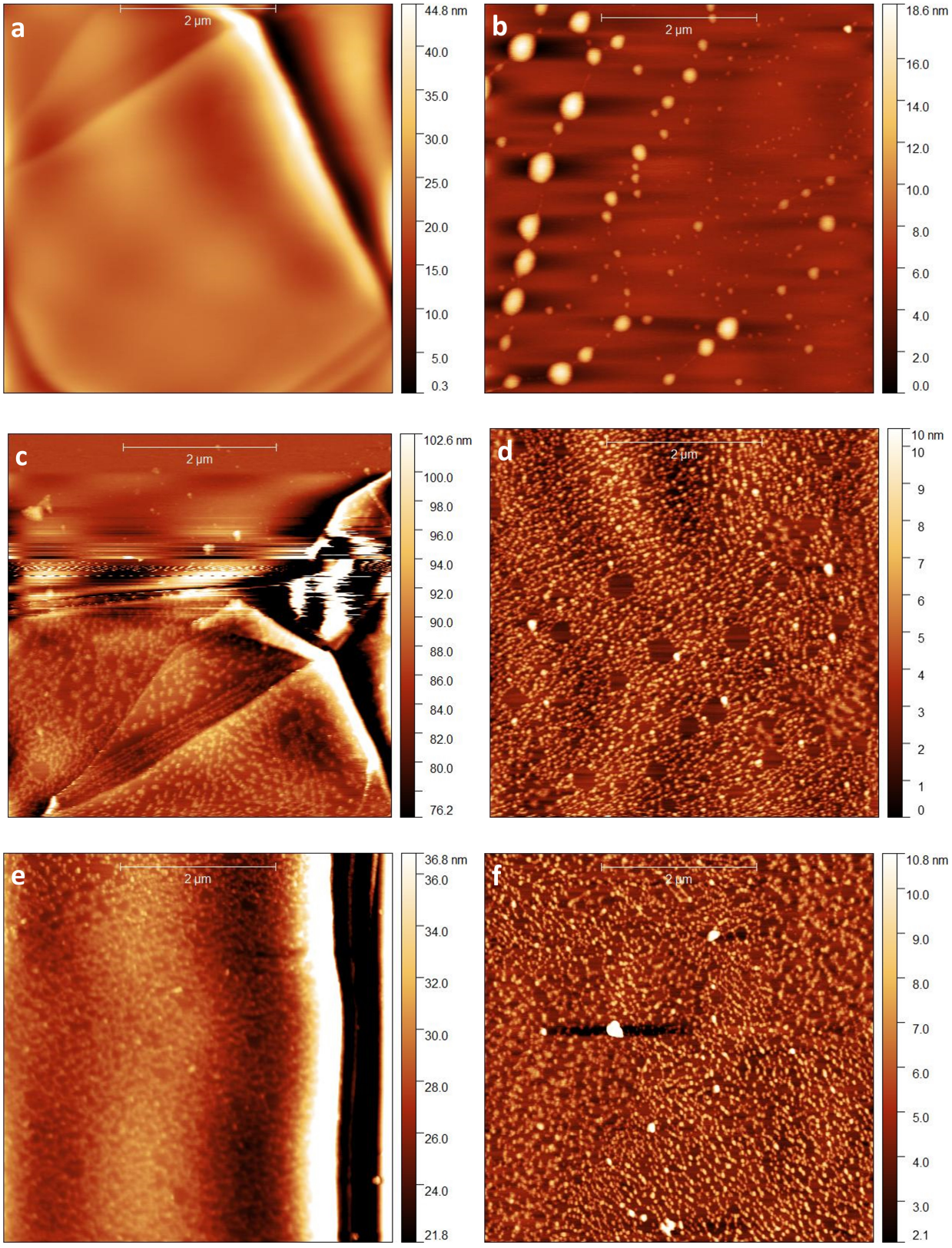

Figure 5.31: AFM measurements of a graphite substrate with no functionalization (a-b), poly-L-lysine functionalization (c-d) and after DNA origami deposition (e-f) of graphite substrates

Decreasing both the incubation time and the concentration of poly-L-lysine did not reduce the networks

created from the $\pi - \pi$ interaction of graphite with poly-L-lysine. The height of the coating was again in the range of $1 - 5$ nm. The surface hydrophobicity was not visible as in the previous experiment (see Figure 5.30), implying that inadequate poly-L-lysine adhered to the surface. The reasons for this behaviour are a low concentration and insufficient incubation time. The deposition of DNA origami does not cause a noticeable difference in the measurement.

Since 2 parameters changed compared to the previous experiment, a systematic study of incubation time or concentration would allow a better understanding of the interaction of graphite with poly-l-lysine.

Next, to examine the effect of incubation times on the substrate, 3 more experiments, with incubation times of 5, 30, and 60 minutes were performed. The concentration and volume used for the DNA origami remained the same, whereas the volume of poly-L-lysine decreased to 15 μL. The volume change occurred because 30 μL was more than enough to cover the whole surface (some of the solution spilt over). Figure 5.33 shows the results of the functionalization of the substrate with poly-L-lysine followed by 5 minutes of incubation. In addition, optical images of graphite flakes before the deposition of DNA origami were captured (Figure 5.32).

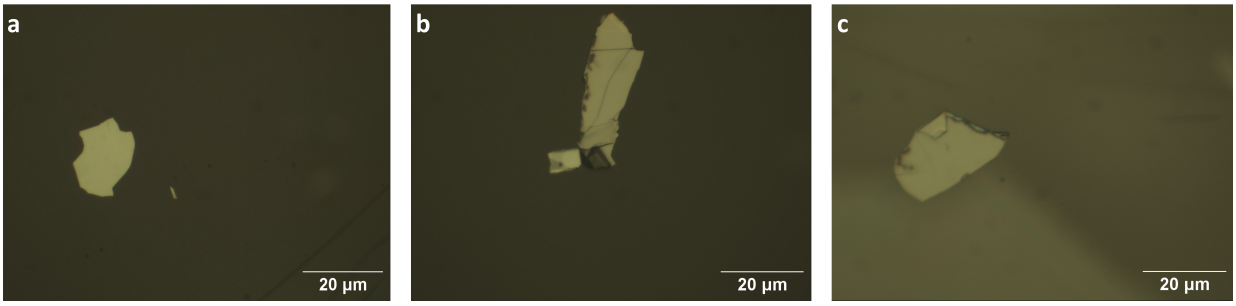

Figure 5.32: Optical Images of Graphite flakes on mica prior to DNA origami deposition. Magnification = 50×

This time, the flakes utilized for this experiment had some cracks and colour differences along their length, suggesting that different thicknesses of graphite are present in the sample. However, following the AFM measurements of the graphite substrates after functionalization with poly-L-lysine, the change in thickness in the small area where the scan takes place is negligible. The only unexpected part is the elevated line in the middle of Figure 5.33b, which caused due to cracks on the surface of the corresponding graphite flake.

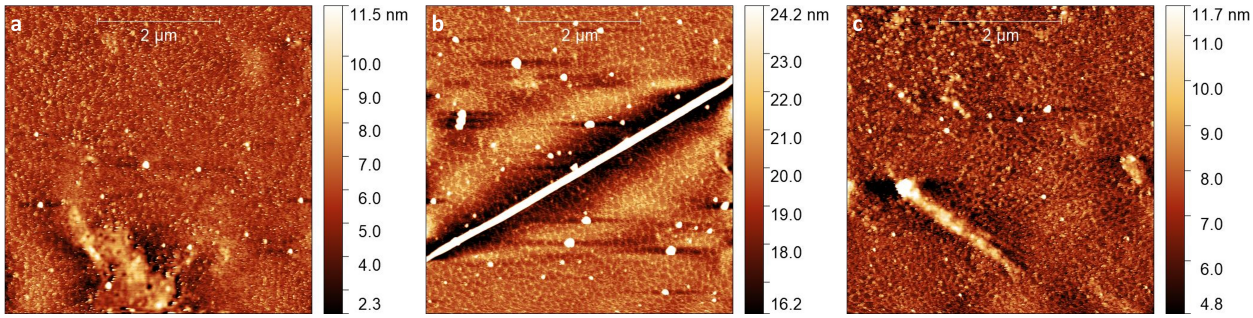

Figure 5.33: AFM images of graphite substrates after functionalization with PLL followed by 5 minutes incubation

As noticed before, the networking structures and aggregates of poly-L-lysine continue to exist in various regions. The height of the functionalizations agrees with previous measurements ($1 - 5$ nm) of lower and higher incubation times. Although there are many things on the surface, some DNA origami appears to stand out from the image. Close-up images of the nanostructures were captured (Figure 5.34).

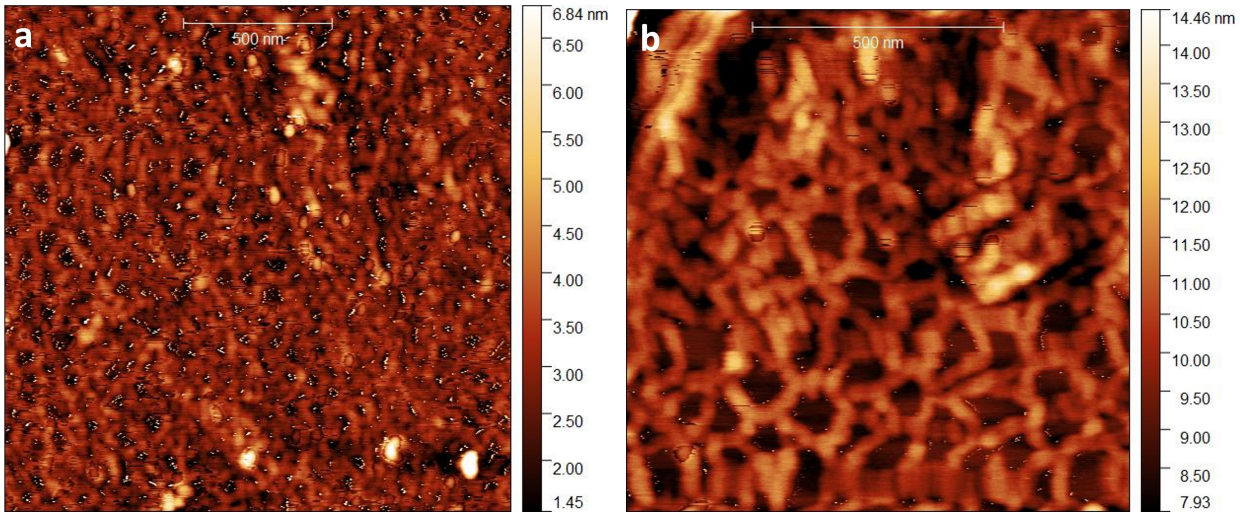

Figure 5.34: A closer look at the DNA origami nanostructures found on a poly-L-lysine functionalized graphite substrate

As more evident in Figure 5.34a, nanostructures with a higher height than the functionalization ($1 - 2$ nm). However, the assumed DNA origami nanostructures present a deformed structure compared to the triangular shapes seen in previous experiments. In Figure 5.34b, the topology appears blurry due to the plethora of biomolecules present on the surface, making the interaction of the tip with the surface more difficult.

Increasing the incubation to 5 minutes did not reduce the networks of poly-l-lysine and graphite formed. This observation suggests that a higher incubation time might allow for a more uniform height profile of the networks and a reduction of uncovered regions. Also, the deformed DNA origami nanostructures might mean that a higher concentration of poly-l-lysine is needed to avoid the denaturation of DNA strands.

Next, an experiment with an incubation time of around 30 minutes was conducted (Figure 5.35).

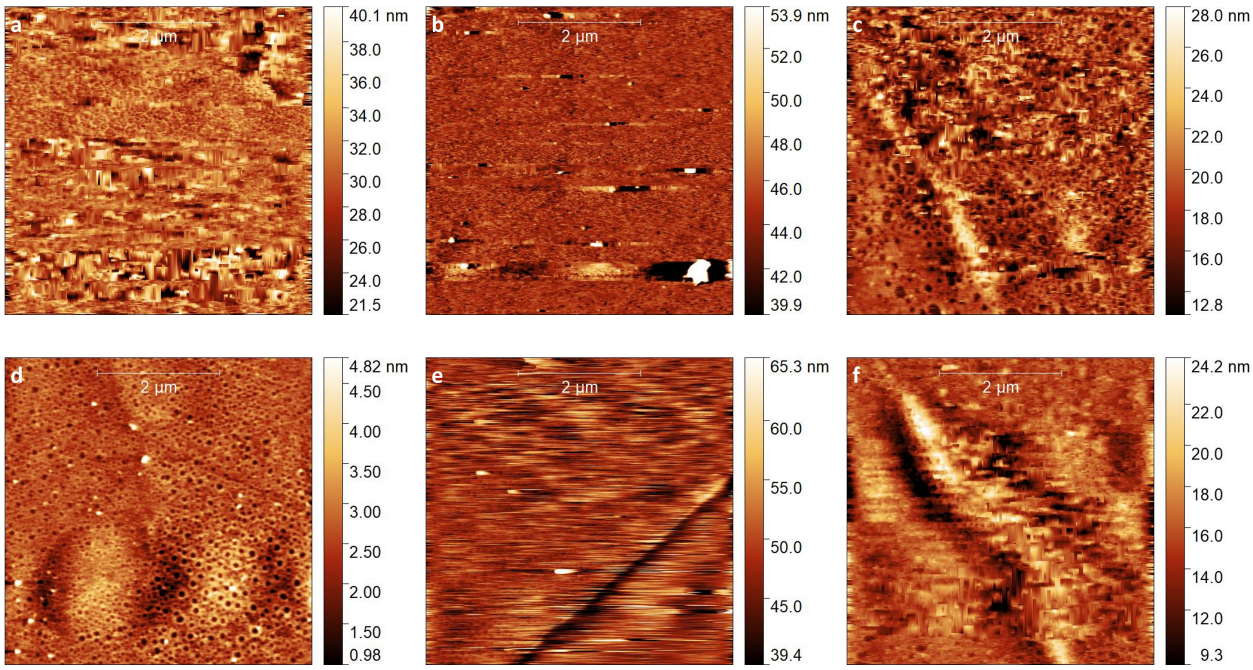

Figure 5.35: AFM images of poly-L-lysine functionalized substrates after deposition of DNA origami

Similar behaviour was observed for this experiment, with the incubation time not affecting the number of networks and aggregates. The new tip used, however, could not make accurate contact with the bottom of the mica surface because of the increased biomolecules on the surface. Deposition of DNA origami did not show any noticeable difference that can lead to an accurate characterization of DNA origami on poly-L-lysine functionalized surfaces. The height profiles of the poly-L-lysine layer were slightly wider than in previous cases ($1-7$ nm). The discrepancy is accounted for by the evaporation of the solution due to the higher incubation time.

The networking structure is unaffected by the increased incubation time. However, preventing the sample from evaporation could give a better measurement of the surface coverage. To avoid any evaporation due to atmospheric exposure, for the next experiments, the sample was shielded using a cup and a wet piece of paper to increase the humidity. Finally, an incubation time of 1 hour was used to complete these series of experiments (Figure 5.36).

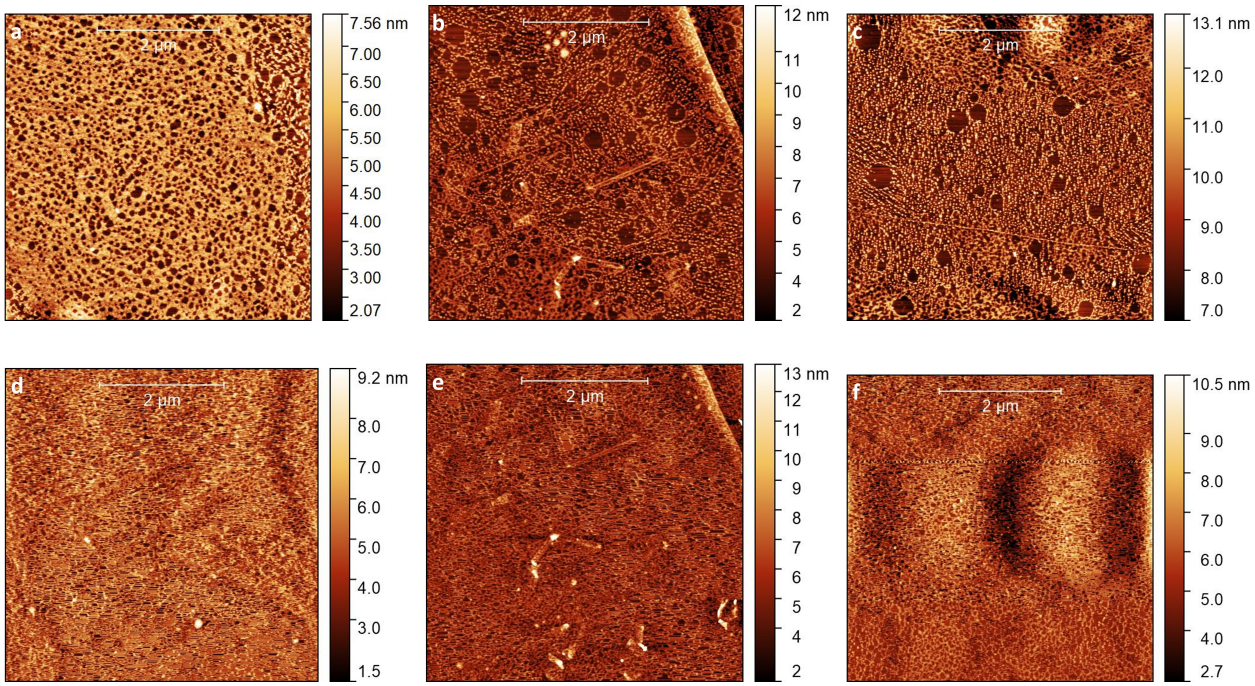

Figure 5.36: AFM images of poly-L-lysine functionalized substrates before (a-c) and after (d-f) deposition of DNA origami. The incubation time for poly-L-lysine for this experiment was 1 hour.

Our most intriguing finding is that increasing the incubation time to 1 hour decreased the surface roughness and the range of height values for poly-l-lysine ($2 - 4$ nm). That could mean that poly-l-lysine has reached its maximum surface coverage, having a uniform coating on graphite layers. However, poly-l-lysine did not fully cover the substrate. In addition, DNA origami nanostructures could not be identified.

The difficulty in imaging DNA origami can be explained by the large number of biomolecules on the surface. The number of molecules does not allow the tip to have intricate contact with DNA origami nanostructures. A more uniform and higher surface coverage could allow accurate characterization of DNA origami nanostructures on functionalized graphite.

5.5.1 Effect of incubation time on the roughness and topology of poly-L-lysine functionalized graphite substrates

For a better understanding of the effect of incubation time on the surface properties of functionalized graphite surfaces, roughness and topology were analysed for each condition. Figure 5.37 shows the topology of functionalized graphite surfaces followed by incubation of 5 minutes, 30 minutes and 60 minutes.

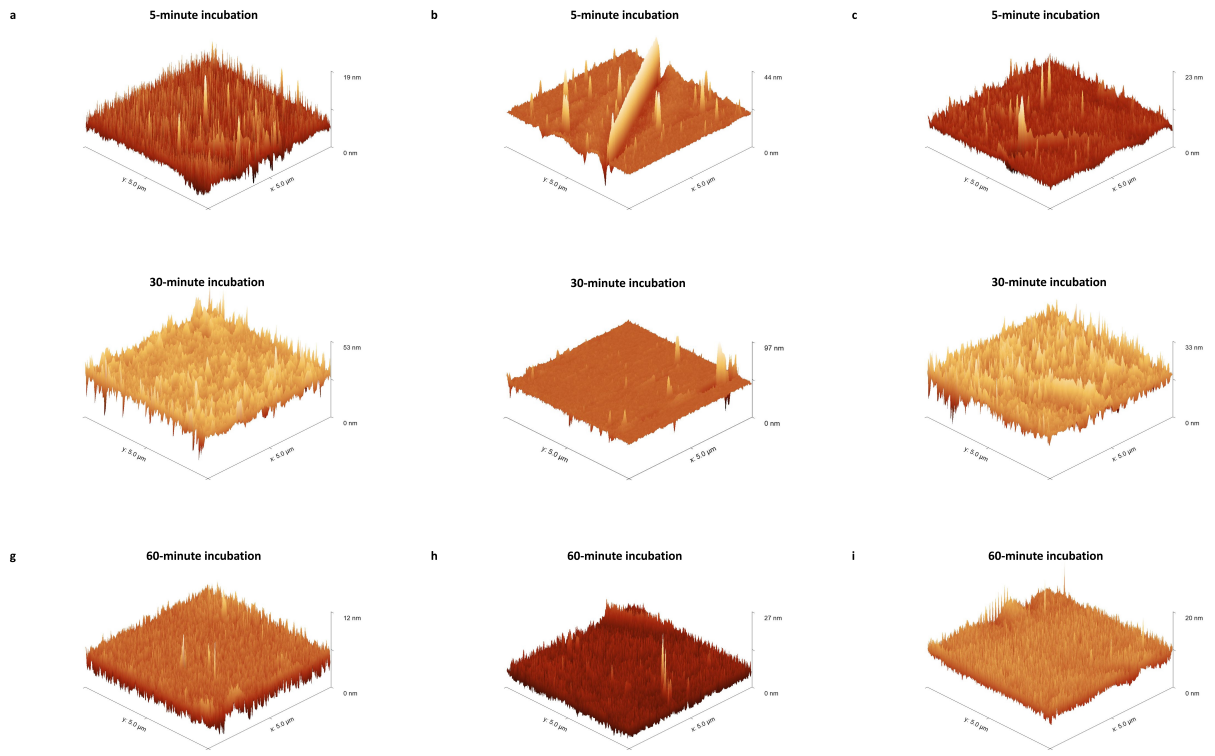

Figure 5.37: Topology Measurements of poly-L-lysine functionalized graphite surfaces before deposition of DNA origami followed by incubation of 5 minutes (a-c), 30 minutes (d-f) and 1 hour (g-i)

Incubation Time (min)	**RMS Roughness (nm)**	**Range of Heights (nm)**
5	1.74 ± 0.84	$1 - 5$
30	2.73 ± 0.19	$1 - 7$
60	1.27 ± 0.17	$2 - 4$

Table 5.4: Table showing the relationship between the roughness of the surface and the incubation time for poly-L-lysine

Taking a look at the average roughness values, the magnitude increases from the incubation time of 5 minutes to 30 minutes and then decreases at the 1-hour incubation time. For the 30-minute incubation, the surface roughness is more than expected due to the evaporation of the solution. However, when no evaporation occurred and the incubation time increased to 1 hour, the roughness value dropped by 0.5 nm. Additionally, the range of height profiles of the poly-L-lysine layer narrows for the 1-hour incubation time, suggesting that poly-L-lysine is distributed more uniformly on the surface. In all the samples, on the other hand, the networks of poly-L-lysine/graphite form and do not allow the accurate characterization of DNA origami triangles. The concentration of poly-L-lysine for all the cases was 0.0005 w/v %.

A conclusion drawn from these experiments is that increasing incubation time reduces the roughness and uniformity of the networks found on graphite. Additionally, biomolecules are attached to a lesser extent as the incubation time is increased from 5 to 60 minutes, as suggested by the maximum height values of the measurements.

A conclusion drawn from these experiments is that increasing incubation time reduces the roughness and the range of heights of the networks found on graphite. On the other side, in all cases, graphite

was not fully coated with poly-l-lysine molecules. The bare graphite regions might result in the denaturation of the DNA strands. To maximize the surface coverage of poly-l-lysine on graphite, the concentration of poly-L-lysine increased by 10 times (0.005 w/v %). By increasing the concentration, graphite might become saturated from poly-l-lysine and cover the whole graphite surface. The results of the final attempt are depicted in Figure 5.38.

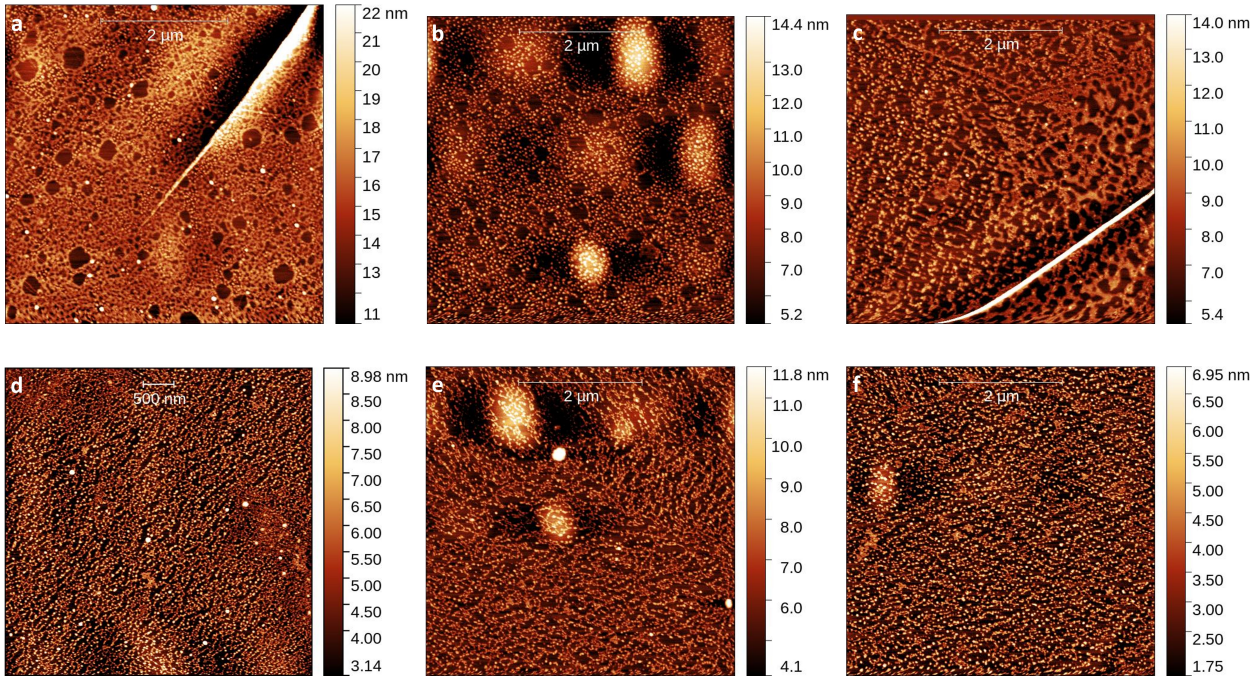

Figure 5.38: AFM measurements of functionalized graphite surfaces with PLL (0.005 w/v %) before (a-c) and after (d-e) DNA origami deposition

The increased concentration did not manage to cover fully the graphite surface. Also, as seen more clearly in Figures 5.38a and 5.38b, there are aggregates of PLL forming at some locations due to this increased concentration. The heights experienced throughout the networks matched the values previously found for the 1-hour incubation ($2-4$ nm). However, at the location of the aggregates, the height could reach values up to 8 nm. Due to this increase in aggregates, surface roughness increased to an average of 2.03 nm, which is even greater than the value found for 5-minute incubation.

Since graphite's π bonds might have fully reacted with poly-L-lysine, the more poly-L-lysine used does not have any space to bond to graphene layers. Therefore, the excess poly-l-lysine molecules form aggregates rather than filling the pristine graphite regions.

A conclusion drawn from this series of experiments is that concentration does not significantly affect the surface coverage of graphite. An increase in the volume could be an alternative solution to increase the surface coverage of poly-l-lysine on graphite.

On the other hand, the increase in concentration provided enhanced biocompatibility and led to the adhesion of DNA origami triangles. In total, about 21 triangles were visible in the 3 images taken after DNA origami deposition (Figures 5.38d - 5.38f). Zoomed-in images of the origami nanostructures were captured (Figure 5.39) to analyse their structural properties.

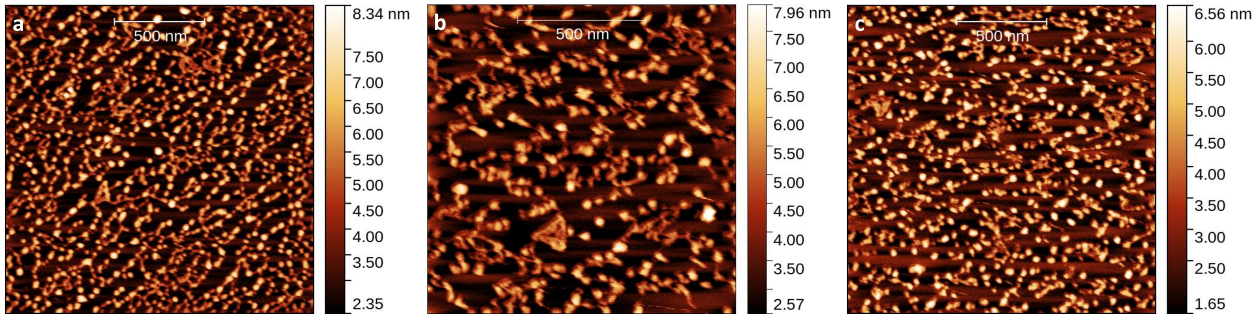

Figure 5.39: AFM measurements of Rutherford Triangles on poly-l-lysine functionalized graphite surfaces

The results demonstrate a decrease in the deformation of 5 nm compared to pristine graphite substrates (110.3 ± 15.4 nm). On the other hand, the range of length values remained wide (85-130 nm) because of the partial covering of graphite with poly-l-lysine. The height profiles of the origami were more uniform than in the unfunctionalized graphite substrate (1.6 - 3.0 nm). On the other hand, values of the thicknesses of the origami sides increased significantly to a value of 52.2 ± 6.5 nm per side.

This experiment can verify the influence of poly-l-lysine in decreasing the denaturation of DNA origami triangles at the right concentration. Since excess poly-l-lysine molecules were present on the substrate, on average 7 DNA origami nanostructures were attached to the substrate. The triangle lengths are about 5 nm below the corresponding value found on mica. Another change related to graphite substrates is the change of thickness of the triangle side that is a result of the attachment of both positively charged poly-l-lysine and magnesium ions. Table 5.5 compares the structural properties of Rutherford triangles on each substrate used. The range of values was determined using the standard deviation of the values measured which got rid of anomalies in the measurements. Covering the entire graphite region with poly-l-lysine could eliminate the denaturation of DNA strands of graphite.

Substrate	**Range of values (nm)**	**Average Dimensions (nm)**	**Thickness (nm)**	**Height (nm)**
Graphite	88.0-113.8	100.9	45.3 ± 13.7	2.7 ± 0.4
Poly-l-lysine Graphite	95.0-125.7	110.3	52.2 ± 11.2	2.3 ± 0.3
Mica	107.6-124.1	115.9	32.9 ± 7.6	1.5 ± 0.3

Table 5.5: Table comparing the structural properties of Rutherford Triangles on different substrates.

5.6 Characterization of DNA origami on pristine hBN substrates

Hexagonal Boron Nitride, or hBN for short, has shown some intrinsic properties in graphene/hBN heterostructures. In studies conducted [75–77], it was found that hBN can act as an excellent dielectric material for graphene, acting as an insulator layer. hBN has a similar hexagonal structure as graphene with high thermal and chemical stability. However, hBN and graphene have some differences in their properties. To get a better understanding of the differences, take a look at the electronic structures of graphene and hBN (Figures 5.40 and 5.41). Graphene is made purely of carbon atoms which form sigma bonds in plane due to hybridization of the s, p_x and p_y orbitals, whereas the p_z orbital forms a delocalized π bond out-of-plane. Each carbon atom bonds to another 3 carbon atoms.

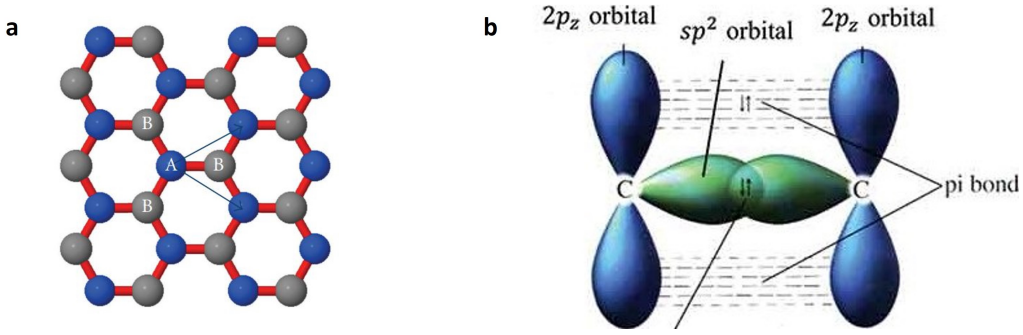

Figure 5.40: a) The hexagonal lattice structure of graphene and b) the corresponding orbitals of a carbon to carbon bond. Adapted from [78] and [79].

Similarly to graphene, hBN has a hexagonal structure and the same type of bonding as graphene (σ bonds in-plane and π bonds out-of-plane). Each Boron atom binds with another 3 Nitrogen atoms and vice versa (Figure 5.41). However, the band gap of hBN is wide [80], which means that hBN is an insulator and the π electrons out-of-plane are localized.

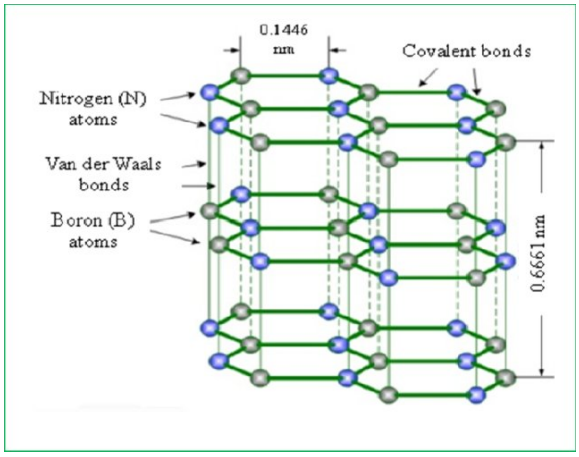

Figure 5.41: Diagram of the atomic structure of hexagonal Boron nitride (hBN). Adapted from [81].

Due to its insulating properties and since electrons are localized (because of the high band gap), hBN could be an alternative substrate for DNA origami nanostructures. The bonding between layers is Van der Waals which allows the extraction of few-layer hBN substrates in a similar manner to other 2D materials. Therefore, hBN flakes were transferred using the same PDMS stamp method as graphite. AFM measurements of hBN surfaces before and after the deposition of DNA origami triangles were captured. The results are conveyed in Figure 5.42.

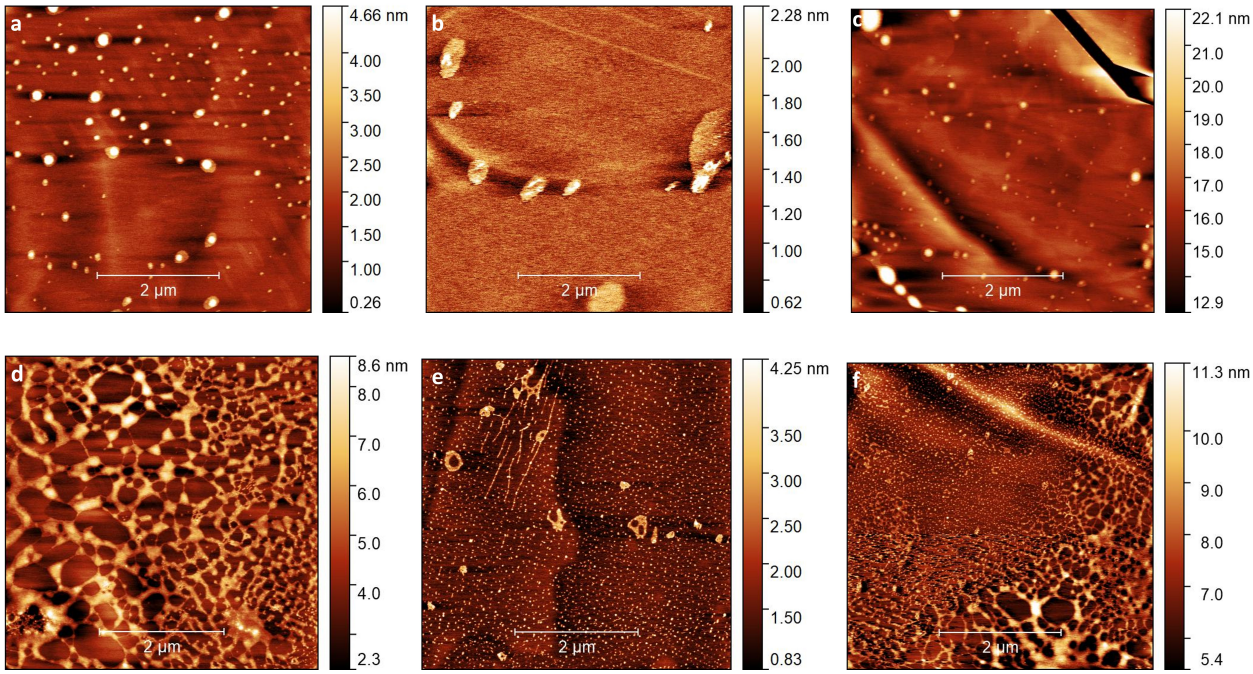

Figure 5.42: AFM images of hBN substrates before (a-c) and after (d-f) deposition of DNA origami

Measurements taken before the deposition of DNA origami had traces of PDMS residue, like graphite. Despite the similar topology, the surface roughness of bulk hBN appears significantly lower than bulk graphene. The average hBN roughness was about 620 pm, whereas graphite had an average of a bit higher than 1 nm. Despite the decreased roughness and the localized π electrons, hBN denatured DNA strands and formed DNA/Mg^{2+} networks. Also, all structures appear affected by the interaction with hBN. Scaled-up images show a less deformed triangle with its average dimensions equal to about 93.6 nm (Figure 5.43a). The value is about 6 nm below the average magnitude of DNA origami triangles on graphite substrates and almost a 25 nm difference from the corresponding magnitude for mica surfaces.

Although more measurements are required to verify the degree of deformation, the denaturation of DNA origami is noticeable. The effect of $\pi - \pi$ bonding reduces the side lengths of the Rutherford triangle, similarly to graphite.

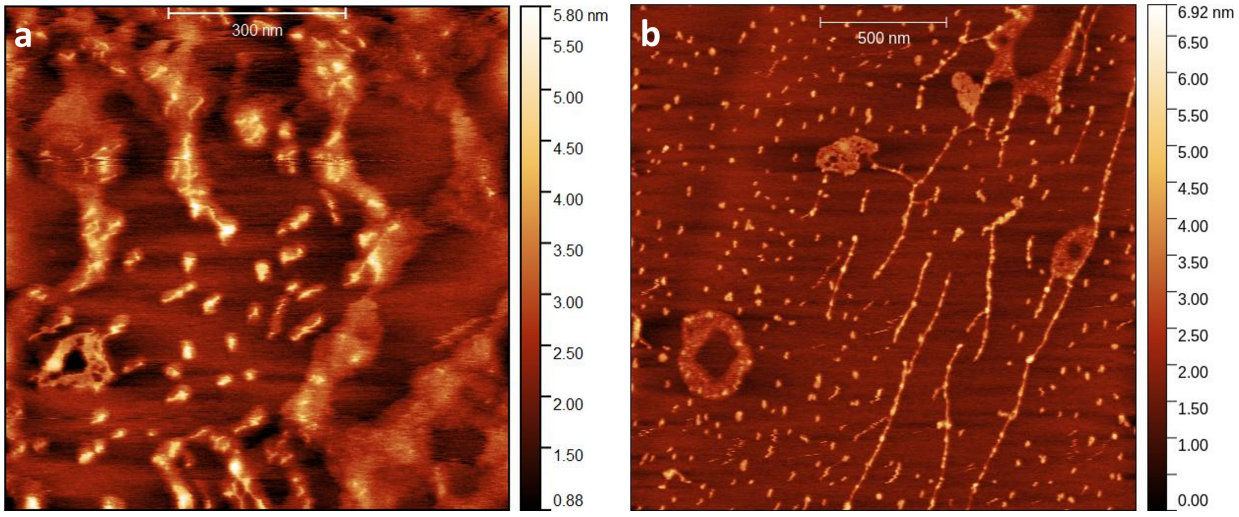

Figure 5.43: A closer look at DNA origami nanostructures on hBN surfaces using AFM measurements

Another observation that came to attention was that the DNA origami triangles adhered to mica (same sample as hBN) were in their natural state and were not deformed as appeared for graphite samples (Figure 5.44). The triangles that retain their triangular shape have an average triangle length of 115.0 ± 4.7 nm, which agrees with the measurements previously taken on freshly cleaved mica substrates. However, only 10 triangles adsorb to the surface, a significantly reduced number compared to freshly cleaved mica (see Table 5.1). The possible reasons for this behaviour are the reduced negative charge of the mica after exposure to the atmosphere and PDMS, and the hydrophobic nature of hBN causing increased water exposure and removal of DNA origami from the substrate.

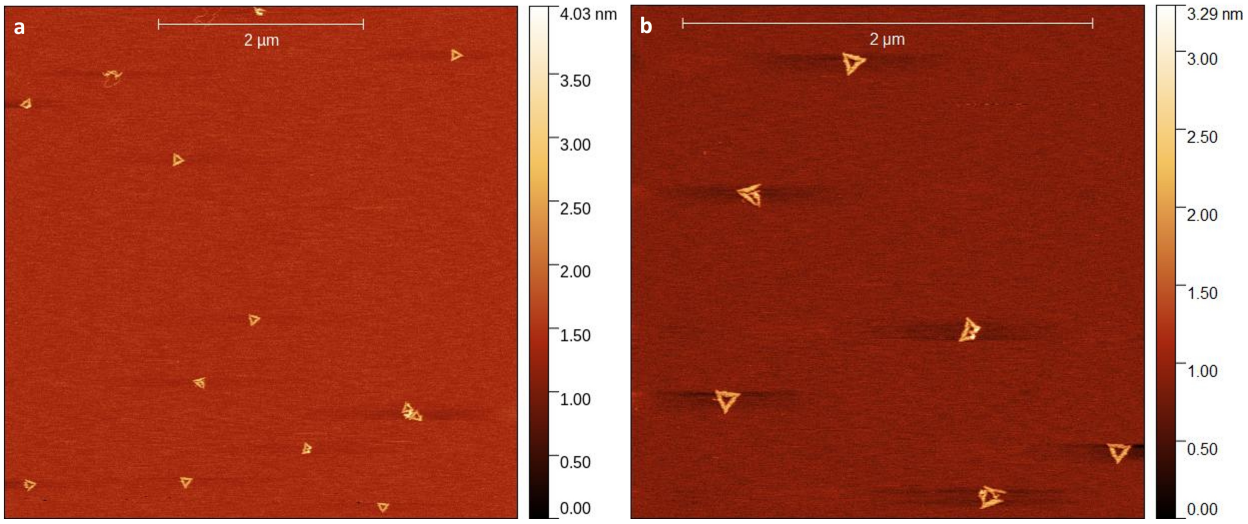

Figure 5.44: Zoomed images of DNA origami nanostructures on hBN surfaces

Optical images of hBN flakes on mica were captured from both the inverted microscope in BN and the top-down microscope in the Chemistry lab (Figure 5.45). The images give the reader an understanding of how hBN flakes look if illuminated from the bottom or the top.

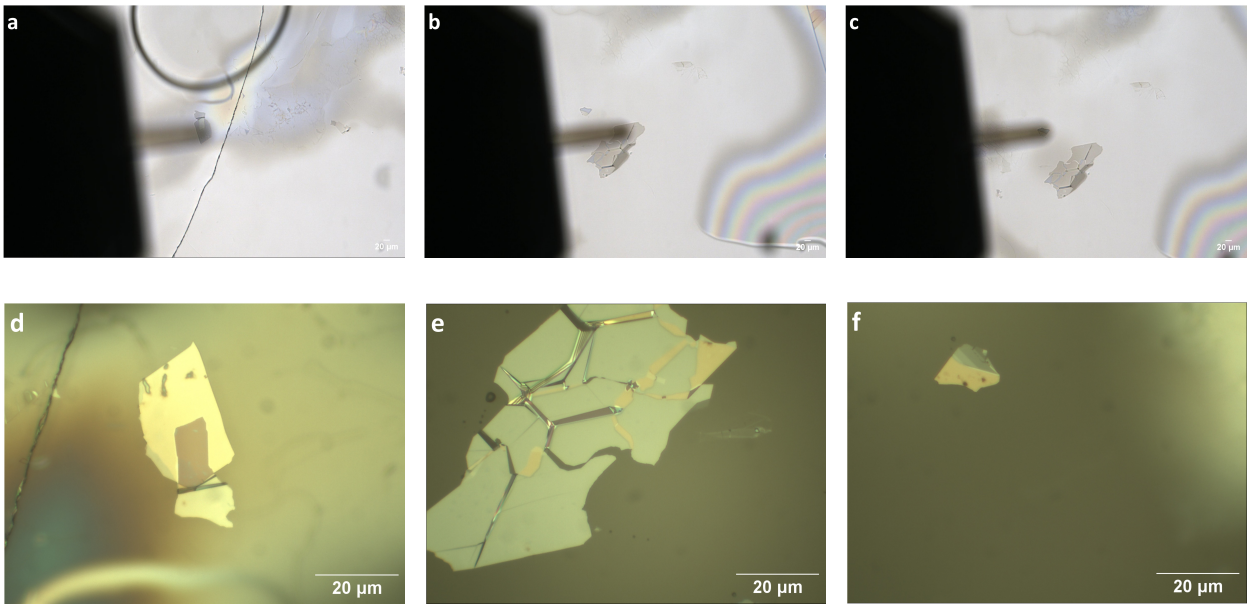

Figure 5.45: Optical images of hBN flakes on mica. The top images are taken from a microscope where the light is illuminated from the bottom, whereas the bottom images have the light placed above the sample. Magnification = 50 × for top, Magnification = 10 × for bottom.

In the case of a top-down microscope, the flake appears to change colours from blue to yellow when the hBN thickness increases and cracks are visible. On the other side, the inverted microscope changes from a grey to a dark black colour when thickness increases, while cracks are not detectable.

Chapter 6

Conclusion and Future Work

6.1 Conclusion

AFM and TEM are currently used for imaging DNA origami nanoarchitectures. While AFM allows imaging of static and dynamic imaging, TEM is only limited to static images. Challenges of TEM in enhancing resolution, minimizing damage and preparing the sample have limited its use in imaging DNA origami nanostructures. The aforementioned challenges of TEM have made AFM the main characterization method for DNA origami nanostructures. On the other hand, the invasiveness and lateral resolution limitation caused by the tip, limit the accurate characterization of DNA origami nanostructures. A new advancement in TEM technologies, namely liquid flow cells, might enable the imaging of static and dynamic nanostructures under vacuum and physiological conditions. Unfortunately, graphene substrates, which are the primary material for the fabrication of liquid flow cells, have been found to cause unwanted deformations on DNA origami structures due to $\pi - \pi$ bonds. Functionalization of graphite with poly-l-lysine and pyrene has decreased the degree of deformation of DNA origami. The main goal of this thesis is to give a quantitative comparison of the changes in DNA origami nanostructures after deposition on 2D materials, mainly graphite, and mica.

As a baseline, the deposition of DNA origami nanostructures on mica was performed. The nanostructures used for this project were the Rutherford Triangles (see Appendix A.4). Both the location and the rinsing method were altered to understand the effect of roughness and cleanliness of the surface on the DNA origami nanostructures. The best image location was determined to be at the centre of the mica because of the presence of elevated mica layers and cracks on the sides of the mica. Rinsing the sample effectively (2-3 times of 1000 μL MilliQ water) increased both the number of origami and the percentage of undeformed origami. An increase in the rinsing quantity has significantly reduced the surface roughness of mica. A clean surface increases the number of DNA origami nanostructures with cavities (designed structure) due to the reduced magnesium concentration on the substrate. The surface roughness plays an important role in the number of DNA origami nanostructures adhering to the surface. An increase in roughness does not allow an intricate contact of DNA origami with mica, thus less adhesion that causes the nanostructures to be washed away during rinsing. The side length of Rutherford triangles on mica was found to be 115.9 $\pm$ 8.3 nm and the thickness to be 32 nm (for optimal rinsing conditions).

Pristine graphite samples were prepared using the PDMS transfer method. The PDMS stamp allowed the deposition of graphite flakes at the centre of the substrate, where less salt remains after rinsing and drying. However, since the bonding of graphite and DNA origami is covalent, magnesium ions in the buffer formed networks of denatured DNA/Mg^{2+}. Furthermore, the hydrophobic nature of graphite and the increased roughness reduced the number of individual DNA origami triangles on graphite. Concerning the structural properties of Rutherford triangles, a noticeable reduction of 10 nm in the side length was found relative to mica. The discrepancy can be explained by the melting of dsDNA to

ssDNA, resulting in a reduction in the base length of the triangle sides. In addition, an increase in the thickness of triangle sides of 10 nm was measured using the image analysis software Gwyddion. The change in thickness was due to magnesium ions adhering to the phosphate backbone of DNA strands. Furthermore, another 2D material with a similar structure (hBN) was examined as a substrate for DNA origami. The difference is the localized π electrons present in hBN that make it an insulator. However, the localization of electrons did not change the interaction between DNA origami and the 2D material. On the other side, hBN supports have a decreased roughness compared to graphite. The reason for this difference is the possible higher quality of the hBN flakes (fewer cracks, more uniform) in relation to graphite which resulted in a more uniform surface after transfer.

In an attempt to decrease the degree of deformation, graphite surfaces were functionalized with poly-l-lysine. The incubation time and the concentration used in the literature varied significantly, therefore a series of experiments were utilized to find the effect of incubation time on the surface. The surface roughness decreased as the incubation time increased from 5 to 60 minutes. Also, the height profiles of the graphite/poly-l-lysine networks formed were more uniform. Additionally, the presence of networks made it difficult to characterize individual DNA origami nanostructures. Despite the presence of networks, a concentration of 0.005 w/v % and an incubation time of 60 minutes resulted in a surface where 7 DNA origami nanostructures were present in a 25 μm^2 area. Extracting the dimensions of the Rutherford triangles, the average value of the triangle side was 110.3 $\pm$ 15.4 nm, which is between the value found for mica and graphite substrates. Therefore, although poly-l-lysine decreases the degree of deformation, there is still a significant decrease in the base length of origami triangles on functionalized graphite. Furthermore, the thickness of origami triangles increased to 52 nm, mainly caused by the increased presence of positive ions in the mixture, since now both amide groups and magnesium ions are available for a salt bridge between DNA origami and mica. One thing to note is that none of the protocols used managed to cover the whole graphite surface.

In conclusion, it was determined that rinsing 2-3 times and imaging at the centre of mica gives the optimal properties for imaging DNA origami nanostructures. Rinsing helped in removing buffer residue and unattached DNA origami triangles. Furthermore, imaging at the sides should be avoided, since drying and rinsing the sample did not remove buffer residues. 2D materials, like hBN and graphite, created unwanted deformations on DNA origami structures because of the denaturation of DNA strands by $\pi - \pi$ bonds. Also, the formation of DNA/Mg^{2+} networks observed on graphite was due to the electrostatic interaction of denatured DNA strands and magnesium ions and the hydrophobic nature of graphite upon contact with the environment. Functionalization with poly-l-lysine reduces the deformation in the nanoarchitectures, however, the number and structural stability of the nanostructures are still greatly affected. A higher volume and concentration could enable the complete functionalization of the graphite surface. Under these conditions, there is a possibility of creating a biocompatible environment for DNA origami nanoarchitectures i.e. no denaturation.

6.2 Future Work

Although this project has answered some questions regarding the interaction of DNA origami with 2D materials, many issues remain unresolved. Future directions are related to the improvement of the protocol needed for poly-l-lysine functionalization. Increasing volume and/or concentration might allow for coverage of the whole graphite region. Quartz Crystal microbalance (QCMD) measurements could also help in extracting the incubation time required for maximum surface coverage. Using the determined volume, concentration and incubation time would give the best biocompatible environment for DNA origami nanostructures. Additionally, other functionalizations such as pyrene could be utilized and compared to bare and functionalized graphite surfaces. Pristine and functionalized graphite surfaces would give a complete overview of how DNA origami interacts with the corresponding 2D material. For data validation, experiments on monolayer graphene substrates could be used to examine the influence of thickness on the interaction of the nanostructures.

This study was limited to graphite substrates but could be extended to other 2D materials, pristine and functionalized, such as MoS_2. Since these two materials (graphene and MoS_2) dominate the liquid cell microscopy field, experiments on both would help to determine the optimal 2D surface for imaging dynamic DNA origami nanodevices. Subsequently, since both graphite and hBN flakes had polymer residue from the transfer, the effect of cleaning on the 2D materials' structure can be investigated using Raman Spectroscopy measurements. Furthermore, the degree of deformation on more complex DNA nanostructures that have extended ssDNA, like the robot shapes [44], could also be examined. The ssDNA extensions would indicate any difference between the interaction of ssDNA strands with graphite and dsDNA with graphite. Finally, the substrate with the least denaturation can be used as a suspended substrate for DNA origami nanostructures. The suspended substrate would mimic more accurately the support used for TEM measurements.

Bibliography

1. Göpfrich, K. & Keyser, U. F. Dna nanotechnology for building sensors, nanopores and ion-channels. *Biological and Bio-inspired Nanomaterials,* 331–370 (2019).
2. Husale, B. S. *et al.* ssDNA binding reveals the atomic structure of graphene. *Langmuir* **26,** 18078–18082 (2010).
3. Institute, N. H. G. R. *Double Helix* 2010. https://www.genome.gov/genetics-glossary/Double-Helix (2021).
4. Heck, C. *Gold and silver nanolenses self-assembled by DNA origami* PhD thesis (Universität Potsdam, 2017).
5. Zhang, F., Nangreave, J., Liu, Y. & Yan, H. Reconfigurable DNA origami to generate quasifractal patterns. *Nano letters* **12,** 3290–3295 (2012).
6. Lanphere, C. *et al.* Design, assembly, and characterization of membrane-spanning DNA nanopores. *Nature Protocols* **16,** 86–130 (2021).
7. Rothemund, P. W. Folding DNA to create nanoscale shapes and patterns. *Nature* **440,** 297–302 (2006).
8. Douglas, S. M. *et al.* Rapid prototyping of 3D DNA-origami shapes with caDNAno. *Nucleic acids research* **37,** 5001–5006 (2009).
9. Zhang, D. Y. & Seelig, G. Dynamic DNA nanotechnology using strand-displacement reactions. *Nature chemistry* **3,** 103–113 (2011).
10. Marini, M. *et al.* A revertible, autonomous, self-assembled DNA-origami nanoactuator. *Nano letters* **11,** 5449–5454 (2011).
11. Marras, A. E., Zhou, L., Su, H.-J. & Castro, C. E. Programmable motion of DNA origami mechanisms. *Proceedings of the National Academy of Sciences* **112,** 713–718 (2015).
12. Ke, Y., Meyer, T., Shih, W. M. & Bellot, G. Regulation at a distance of biomolecular interactions using a DNA origami nanoactuator. *Nature communications* **7,** 1–8 (2016).
13. Tanaka, F. *et al.* Robust and photocontrollable DNA capsules using azobenzenes. *Nano letters* **10,** 3560–3565 (2010).
14. Liang, X., Mochizuki, T. & Asanuma, H. A supra-photoswitch involving sandwiched DNA base pairs and azobenzenes for light-driven nanostructures and nanodevices. *Small* **5,** 1761–1768 (2009).
15. Gerling, T., Wagenbauer, K. F., Neuner, A. M. & Dietz, H. Dynamic DNA devices and assemblies formed by shape-complementary, non–base pairing 3D components. *Science* **347,** 1446–1452 (2015).
16. Idili, A., Vallée-Bélisle, A. & Ricci, F. Programmable pH-triggered DNA nanoswitches. *Journal of the American Chemical Society* **136,** 5836–5839 (2014).
17. Mao, C., Sun, W., Shen, Z. & Seeman, N. C. A nanomechanical device based on the B–Z transition of DNA. *Nature* **397,** 144–146 (1999).

18. Kopperger, E. *et al.* A self-assembled nanoscale robotic arm controlled by electric fields. *Science* **359,** 296–301 (2018).

19. Lauback, S. *et al.* Real-time magnetic actuation of DNA nanodevices via modular integration with stiff micro-levers. *Nature communications* **9,** 1–11 (2018).

20. Scheible, M., Jungmann, R. & Simmel, F. C. in *Nano-Biotechnology for Biomedical and Diagnostic Research* 87–96 (Springer, 2012).

21. Endo, M., Hidaka, K. & Sugiyama, H. Direct AFM observation of an opening event of a DNA cuboid constructed via a prism structure. *Organic & biomolecular chemistry* **9,** 2075–2077 (2011).

22. Xin, Y., Zargariantabrizi, A. A., Grundmeier, G. & Keller, A. Magnesium-Free Immobilization of DNA Origami Nanostructures at Mica Surfaces for Atomic Force Microscopy. *Molecules* **26,** 4798 (2021).

23. Namba, K. & Stubbs, G. Structure of tobacco mosaic virus at 3.6 Å resolution: implications for assembly. *Science* **231,** 1401–1406 (1986).

24. Harris, J. R. & Horne, R. W. Negative staining: A brief assessment of current technical benefits, limitations and future possibilities. *Micron* **25,** 5–13 (1994).

25. Henderson, R. The potential and limitations of neutrons, electrons and X-rays for atomic resolution microscopy of unstained biological molecules. *Quarterly reviews of biophysics* **28,** 171–193 (1995).

26. Park, J. *et al.* Graphene liquid cell electron microscopy: Progress, applications, and perspectives. *ACS nano* **15,** 288–308 (2021).

27. Meyer, J. C., Girit, Ç. Ö., Crommie, M. & Zettl, A. Imaging and dynamics of light atoms and molecules on graphene. *Nature* **454,** 319–322 (2008).

28. Eda, G., Fanchini, G. & Chhowalla, M. Large-area ultrathin films of reduced graphene oxide as a transparent and flexible electronic material. *Nature nanotechnology* **3,** 270–274 (2008).

29. Chen, J.-H. *et al.* Charged-impurity scattering in graphene. *Nature physics* **4,** 377–381 (2008).

30. Ziegler, K. Robust transport properties in graphene. *Physical review letters* **97,** 266802 (2006).

31. Matković, A. *et al.* Enhanced structural stability of DNA origami nanostructures by graphene encapsulation. *New Journal of Physics* **18,** 025016 (2016).

32. Jeon, J. *et al.* Superb resolution and contrast of transmission electron microscopy images of unstained biological samples on graphene-coated grids. *Biochimica et Biophysica Acta (BBA)-General Subjects* **1830,** 3807–3815 (2013).

33. Brenner, S. & Horne, R. A negative staining method for high resolution electron microscopy of viruses. *Biochimica et biophysica acta* **34,** 103–110 (1959).

34. Wang, C., Qiao, Q., Shokuhfar, T. & Klie, R. F. High-resolution electron microscopy and spectroscopy of ferritin in biocompatible graphene liquid cells and graphene sandwiches. *Advanced Materials* **26,** 3410–3414 (2014).

35. Shan, C. *et al.* Water-soluble graphene covalently functionalized by biocompatible poly-L-lysine. *Langmuir* **25,** 12030–12033 (2009).

36. Chen, Q. *et al.* 3D motion of DNA-Au nanoconjugates in graphene liquid cell electron microscopy. *Nano letters* **13,** 4556–4561 (2013).

37. Cho, D.-H. *et al.* Effect of surface morphology on friction of graphene on various substrates. *Nanoscale* **5,** 3063–3069 (2013).

38. Ishigami, M., Chen, J., Cullen, W., Fuhrer, M. & Williams, E. Atomic structure of graphene on SiO2. *Nano letters* **7,** 1643–1648 (2007).

39. Lee, C. *et al.* Frictional characteristics of atomically thin sheets. *science* **328,** 76–80 (2010).

40. Lui, C. H., Liu, L., Mak, K. F., Flynn, G. W. & Heinz, T. F. Ultraflat graphene. *Nature* **462,** 339–341 (2009).

41. Green, N. S., Pham, P. H., Crow, D. T., Burke, P. J. & Norton, M. L. Layered graphene-mica substrates induce melting of DNA origami. *Materials Research Express* **5,** 045035 (2018).

42. Suk, J. W. *et al.* Transfer of CVD-grown monolayer graphene onto arbitrary substrates. *ACS nano* **5,** 6916–6924 (2011).

43. Lyubchenko, Y. L. Preparation of DNA and nucleoprotein samples for AFM imaging. *Micron* **42,** 196–206 (2011).

44. Kabiri, Y. *et al.* Distortion of DNA origami on graphene imaged with advanced TEM techniques. *small* **13,** 1700876 (2017).

45. Kaminska, I. *et al.* Distance dependence of single-molecule energy transfer to graphene measured with DNA origami nanopositioners. *Nano Letters* **19,** 4257–4262 (2019).

46. Brintlinger, T. H. *et al.* Aberration-corrected scanning transmission electron microscopy and energy-dispersive spectral maps of DNA origami triangles using graphene supports. *Microscopy and Microanalysis* **24,** 386–387 (2018).

47. Buckhout-White, S. *et al.* TEM imaging of unstained DNA nanostructures using suspended graphene. *Soft Matter* **9,** 1414–1417 (2013).

48. Akca, S., Foroughi, A., Frochtzwajg, D. & Postma, H. W. C. Competing interactions in DNA assembly on graphene. *PLoS One* **6,** e18442 (2011).

49. Varghese, N. *et al.* Binding of DNA nucleobases and nucleosides with graphene. *ChemPhysChem* **10,** 206–210 (2009).

50. AM, C. P., Oretskaya, T. S. & AM, O. B. Adsorption of synthetic homo-and hetero-oligodeoxynucleotides onto highly oriented pyrolytic graphite: Atomic force microscopy characterization. *Biophysical chemistry* **121,** 131–141 (2006).

51. Jariwala, D., Sangwan, V. K., Lauhon, L. J., Marks, T. J. & Hersam, M. C. Emerging device applications for semiconducting two-dimensional transition metal dichalcogenides. *ACS nano* **8,** 1102–1120 (2014).

52. Bonaccorso, F. *et al.* Graphene, related two-dimensional crystals, and hybrid systems for energy conversion and storage. *Science* **347,** 1246501 (2015).

53. Li, X. & Zhu, H. Two-dimensional MoS2: Properties, preparation, and applications. *Journal of Materiomics* **1,** 33–44 (2015).

54. Choi, J. *et al.* Nanomanufacturing of 2D Transition Metal Dichalcogenide Materials Using Self-Assembled DNA Nanotubes. *Small* **11,** 5520–5527 (2015).

55. Yang, J. *et al.* MoS2 liquid cell electron microscopy through clean and fast polymer-free MoS2 transfer. *Nano letters* **19,** 1788–1795 (2019).

56. Lin, Z. *et al.* Controllable growth of large–size crystalline MoS2 and resist-free transfer assisted with a Cu thin film. *Scientific reports* **5,** 1–10 (2015).

57. Choi, M. K. *et al.* Thermally controlled, patterned graphene transfer printing for transparent and wearable electronic/optoelectronic system. *Advanced Functional Materials* **25,** 7109–7118 (2015).

58. Bae, S. *et al.* Roll-to-roll production of 30-inch graphene films for transparent electrodes. *Nature nanotechnology* **5,** 574–578 (2010).

59. Wang, X. *et al.* Direct Delamination of Graphene for High-Performance Plastic Electronics. *Small* **10,** 694–698 (2014).

60. Abellan, P. *et al.* Factors influencing quantitative liquid (scanning) transmission electron microscopy. *Chemical Communications* **50,** 4873–4880 (2014).

61. Woehl, T. & Abellan, P. Defining the radiation chemistry during liquid cell electron microscopy to enable visualization of nanomaterial growth and degradation dynamics. *Journal of microscopy* **265,** 135–147 (2017).

62. Zhu, C. *et al.* Single-layer MoS2-based nanoprobes for homogeneous detection of biomolecules. *Journal of the American Chemical Society* **135,** 5998–6001 (2013).

63. Zhang, X., Rahman, M., Neff, D. & Norton, M. L. DNA origami deposition on native and passivated molybdenum disulfide substrates. *Beilstein journal of nanotechnology* **5,** 501–506 (2014).

64. Butt, H.-J. Measuring electrostatic, van der Waals, and hydration forces in electrolyte solutions with an atomic force microscope. *Biophysical journal* **60,** 1438–1444 (1991).

65. Klapetek, P., Necas, D. & Anderson, C. Gwyddion user guide. *Czech Metrology Institute* **2007,** 2009 (2004).

66. Bruker. *TopViewOptics with Granite Base* 2015. https://www.bruker.com/en/products-and-solutions/microscopes/bioafm/bioafm-accessories/topviewoptics-with-granite-base.html (2022).

67. Bruker. *NanoWizard 4 XP BioScience Properties* 2019. https://www.bruker.com/en/products-and-solutions/microscopes/bioafm/jpk-nanowizard-4-xp-bioscience.html (2022).

68. Bruker. *MultiMode 8-HR Properties* 2015. https://www.bruker.com/en/products-and-solutions/microscopes/materials-afm/multimode-8-hr-afm.html (2022).

69. Kielar, C. *et al.* On the stability of DNA origami nanostructures in low-magnesium buffers. *Angewandte Chemie* **130,** 9614–9618 (2018).

70. Li, Z. *et al.* Effect of airborne contaminants on the wettability of supported graphene and graphite. *Nature materials* **12,** 925–931 (2013).

71. Kim, H., Surwade, S. P., Powell, A., O'Donnell, C. & Liu, H. Stability of DNA origami nanostructure under diverse chemical environments. *Chemistry of Materials* **26,** 5265–5273 (2014).

72. Brintlinger, T. H. *et al.* Chemical Mapping of Unstained DNA Origami Using STEM/EDS and Graphene Supports. *ACS Applied Nano Materials* **3,** 1123–1130 (2020).

73. Shan, C. *et al.* Water-soluble graphene covalently functionalized by biocompatible poly-L-lysine. *Langmuir* **25,** 12030–12033 (2009).

74. Morga, M., Adamczyk, Z., Kosior, D. & Kujda-Kruk, M. Kinetics of Poly-l-lysine adsorption on mica and stability of formed monolayers: theoretical and experimental studies. *Langmuir* **35,** 12042–12052 (2019).

75. Jang, C. *et al.* Tuning the effective fine structure constant in graphene: Opposing effects of dielectric screening on short-and long-range potential scattering. *Physical review letters* **101,** 146805 (2008).

76. Kim, K. K. *et al.* Synthesis and characterization of hexagonal boron nitride film as a dielectric layer for graphene devices. *ACS nano* **6,** 8583–8590 (2012).

77. Datta, S. S., Strachan, D. R., Mele, E. & Johnson, A. C. Surface potentials and layer charge distributions in few-layer graphene films. *Nano letters* **9,** 7–11 (2009).

78. Cooper, D. R. *et al.* Experimental review of graphene. *International Scholarly Research Notices* **2012** (2012).

79. Yang, G., Li, L., Lee, W. B. & Ng, M. C. Structure of graphene and its disorders: a review. *Science and technology of advanced materials* **19,** 613–648 (2018).

80. Wang, J., Ma, F., Liang, W. & Sun, M. Electrical properties and applications of graphene, hexagonal boron nitride (h-BN), and graphene/h-BN heterostructures. *Materials Today Physics* **2,** 6–34 (2017).

81. Majety, S. *et al. Semiconducting hexagonal boron nitride for deep ultraviolet photonics* in *Quantum Sensing and Nanophotonic Devices IX* **8268** (2012), 607–614.

82. Tørring, T., Voigt, N. V., Nangreave, J., Yan, H. & Gothelf, K. V. DNA origami: a quantum leap for self-assembly of complex structures. *Chemical Society Reviews* **40,** 5636–5646 (2011).

Appendix A

Appendix

A.1 Preparation of Buffer

The solution prepared was for a 250 mL buffer. The final concentration of the chemicals of the buffer were:

- **Tris** 0.04 M
- **Acetic Acid** 0.02 M
- **Ethylenediaminetetraacetic acid (EDTA)** 0.001 M
- **$MgCl_2$** 0.01 M

The procedure followed was:

(1) Prepare a 100 mL MilliQ water on a 300 mL beaker.

(2) Add all the chemicals in the required mass in the beaker containing the water. $MgCl_2$ was added last so that the majority of the ligands of EDTA were occupied from the 2 acids and magnesium ions would give the buffer the appropriate positive charge to enable adhesion of the DNA origami into the negatively charged mica.

(3) Add droplets of concentrated NaOH and use a magnetic spinner. Continue spinning and adding droplets until the liquid does not contain any crystals in the solution.

(4) Then, use a pH meter and using concetrated NaOH to increase pH and concetrated HCl to decrease pH to make the pH of the solution to reach a value between 8.5-9.

(5) Add MilliQ water until the solution reaches the 250 mL mark.

A.2 Preparation of mica

(1) Cut a small piece of mica using scissors.

(2) Stick the mica using UV glue in a glass substrate.

(3) Cleave the mica using a tape. Look at the tape to see that a uniform cleaving is achieved i.e. in the tape you can see the shape of a mica substrate. Also looking the mica substrate at eye level can help distinquish whether mica is atomically flat.

A.3 Complete Data of Rinsing Conditions Experiment

Rinses	Number of Triangles	Number of deformed Triangles	Aggregates	Cavities
0	65	15	6	7
0	39	36	11	0
0	40	18	10	0
0	45	14	9	13
0	72	44	13	1
1	47	5	1	40
1	39	7	5	40
1	20	9	11	0
1	0	0	16	0
1	0	0	10	0
2	40	5	1	38
2	59	6	3	53
2	75	11	4	42
2	51	7	2	47
3	80	17	2	63
3	84	10	2	77
3	43	9	3	39
3	52	7	3	44
3	66	14	5	58

Table A.1: Table assessing different parameters regarding DNA origami interaction with mica as rinsing conditions are changed

A.4 Composition of Rutherford Triangles (RTO) DNA origami

The DNA origami nanostructures used for this experiment were the standard Rutherford (RTO) triangles. The edge length of the triangle is about 376 bases, resulting to a dimension of about 127.8 nm. The assembly buffer used for the composition was 10 mM MgCl2 and 1 × TAE. This is the same buffer used also for the dilution of DNA origami. Rutherford designed those triangles among other shapes and their structures can be seen in more detail in Figure A.1.

(a) (b)

Figure A.1: a) Schematic and b) AFM representation of Rutherford triangles. In Figure a) the linkers are shown with red colour and most of the structure is composed of dsDNA, including a hairpin at the bottom side of the triangle. Adapted from [82].

A.5 Imaging of DNA origami diluted with MilliQ water on mica and graphite substrates

Experiments conducted on bulk graphene substrates for both the diluted DNA origami and buffer solution involved a lot of networks developing on the surface. In the case of buffer deposition, there wasn't any network formation because of the lack of a negative charge to connect the positively charged magnesium ions between them. However, it might be that the magnesium concentration in the solution might be used in excess for graphite substrate adsorption. This is because, for graphite surfaces, no ions are required for DNA origami triangles to adsorb. As a result, there are free magnesium ions that react with the phosphate backbone of DNA, forming networks of Mg^{2+}/DNA. In an attempt to see the effects of a reduced magnesium concentration on bulk graphite substrates, an experiment was performed with DNA origami diluted using MilliQ water and not TAE/Mg_{2+} buffer solution. This means that only the magnesium concentration that was present in the sample due to the assembly was present (136 times less than what is normally used).

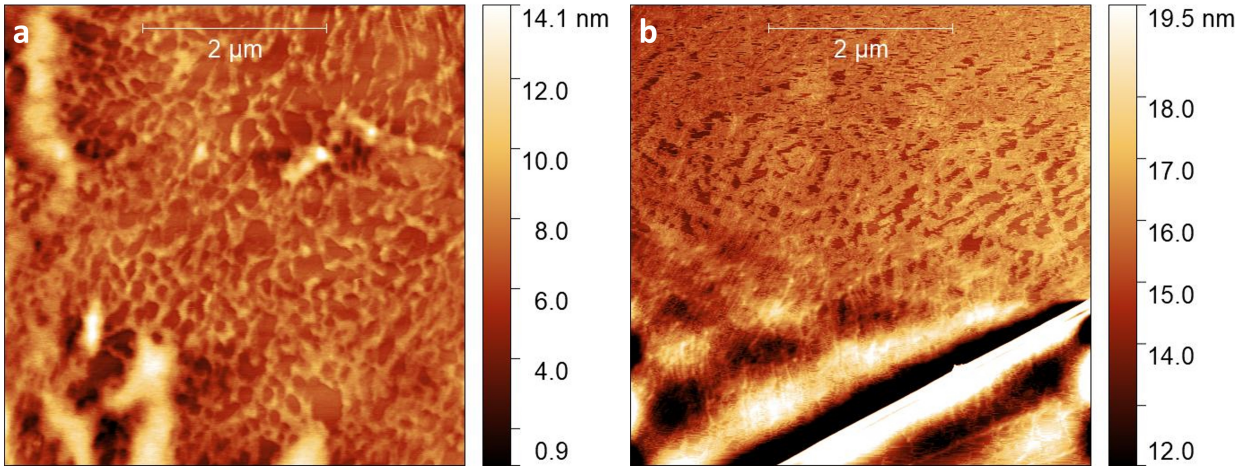

Figure A.2: AFM images of 2 nM DNA origami solution diluted using MilliQ water on graphite and graphite/mica substrates

It can be seen that decreasing the salt concentration led to an increase in the number of aggregates and the Mg^{2+}/DNA networks produced on bulk graphene. Diluting the DNA origami assembly buffer using MilliQ water, made the ions present in the solution (Mg^{2+} from the buffer and DNA origami) closer to each other forming ion clusters. Also, because the ions got closer together, denatured DNA strands formed more networks with magnesium ions after deposition on graphite. Therefore, it seems that even the much lower concentration was enough for the DNA origami nanostructures to buckle up together and form networks, not allowing the structural analysis of individual origami nanostructures. Spin filtering could be used to remove all the Magnesium ions present in the assembly buffer, while also changing the buffer to a Phosphate Saline buffer, like in the methodology performed in [22], however, this would greatly reduce the DNA origami concentration. For this reason, no further reduction of the magnesium ions in the solution used was conducted.